MICROSCALE TESTING AND CHARACTERIZATION TECHNIQUES FOR BENCHMARKING CRYSTAL PLASTICITY MODELS

by

David Eastman

A thesis submitted to Johns Hopkins University in conformity with the requirements for the degree of Doctor of Philosophy

Baltimore, Maryland

October, 2018

Abstract

The desire to improve the performance of engineering alloys and introduce new materials into service has led to the development of advanced, multi-scale material property models that can accurately predict the deformation response of polycrystalline microstructures. These microstructure-dependent, multi-scale models have the ability to provide insight into the connections between material processing, microstructure and properties in a way that has not been available before. However, these advanced modeling techniques require microstructural characterization and experimentally obtained benchmarks at salient length scales. Accordingly, microtensile tests of the polycrystalline Ni-base superalloy René 88DT have been carried out in order to guide and benchmark parallel crystal plasticity finite element method (CPFEM) modeling of this material at appropriate length scales. Microscale machining processes, including wire electrical discharge machining (EDM), focused ion beam (FIB) and femtosecond laser machining, have been developed and optimized for machining microtensile samples across multiple sizes. Loading in uniaxial tension provides the full stress-strain behavior from which quantitative mechanical benchmarks such as yield strength, strain hardening, and modulus can be extracted. The effect of sample size was studied to observe the underlying effects of microstructural variations. It was found that average sample strength decreased, and stochasticity of strength increased, as sample size decreased, owing to a finite sampling of grain orientations with a biased distribution towards higher Schmid factor values for grains in a randomly textured FCC material.

In addition, local strain accumulation on the surface of tested oligocrystalline samples, with a computationally tractable number of grains, has been measured through the use of 2D digital image correlation (DIC). It was observed that strain concentrations formed in regions of the microstructure where there was a significant mismatch in Schmid factor and elastic modulus across grain and twin boundaries, a microstructural feature that leads to local stress concentrations. These observations help to guide model development in highlighting deformation mechanisms in the material, and the developed strain maps provide both quantitative and qualitative benchmarks that can be directly compared with modeling results.

The scale of these experiments allows for 3D characterization, via serial sectioning and electron backscatter diffraction (EBSD), of tested samples through collection of critical microstructural data, including size, shape and orientation of grains and twins within the tested volume. Experimentally capturing explicit microstructures, at a scale that is also computationally tractable in crystal plasticity modeling, and their attendant mechanical behavior highlights stochastic nature of plasticity in small volumes and provides quantitative metrics for model development.

Advisor: Professor Kevin Hemker

Readers: Professors Kevin Hemker, Jaafar El-Awady, Somnath Ghosh

Acknowledgements

There are many people that I need to thank that have helped me on the path to completing my Ph.D. First and foremost, I want to thank my advisor, Professor Kevin Hemker. He has such passion and enthusiasm for research and dedication to his students. I am so thankful to have had the opportunity to work with him for the past five years.

I want to thank Professor Somnath Ghosh and Professor Jaafar El-Awady for their support both as part of the CEIMM project and for their help in editing this thesis and being part of my thesis defense committee.

I want to acknowledge the many wonderful people that I had the opportunity to work with in the Hemker Group. I want to thank Professor Jessica Krogstad, now at the University of Illinois, who was a fantastic mentor and profound source of knowledge and motivation for me when I first started my Ph.D. I want to thank Dr. Zafir Alam who I was fortunate to work very closely with and who taught me a great deal about superalloys. Professor Kelvin Xie, now at Texas A&M University, was also a huge inspiration for me during my Ph.D. with his persistently positive attitude and scholarly advice. These three former postdoctoral researchers of the Hemker group in particular have helped me to build the foundation for my own future in research and I cannot thank them enough. I want to specifically thank Gianna Valentino who is one of the closest friends that I have made at Johns Hopkins and someone that I have counted on for help on a regular basis, whether it is talking about DIC or assisting me in editing this thesis. I also thank Jalil Alidoost and Ojaswi Agarwal for taking the time to help me in editing this thesis as well.

I want to thank the many other Hemker group members, past and present, that I have gotten the chance to work with including Dr. Gidong Sim, Dr. Yong Zhang, Dr. Madhav Reddy, Dr. Ankur Chauhan, Dr. Binwei Zhang, Dr. Stephen Ryan, Dr. Simon Lockyer-Bratton, Dr. Suman Dasgupta, Dr. Paul Rottman, Dr. Brady Butler, Betsy Congdon, Luoning Ma, David Mills, Matt Vaughn, Arunima Banerjee and Sam Present.

I would also like to acknowledge the fantastic undergraduate research assistants that I had the chance to work with in Glenn Balbus, Bailey Hannon, Kevin Peters, Andrew Shaughnessey, Brandon Fielder, Avi Gordon, Andrew Holliday and Minjea Jo. I enjoyed working with all of you and without your efforts the work accomplished for this thesis could not have been possible. I hope that I was able to be a positive mentor for you and I know that you all will have very successful futures.

I am very thankful to have had the chance to be a part of the Center of Excellence in Integrated Materials Modeling and for the many collaborators that I had the opportunity to work with. I especially want to thank Drs. Paul Shade and Michael Uchic from the Air Force Research Lab for hosting me when I came to work at the AFRL, for their constant support in my work and for teaching me a great deal about being an experimentalist. I would also like to thank the CEIMM leadership from AFRL and AFOSR of Drs. Mike Groeber, Chris Woodward, Craig Przybyla and Ali Sayir. I would again like to thank Professor Somnath Ghosh for his leadership in the CEIMM project and members of his group that I was able to work with in George Weber, who has been a great friend and colleague, Dr. Akbar Bagri, Max Pinz, Deniz Öztürk, Dr. Ahmad Shahba and Dr. Shahriyar Keshavarz. I would also again like to thank Professor Jaafar El-Awady and his group member Dr. Yejun Gu for their collaborations. I would also like to thank

Professor Tresa Pollock from UCSB and her group members Drs. Will Lenthe, Jean-Charles Stinville and McLean Echlin, as well as Professor Graham-Brady from Johns Hopkins University and her student Noah Wade. I would like to thank Drs. Adrian Loghin, Shak Ismonov, Jud Marte, Doug Konitzer, Jeff Williams from GE who were great advisors in this project and provided us with resources necessary for this research including most of the material that was tested.

I want to thank the many friends that I have made at Johns Hopkins, especially Steve Laventstein, Debjoy Mallick, Charles El-Mir, Meng Zhao, Amy Dagro and the aforementioned Gianna Valentino and George Weber. It's been a pleasure to share my Ph.D. experience with all of you.

I would like to thank all the staff members from the Johns Hopkins Department of Mechanical Engineering, especially Marty Devaney, Deana Santoni, Tom Benassi, Mike Bernard, Kevin Adams, Nancy Lippi, Rich Middlestadt and Matt Shaeffer.

Finally, I dedicate this thesis to my family. I cannot thank my parents enough for their love through all the years and raising me to be who I am today. My mother, who also received her Ph.D. from Johns Hopkins University, continues to be a huge inspiration to me and was there for me every step of the way. My darling daughter Alexis is such a wonderful blessing and a great source of joy for us. And finally, to my wife Veronica, I thank you for constantly putting up with me and for your love, support and sacrifice on this long journey. You are my rock and my muse, and I don't know what I would do without you.

Table of Contents

List of Figures

List of Tables

Chapter 1: Introduction

1.1 Motivation

Polycrystalline engineering alloys are used in many structural components, such as turbine blades and discs in jet engines, and the desire to improve their performance and lifetime has led the development of advanced micromechanical modeling tools through the Integrated Computational Materials Engineering (ICME) paradigm [1] and the Materials Genome Initiative (MGI) [2]. It has become increasingly clear that continuum multiscale modeling approaches, such as Crystal Plasticity Finite Element Methods (CPFEM), have the ability to illuminate the link between material processing, microstructure and properties in a way that has not been previously possible [3]. Whereas traditional FE modeling relies on convergent macroscale properties, the ability of CPFEM to explicitly represent the morphology and local crystallographic orientations of polycrystalline microstructures requires scale-specific, quantitative microstructural information for both input and validation. With rapid advances in computational capabilities and experimental techniques, ICME and MGI seek to build a strong connection between experiments and advanced, multi-scale materials modeling to better predict material behavior.

The development and implementation of experimental techniques for capturing behavior and microstructural properties at salient length scales are needed to inform the determination of representative volume elements (RVE) both with regards to accurately capturing microstructural details as well as observing size effects on material properties. Simply extrapolating from average microstructure descriptors doesn't provide

information such as specific grain size, shape and configuration with neighbors. These are features that can be captured experimentally through advanced characterization techniques, such as 3D serial sectioning [4]. Whereas traditional modeling efforts have made use of existing data in the literature to model a certain material behavior, the inverse, namely designing and tailoring experiments to obtain microstructure specific benchmarks for corresponding models is the most effective means for advancing ICME.

The work presented in this dissertation was undertaken as part of the AFOSR sponsored Center of Excellence in Integrated Materials Modeling (CEIMM), and its overall goal is to experimentally benchmark and validate multiscale CPFEM models of the Ni-base superalloy René 88DT. The specific goal of this work was to develop scale-specific mechanical benchmarks by capturing the mechanical response of microtensile samples in conjunction with characterizing their microstructure in 3D. As part of this effort, multiple test sample geometries were designed in an attempt to characterize sample volumes that were small enough to reasonably be measured and modeled while still providing a true polycrystalline response. Significant effort went into developing machining processes, and the test equipment and techniques required for obtaining the requisite data, at the various length scales that each of these samples represented. In addition, after observing a size effect on yield strength, a further study was done to investigate this phenomena by testing samples of different sizes and elucidating the mesoscale behavior of René 88DT.

1.2 Thesis Overview

The remainder of this thesis is organized into five chapters. Chapter 2 is a review of the relevant literature on microscale mechanical testing, microstructural

characterization, and ICME efforts. Chapter 3 is a description of three machining techniques (wire EDM, femtosecond laser machining and focused ion beam), and how they were adapted and optimized for making microtensile samples of René 88DT. Chapter 4 discusses microtensile testing of René 88DT performed to capture mechanical benchmarks and study microstructurally dependent sample size effects on yield strength. Chapter 5 discusses 2D and 3D characterization of mesoscale samples and the use of 2D digital image correlation (DIC) for generating local strain maps as an advanced benchmark for model predictions and to investigate the role of microstructural features in the deformation of René 88DT. Lastly, Chapter 6 gives a summary of the thesis and a discussion of related future work.

Chapter 2: Background

2.1: Introduction

This chapter presents a review of experimental efforts that have been made to manufacture, test and characterize microscale samples. The review begins by describing early microscale testing techniques and fabrication processes and builds up to modern emerging techniques in sample manufacturing such as femtosecond laser ablation. Then characterization techniques for measuring localized strain as well as advanced techniques for characterizing microstructure in 2D and 3D and their applications in terms of ICME will be discussed. The review concludes by describing René 88DT, the material of focus in the work of this thesis, as well as a brief description of the CPFEM model that is being developed for this material alongside the experimental efforts.

2.2: Evolution of Microscale Mechanical Testing and Fabrication

The development of microscale experiments is motivated by the desire to measure the local mechanical behavior of small volumes of material and to observe the role of both subgrain microstructure and mesoscale microstructure of grain ensembles or neighborhoods.

The whisker experiments of the 1950s and 1960s are among the earliest examples of mechanical testing at the micrometer scale. Most of whiskers tested in these experiments were single crystals, with the whisker axis parallel to a major crystallographic direction [5]. There was significant interest in the mechanical properties of whiskers after Herring and Galt demonstrated that whiskers had significant

strengths by bending Sn whiskers to very large elastic strains without evidence of plasticity [6].

Subsequent tensile tests on Fe, Cu, Ag, Cr, W, Ni and Co whiskers produced yield strengths close to the theoretical strength of dislocation free crystals [7]. This study by Brenner on perhaps the most exhaustive to date, and showed that whisker yield stresses scaled roughly with inverse sample diameter, a distinct and now well-known size effect of smaller being stronger [7]. One challenge faced in these whisker tension testing experiments was that the sample stresses at yield were so high that the samples shattered. Brenner developed a micrometer-operated brake, that dropped the sample stresses upon yielding, allowing a distinct yield point to be observed along with the plastic flow behavior [8].

While this early testing was limited in terms of the sample geometry that was utilized as well as the materials that could be tested, these microscale experiments, and especially the ability to use microtensile testing, were a significant step forward and provided some of the earliest evidence of size effects in small volumes.

In 1976, Tabata et al performed tension experiments on Al wires with diameters of 5 to 200 μm [9]. These samples were prepared by a process of wire drawing, annealing, electropolishing and then annealing again. The results from these tests showed that the critical resolved shear stress (CRSS) was affected by sample size, with 8 μm diameter samples showing a twelvefold increase in CRSS compared to the bulk scale measurement. Post mortem observations of the deformed wires showed that the degree of slip band localization increased with decreasing sample size. For samples with

diameters smaller than 60 μm, the CRSS seemed to scale as the inverse square root of sample diameter, analogous to the classic Hall-Petch relation.

Tabata et al further performed in-situ experiments on 5 μm diameter samples with a transmission electron microscope (TEM) and reported an increase in dislocation density near the sample surface prior to the formation of slip bands. Similar experiments were performed with Cu-0.15Ag samples and these wires were found to behave with the same inverse scaling, with CRSS going as the inverse square root of sample diameter. This experimental data is another early example of the typical school of thought that smaller is stronger with regards to sample size and microstructural features such as grain size [9]. At a somewhat larger scale, Suzuki et al conducted tension experiments on Cu single crystals with diameters ranging from 100 μm to 2 mm [10]. These tests showed an extended strain range at which easy glide flow behavior would be observed for decreasing sample diameter. They conducted similar experiments on alpha brass and similarly found an increased range of easy glide behavior for decreasing sample size as well. These tests demonstrated a further advance in combining microtensile testing with TEM characterization to describe observed events related to plasticity.

A significant advance in microscale sample preparation came when Uchic et al employed a new specimen preparation technique using focused ion beam (FIB) as a machining technique for fabricating micropillar specimens that range from sub-micrometer to several tens of μm in size for evaluating flow properties [11, 12]. An image of a FIB-machined micropillars after testing as well as stress-strain curves of pillars tested at different sizes is shown in Figure 2-1.

This test is similar to macroscopic compression experiments, however the microcompression samples are not freestanding; they are instead machined directly into a bulk piece of material. The load and displacement resolution of most nanoindentation systems are ideal for microcompression testing, allowing for the generation of engineering stress-strain curves with micro-strain and sub-MPa resolution [12].

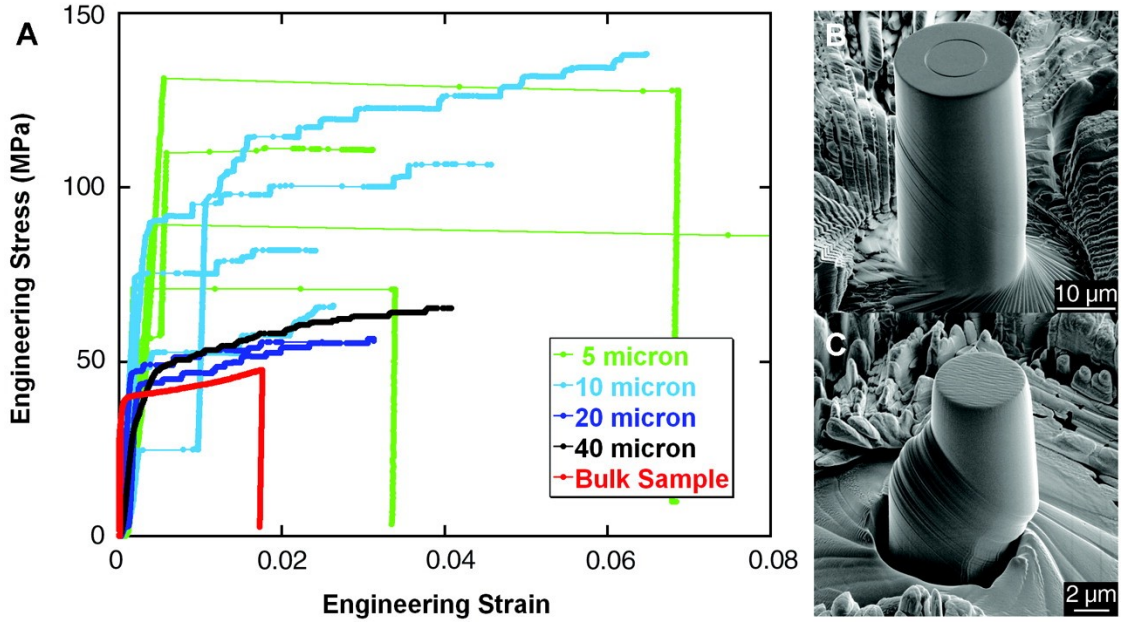

Figure 2-1: (a) plot of stress-strain curves for micropillar compression samples of different sizes demonstrating the stochastic behavior of samples at this length scale, (b) An SEM image of a 20 µm diameter microsample tested to 4% strain, and (c) an SEM image of 5 µm diameter microsample after testing, where the sample achieved 19% strain during a rapid burst of deformation [11].

With the development of FIB-based milling, the majority of microcompression samples have been fabricated with this technique as it allows for the manufacturing of microcompression samples into the surface of a bulk crystal with precise control over both the location and size of the sample [11-13]. Some samples have been milled with the

ion beam normal to the bulk surface [14-16]. These samples are easily produced by stock milling patterns, and therefore were more commonly used when the technique was first introduced. However, this methodology can complicate the interpretation of the microcompression experiments as the samples have some degree of taper leading to a nonuniform stress field within the sample, as well as a gage length can be much larger than the desired aspect ratio for single crystal compression samples. These effects were demonstrated by finite element analysis performed by Zhang et al [17]. To avoid this machining artifact, a procedure called lathe milling was developed where the ion beam is at an oblique angle to the bulk material [13]. This technique allows for both a uniform cross-section and accurate aspect ratio. In addition, lathe milling can be used to prepare samples that have multiple phases, while other milling methods may encounter problems with differential milling rates [15].

Despite the widespread use of FIB as a machining tool after these early demonstrations of the tool, one concern associated with FIB machining was the irradiation-damage layer that is created by the use of Ga+ ions. The impact of the resulting damage layer is dependent on parameters such as the atomic weight of the target material, bonding characteristics of the target material, the beam ion energy and the orientation of the incident beam [18, 19]. Greer and Nix attempted to assess FIB irradiation damage by examining Au microcrystals prepared by FIB milling compared to samples made using electrodeposition [20-23]. Their experiments showed that the microcompression flow-stress values for the three different FIB-based machining processes were similar, but the electrodeposited microsamples were slightly stronger on average, albeit with size-dependent trends. Based on these results Greer concluded that

the effect of FIB-irradiation damage was negligible. Shim, Pharr et al also studied the effect of FIB damage on mechanical properties during their investigation of Mo alloy micropillars [24]. They found that as grown single crystal micropillars tested in compression approach the theoretical yield stress. However, in the case of FIB machined micropillars the yield stress was an order of magnitude lower, and exhibited strain hardening and localized failure at the tip of the indenter as compared to the catastrophic collapse observed in the as grown micropillars. A further investigation in comparing FIB machined Mo micropillars to 4% and 8% pre-strained as grown pillars showed similar behavior between the two, however the pre-strained as grown pillars still showed higher average yield strengths than the FIB machined ones.

Shim, Pharr et al also investigated microhardness tests on a single crystal Mo sample exposed to 30 kV Gallium ions at a normal and glancing angle and compared with electropolished samples [24]. They found that the electropolished samples exhibited elastic behavior until pop-in effect consistent with onset of dislocation nucleation was observed. However, the FIB milled surfaces showed no pop-in activity and deviated from elastic behavior. In addition, hardness measurements at the FIB milled surface was twice as much as what was observed for electropolished samples. The results of these investigations in Mo alloys are corroborated in work done by Kiener et al who predicted significant effects on mechanical properties in modeling FIB machined Cu micropillars with 50 nm of amorphous damage [19]. Another study that examined irradiation-damage defects was done by Shan et al utilizing in-situ TEM tests [16]. They showed that most, if not all, of the dislocation substructure disappeared from sub-micrometer diameter microcrystals upon loading, a process they referred to as ‘mechanical annealing’. While it

is clear that a nontrivial amount of damage is induced by machining processes with Ga FIB, the damage is localized at the surface and only plays a significant role at the single digit micron scale and below as demonstrated in studies by El-Awady et al. [25, 26]

The machining automation capabilities associated with FIB allows for interrogation of properties at previously inaccessible length scales in a repeatable and efficient manner. Several years after the development of micropillars using FIB machining, the technique was extended to microtensile samples. Kiener et al. and Uchic et al. developed in situ SEM methods for tensile testing of single-crystalline metallic specimens fabricated using FIB methods [27-29]. The specimen and gripping configuration from Kiener et al. is shown in Figure 2-2 and was used for tensile specimens with sizes ranging from 0.5 μm to 8 μm. For the time, these were heroic experiments because of the hours of FIB machining time required to manufacture these samples, as well as the precise in situ testing that was performed.

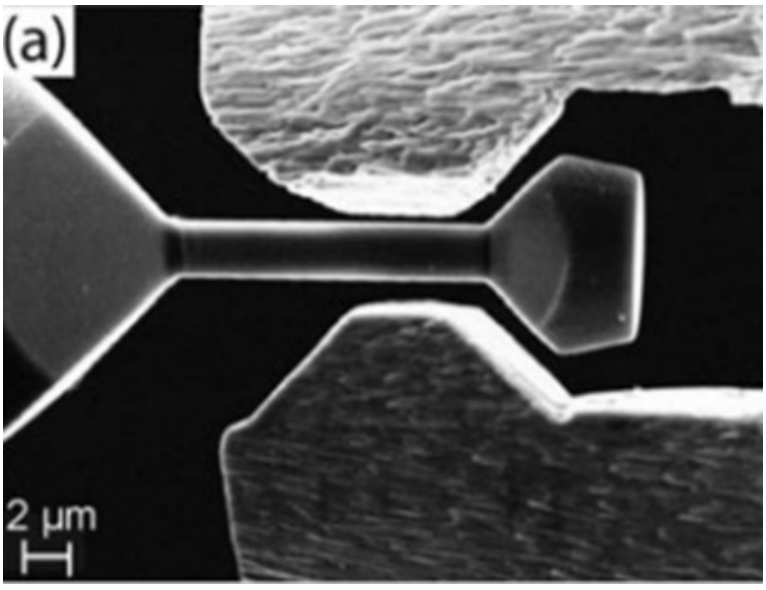

Figure 2-2: Image of microtensile and in-situ test grip mechanism prepared by Kiener et al.[27]

Although ASTM standards form macroscale tensile experiments [30], these standards are not always readily applied to microtensile testing and Kiener et al found that tensile specimens with aspect ratios of 2:1 or higher exhibited yield strengths that were significantly lower than equivalent compression experiments using the same FIB parameters and experimental testing apparatus. Further work in this area demonstrated that reversing the loading of a tensile specimen into compression does not alter the yield strength, however, lowering the aspect ratio of the tensile specimens that of the microcompression pillars yielded strengths similar to that measured from compression. These experiments highlighted the importance of boundary conditions in testing at the microscale and demonstrate the need to be cognizant of testing artifacts.

The application of the FIB has been further extended to machining of polycrystalline microtensile samples [31-34] as well as in microbending samples [35-39], making it a widespread tool in microsample preparation. However, challenges in using the FIB as a sample preparation tool still remain due to the scale at which it can be applied because of relatively slow removal rates and as mentioned previously, in machining more complex, multiphase materials.

While the trend of smaller is stronger observed in small volumes of single crystalline materials is scientifically interesting, this type of analysis precludes measurements of constitutive properties that makes microscale testing such a relevant technique. Other techniques traditionally utilized for macroscale sample preparation such as diamond saws and wire electric discharge machining (EDM) of for TEM applications such as tripod polishing have been shown to be able to prepare freestanding microtensile specimens from a wide range of materials [40], including thermal barrier coatings (TBCs)

[41]; TiAl [42, 43]; nanocrystalline Al [44], Cu [45], and Ni [46]; 316 stainless steel and Fe-Cu-Mn alloys [47]. Figure 2-3 shows an example of a sample nanocrystalline Ni machined using wire EDM [46]. In this sample, in order to achieve an appropriate level of surface roughness on the sample edges, further machining using diamond polishing papers and a rotary polishing tool were used.

The emergence of MEMS devices has also led to a need for developing techniques for testing thin film materials relevant to this application and length scale. The preparation of MEMS test specimens typically involves a combination of both additive and subtractive processes. Sharpe et al. describe a process of using photolithography to pattern a sample, followed by etching away excess material to achieve the final sample geometry [48]. An example of a polysilicon tensile specimen prepared this way is shown in Figure 2-4.

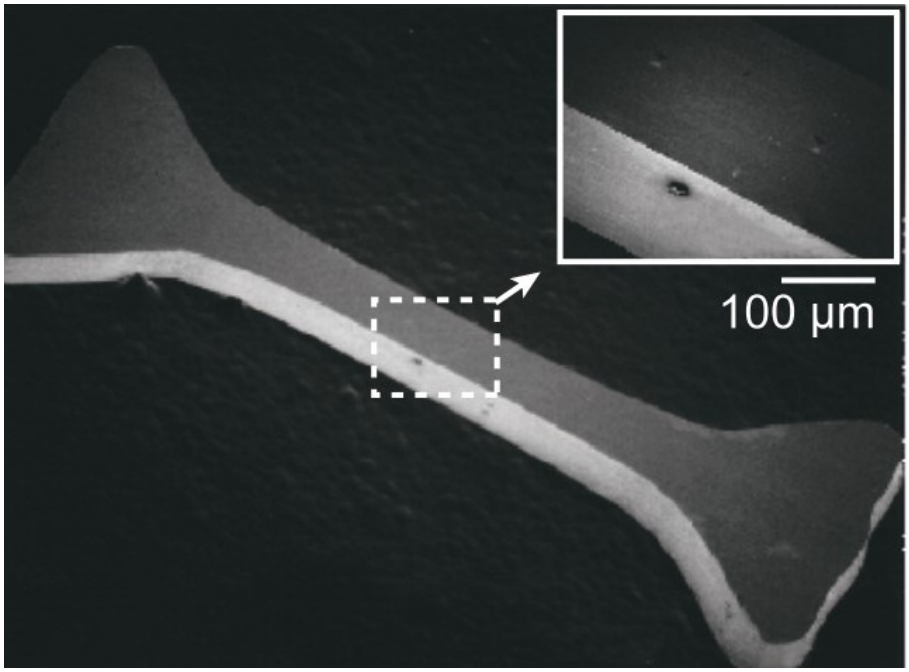

Figure 2-3: Image of microtensile Ni sample prepared by wire EDM and subsequent machining at the sample surface to minimize roughness [46].

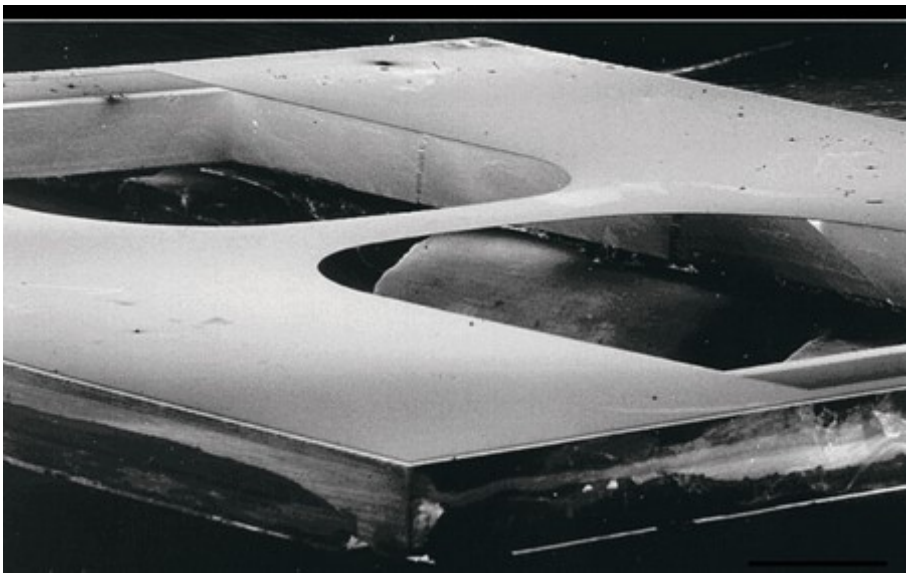

Figure 2-4: Freestanding polysilicon sample mounted on separate frame to improve structural rigidity [48].

This geometry is unique in that it features a frame around the sample to maintain its integrity for handling prior to testing. The ends are secured into a test machine, the two supporting strips are cut and the freestanding specimen gage section at the center that remains enables measurement of mechanical properties in a tension experiment. Pure LIGA Ni and LIGA Ni alloys can be electroplated into molds to make microtensile specimens that have wedge-shaped ends that fit into the matching grips of a small test machine. This technique was demonstrated in preparing Ni bowtie-shaped microtensile specimens 3 mm long and having a gage cross section of 200 μm by 200 μm [49]. This batch of specimens was electroplated into SU8 molds on a Si wafer and this process used to make what is referred to as LIGA Ni can be used to produce microstructures with very tight tolerances [50]. Deep reactive ion etching (DRIE) is a subtractive process, provides excellent resolution, and can also be used to fabricate microtensile specimens that are hundreds of microns thick [51]. DRIE has also been shown to be useful in making

microtensile samples for measuring fracture strength in silicon carbide from wafers that have been previously patterned and etched [52]. Rottmann developed another technique for fabricating framed thin film samples of Cu using a lift-off procedure [53]. An array of dogbone shaped plateaus was patterned onto a silicon wafer using negative photoresist and UV lithography. Then, a thing film of Cu was deposited om top of the silicon wafer, resulting in dogbone shaped samples attached to the wafer on each plateau. For each of the samples, a polypropylene frame was attached, and then the samples were lifted off using acetone. The result of the process was a set of freestanding Cu thin film dogbone samples with the frame already attached to make for easy handling.

Another emerging technique in sample fabrication is the use of laser machining samples at the microscale. Though the application of lasers for machining has been investigated since shortly after they were first developed [54], the effect of heating in short pulse (>10 ps) lasers precludes them from being applied for precise machining of microscale geometries [4, 55]. However, femtosecond lasers allow for material removal at an order of magnitude greater than what is capable with FIB machining, while still allowing for precise sample geometries. The short pulse duration of the femtosecond laser allows for ablation with virtually no heat affected zone or melting. Suzuki et al utilized femtosecond laser machining for making microtensile samples of a Ni-20Cr alloy to study deformation at grain boundaries. The samples had dimensions of 1200 μm wide, 3000 μm long and 10–250 μm thick, however the machining process was not well investigated as part of the study [56]. Slaughter et al demonstrated the use of femtosecond laser in machining microtensile samples in 15 μm thick foils of Ta [57]. More recently Pfeifenberger et al published work done using a two-chamber setup, with

one chamber containing a femtosecond laser for machining and the second a dual-beam FIB-SEM system [58]. This setup was utilized to rapidly machine microcantilever beams of W with dimensions of 420 ×60 ×25 μm. In this work, the feasibility of nanosecond laser is also investigated and Figure 2-5 shows the melting at the sample edge with the nanosecond laser that doesn't happen when using femtosecond laser as seen in Figure 2-6, demonstrating the power of the femtosecond laser in machining at this length scale [58]. However, the samples machined by this laser system would still require some cleanup with the FIB to reach the desired sample dimensions, similar to the work done by Lavenstein et al. in machining cantilever samples with femtosecond laser and FIB [39].

2.3: Strain Measurement in Microscale Samples

In addition to determination of mechanical properties of tested samples to be used for benchmarking, the local deformation behavior also needs to be determined in order to compare directly with simulation results. For a geometry as small as a microtensile specimen, traditional contact methods for measuring strain such as strain gauges or extensometers prove to be difficult, if not impossible to use and so other methods have been developed over time.

Espinosa et al performed tensile tests by pushing an Au film that is fixed at each end. The vertical deflection along the film was measured by interferometry and converted into elongation. While this is a novel concept, this technique is only able to be applied to a very specific test and geometry, and certainly could not be well adapted to a microtensile experiment [59, 60]. Haque & Saif constructed a test system that combines

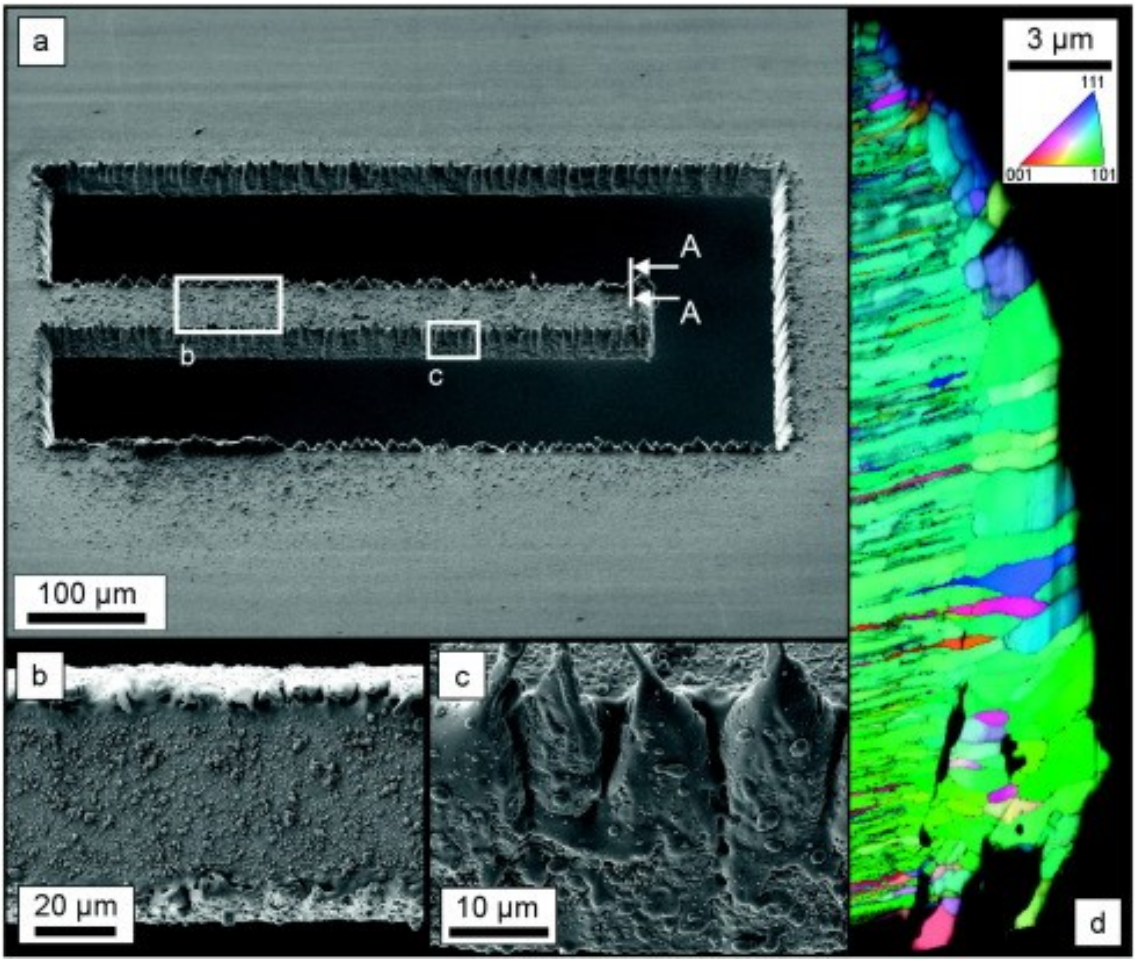

Figure 2-5: A cantilever fabricated by a nanosecond laser in a foil with a thickness of 25 µm is displayed in (a). The magnified top view (b) shows rough debris. The magnification of the cut edge shows a melted surface and a distinct burr (c). An EBSD analysis of the cross-section A-A indicated in (a) reveals coarsened and equiaxed grains in the heat influenced zone (d) [58].

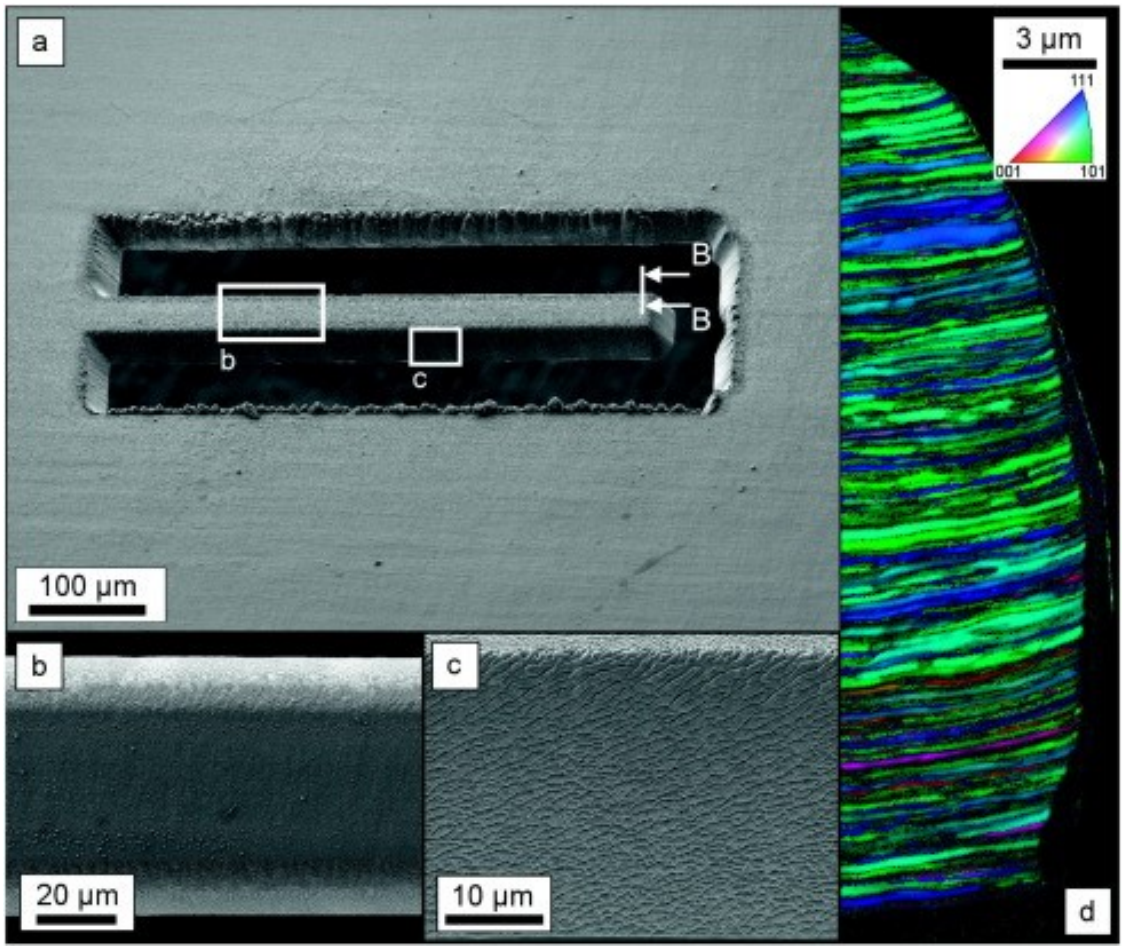

Figure 2-6: A cantilever fabricated by a femtosecond laser in a foil with a thickness of 25 µm is shown in (a). In the magnified top view (b) less debris is found than for the nanosecond laser processing. The magnification of the cut edge exhibits the characteristic laser induced periodic structures (c). An EBSD analysis of the cross-section B-B indicated in (a) reveals no grain coarsening near the cut edge (d) [58].

the test machine and the specimen into a single part, which is tested in an SEM and deformed with a piezoelectric actuator.

Observation of the displacement of two sets of markers deposited on the sample allowed for determination of overall elongation of a thin film specimen [61]. Simply attempting to determine strain from grip displacement as is done in macroscale tensile testing is made difficult by the compliance of a large test machine relative to the small sample geometry being tested. Greek & Johansson developed a method for removing the effect of sample compliance, however it can only be used if the compliances of the specimens are sufficiently different and with other potential errors it is best to measure strain directly from the gage of the specimen rather than relying on these grip displacement measurements [62].

Direct strain measurement at the microscale is a challenge, but great advances in the field have been made in the 15-20 years. One of the first noncontact methods developed for measuring strain in microtensile samples was interferometric strain displacement gage (ISDG). In this technique, two reflective markers are placed on a sample and illuminated with a laser, generating fringe patterns. As the sample strains, the motion of the fringe pattern can be sensed with photodiode arrays and converted into strain [63]. A few examples of markers used in this method were FIB-deposited lines of Pt or vapor deposited lines of Au lines of Au on a polysilicon sample as can be seen in Figure 2-7 [64].

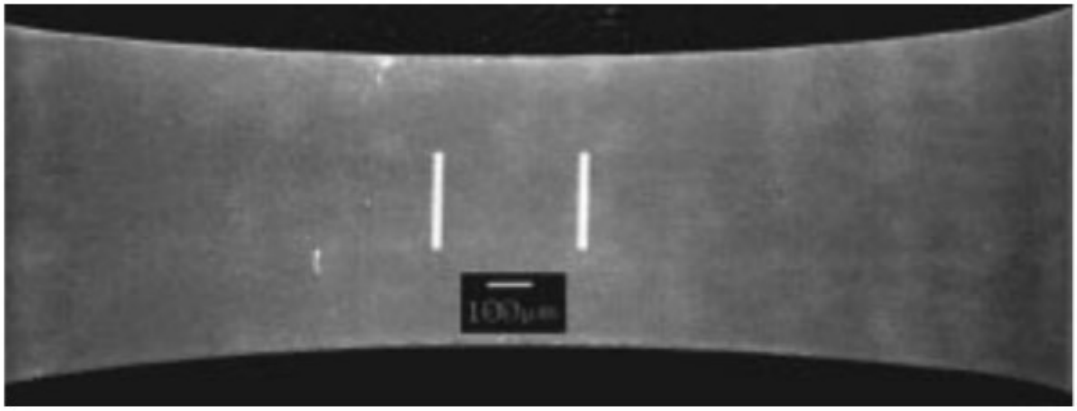

Figure 2-7: Image of Au lines deposited on a microtensile samples of polysilicon [64].

This technique enabled both measurements of normal and transverse strain and therefore allowed for the determination of the Poisson's ratio in tested samples. Another technique for marking samples was the use of microhardness indentation. Particularly in metallic samples, these indents make excellent reflective markers for the ISDG technique and are easier to apply. A more computationally based method is differential digital image tracking (DDIT), which tracks two or more markers in a series of images of the tensile sample gauge [65]. These markers can be either reflective lines applied to the sample or ceramic particles. This technique differs from the ISDG technique in that it uses image processing and correlation rather than fringe patterns.

However, the most prominent noncontact method for measuring strain that has been developed is digital image correlation (DIC). A pattern of markers is applied to the sample surface, typically referred to as a speckle pattern because of its appearance. In order for the correlation to perform well, the pattern either needs to appear bright against a dark background (in this case the sample surface), or dark against a bright background. The reason for this is that the correlation algorithm works by dividing the region of

interest into subsets. Each of these subsets is tracked as it deforms and the correlation to the subset in the original image depends on a grayscale intensity function. The correlation coefficients of subsets of consecutive images are calculated and plotted versus their position. The maximum correlation coefficient is then located that is representative of the optimal fit between the subsets of the two images. From this correlation, displacements can be calculated and therefore global strains can be calculated, as well as local strains in observing local displacements in subsets from image to image.

The most important aspects of DIC are being able to produce a high-quality speckle pattern and having an imagining technique with the resolution necessary to resolve said speckle pattern. Recent progress in developing high resolution speckle patterns has led to the ability to observe strains at very localized subgrain regions. Kammers et al made use of gold nanoparticles to create speckle patterns with features on the order of 30 nm. Through imaging of these particles in in an SEM, DIC with a resolution of 4 nm/pixel was reported, which is unprecedented with this correlation technique [66]. Figure 2-8 shows an example of this speckle pattern in an SEM image. One important consideration in performing DIC with high resolution SEM images that Kammers addressed was distortions in SEM images. Through the use of high magnification to reduce spatial distortions, as well as low accelerating voltages, large spot sizes, long dwell times and low working distances to reduce drift distortions, Kammers was able to develop guidelines for applying this technique with minimal distortion effects [66].

Stinville developed a novel technique using the γ’ particles after a heat treatment in René 88DT as the speckle pattern [67]. The nm sized features allowed for high

resolution DIC in a fatigue sample to observe crack nucleation. Figure 2-9 shows the results from using this DIC method to observe intragranular plasticity from the fatigue testing. These high-resolution methods along with others provide the way to improve the resolution of DIC measurements, and further improvements to the technique could be made with higher resolution imaging with reduction in noise.

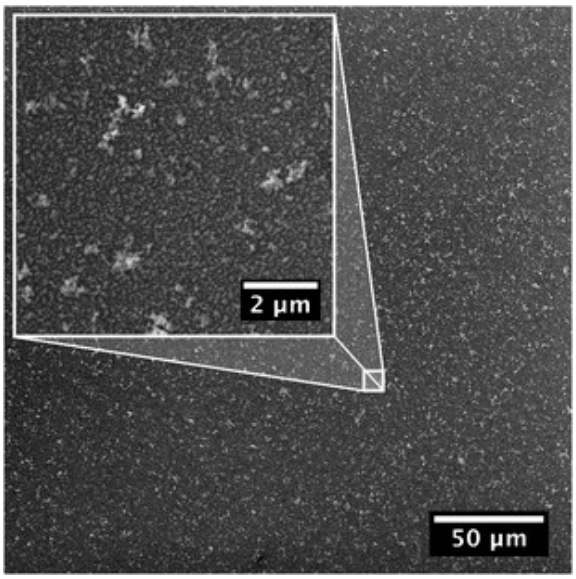

Figure 2-8: 30 nm diameter Au nanoparticles immobilized with MPMDMS on the surface of an Al substrate [66].

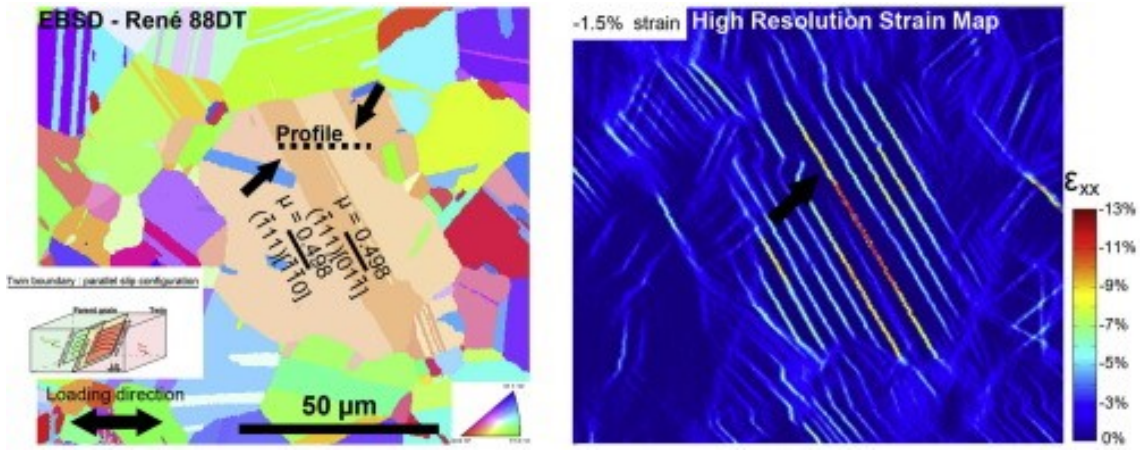

Figure 2-9: EBSD map and corresponding high resolution strain map of a neighborhood of grains near a fatigue crack in a René 88DT sample [67].

The technique of DIC has been demonstrated to work with images that can be obtained optically, in a SEM and from AFM scans, showing that it is a versatile technique in terms of the materials it can be applied to and the independence of scale as strain is a dimensionless quantity. A disadvantage of these methods is that postprocessing is required, which can take a substantial amount of time depending upon the resolution of the captured images and the pattern applied to the sample surface. This makes it a challenge to make in situ full-field strain measurements during a test, though a method for doing so was presented by Tao et al in measuring strain in polymer sample during fatigue testing [68].

2.4: Characterization in 2D and 3D and Applications in ICME

In the ICME paradigm, the need to connect modeling and experiments is evident, but the ability to do so has been limited in the past both by the need for more computational power as well as more detailed explicit microstructural information from experimental results. In terms of experimentally capturing microstructure in 3D in parallel with mechanical properties for benchmarking, most efforts have been limited in some way. Some previous studies have attempted to benchmark using a simpler method of characterization and modeling. Becker et al utilized only the surface orientation data of an Al sample to develop two finite element models: a plane strain model and a quasi-3D model with a mesh that was only one element thick [69]. Cheong et al performed a similar modeling effort using experimental data collected by Zhang for a polycrystalline sample of Al–0.5% Mg [70]. The model utilized a finite element mesh of 35 x 31 x 3 elements on a subsection of the sample gage and compared distributions of plastic axial strain with the experimental results as well as the macroscopic stress-strain behavior [71].

These studies demonstrate some early efforts to connect experiments and modeling despite both experimental and computational limitations. However, the drawbacks of not being able to model the full 3D structure of a tested sample is significant. The effect of boundary conditions as well as subsurface microstructure plays a significant role in deformation. In order to sidestep the need for full 3D characterizations, early ICME efforts have studied materials with microstructures that can be characterized well using only 2D methods. These materials tend to have either very coarse microstructures or columnar structures that maintain their surface microstructure through the thickness of the sample. These structures can be achieved either by the processing methods used to produce the material, such as directional solidification [72] or extraction of oligocrystals [73] or some heat treatment to coarsen the material [74, 75]. A multitude of ICME studies on oligocrystalline structures has been carried out in materials that include Zirconium alloys and near-gamma titanium aluminides [76], polycrystalline columnar Al [72, 74, 77], single and bicrystal stainless steel [72], hot worked waspaloy-ingot specimens [78] and coarse grained tantalum [75]. Figure 2-10 shows an example of a comparison of experimental and modeling results in ICME effort performed on one of the columnar Al samples modeled by Zhao et al [74]. The simpler microstructure of this material makes it easier to characterize and subsequently model the full structure of the sample. The ability to model the full sample gage in 3D allows for a more accurate approximation of the true boundary conditions experienced by the sample during an experiment and provides a more accurate prediction of the deformation response.

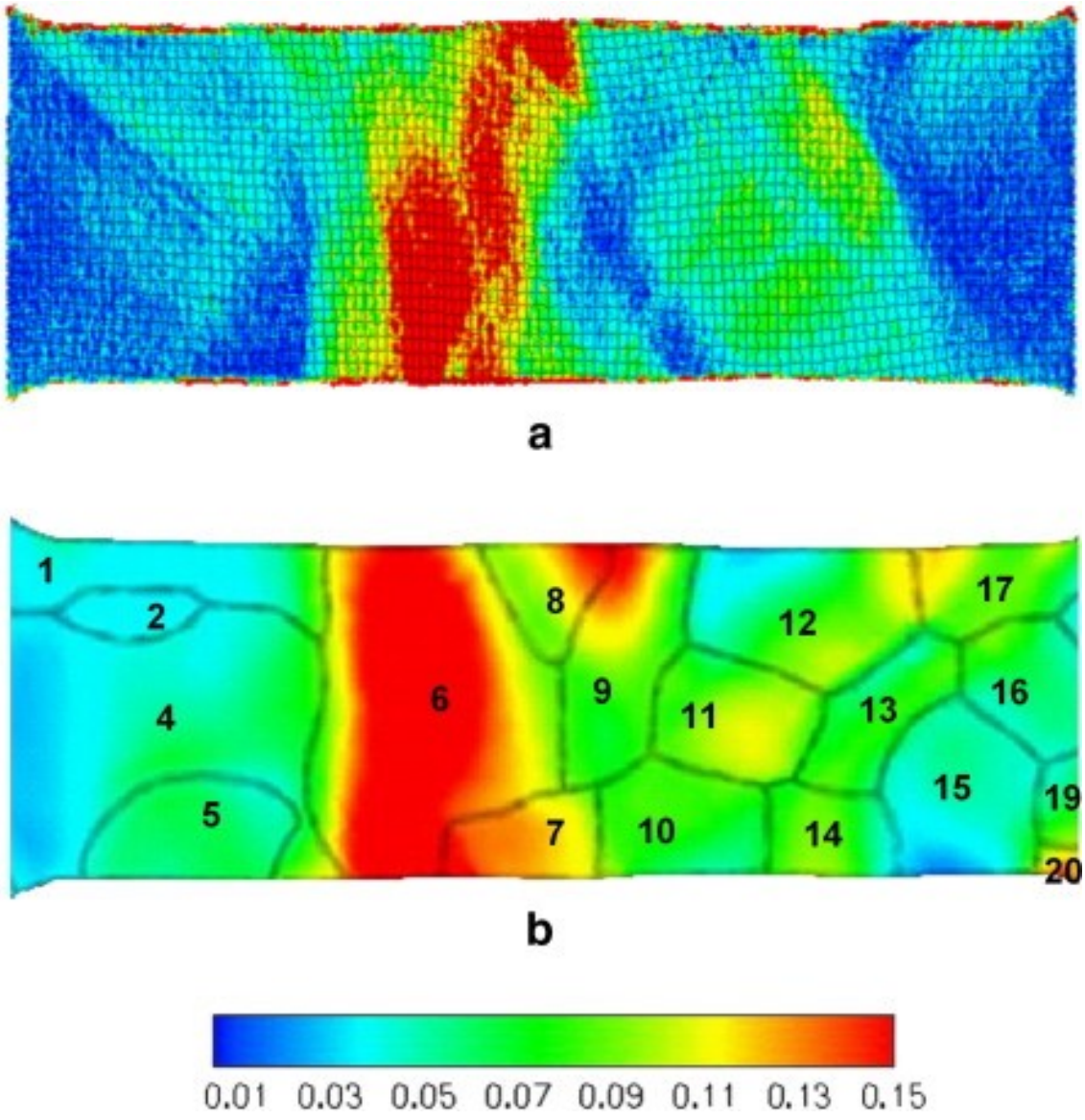

Figure 2-10: Comparison of axial surface strain mapping between: (a) experiment and (b) simulation in an Al oligocrystal [74].

While these studies provide an inventive means of explicitly characterizing and modeling the microstructure of a sample, it is clear that there is a limitation imposed both in terms of the sample size and type of material that can be investigated in this way. Many of these materials don't represent true structural materials or materials with complexity at multiple length scales. In addition, the processing to achieve these specific

coarse-grained and columnar microstructures is not typically indicative of the conditions actually used for a material put into service.

Another technique that has been utilized when only 2D microstructural data is available is the use of statistics to extrapolate a 3D microstructure from a 2D EBSD scan, such as what St-Pierre did for modeling TiAl and grade 702 zirconium [79]. This novel modeling approach is however impossible to truly compare one to one with experimental results as even slight changes in the subsurface microstructure can lead to significant deviations in the observed behavior at the sample surface.

In order to truly observe, and therefore model, polycrystalline materials in 3D, further development of experimental methods in terms of characterization are required. The preeminent experimental technique for building a 3D dataset involves serial sectioning of samples. The 3D microstructural information is collected by destructively slicing the sample layer by layer and characterizing each newly exposed surface before performing the next sectioning step. The acquired set of 2D scans can be stitched together to provide a 3D representation of the sample microstructure. Musienko was one of the first to characterize and model a sample using this methodology by removing layers from a tested Cu microtension sample [80]. A small subsection of the gage containing about 100 grains was characterized in this manner and used to generate a finite element simulation of the 3D structure. Although this subsection did not represent the full microstructure of the sample, this was one of the first times that a modeling effort had been performed on a sample characterized in 3D. Methods such as electropolishing or physical grinding can be difficult to utilize for sectioning an entire sample, especially for samples with dimensions at the micron scale. There is more variability in the slice

thickness that can be achieved and in terms of electropolishing, materials with multiple phases and alloying elements make it difficult to section at a consistent rate. Spanos, Lewis, Rowenhorst and co-workers at the Naval Research Laboratory combined serial sectioning using a Buehler Minimet system and characterization with EBSD to develop 3D datasets of stainless steels and Ti alloys to connect with FEM models. More automated methodologies using mechanical sectioning, such as the Alkemper-Voorhees micromiller developed at Northwestern University [81] or the Robomet.3D system developed at the Air Force Research Lab [82, 83], were major advances in streamlining workflows for 3D dataset collection.

Within the last decade or so, the use of more advanced sectioning tools and methods has allowed for better studies of microstructure in 3D. The use of FIB as a sample machining tool has already been discussed, but its application for serial sectioning is an obvious application as well. In dual beam systems equipped with both an SEM and FIB, serial sectioning and EBSD can be performed and automated in a routine manner. Uchic, Groeber et al were some of the first to demonstrate this technique in sectioning samples of the nickel-base superalloy IN100 [84, 85]. A schematic of the dual beam system demonstrating the methodology for tilting the sample to utilize both beams is shown in Figure 2-11. Shortly after, Zaafarani et al made use of FIB serial sectioning in characterizing the microstructure surrounding a nanoindent in Cu and developing a finite element model from the collected data [86]. In terms of utilizing this technique for characterizing and modeling a full sample volume, the applications can be limited because of the material removal rate of the FIB, especially depending on the material to

be sectioned. One study that did yield positive results in this regard was carried out by Shade et al on microtensile samples of polycrystalline Ni [31, 87].

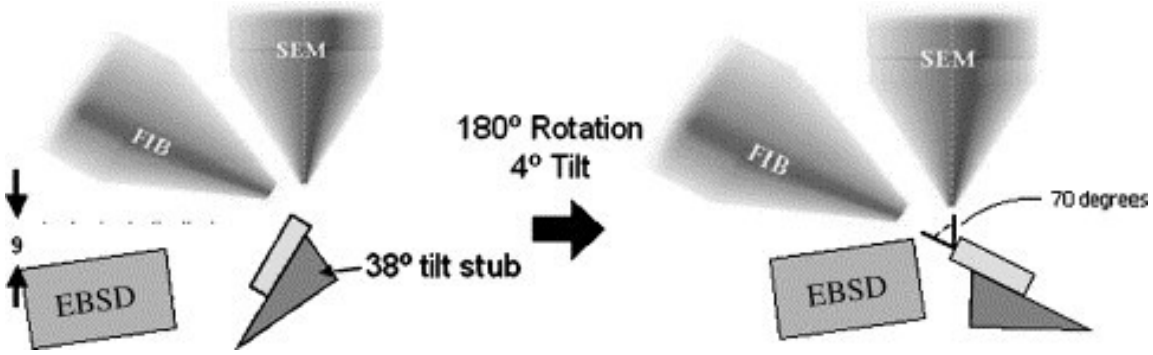

Figure 2-11: Schematic of dual beam system for collecting 3D microstructural information. The sample is tilted between imaging with the SEM to collect an EBSD scan of the sample surface and ablation with the FIB to remove a layer of material [85].

Using a dual beam FIB-SEM system, multiple samples with gage dimensions of width of 21 μm, a thickness of 38 μm, and a gage length of 80 μm were characterized in 3D and in combination with surface strain maps collected during testing used to later benchmark a finite element model using these explicit representations of microstructure [88]. Figure 2-12 demonstrates some of the 3D microstructural data that was obtained from the Ni samples. While these examples demonstrate the ability of the FIB as a sectioning tool, it is clear that sample size and material limitations due to the material removal rate of the FIB can limit what can be done despite the level of precision that can be achieved.

A more recently introduced tool for collection of 3D data at a larger scale is the UCSB Tribeam system which incorporates a femtosecond laser into the previous FIB-SEM dual beam platform as seen in Figure 2-13.

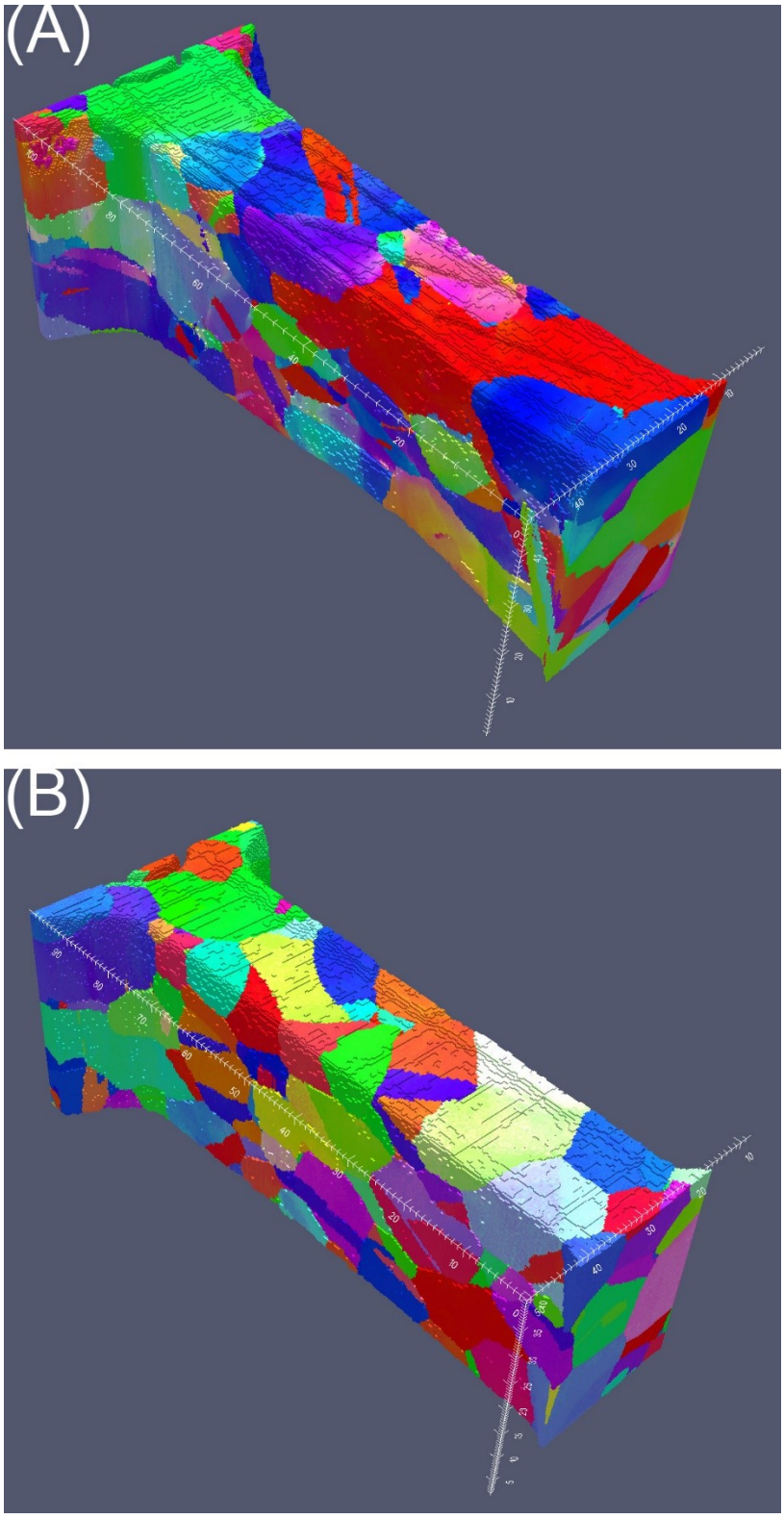

Figure 2-12: 3D reconstructions of two of the deformed Ni polycrystalline micro-tensile samples [31].

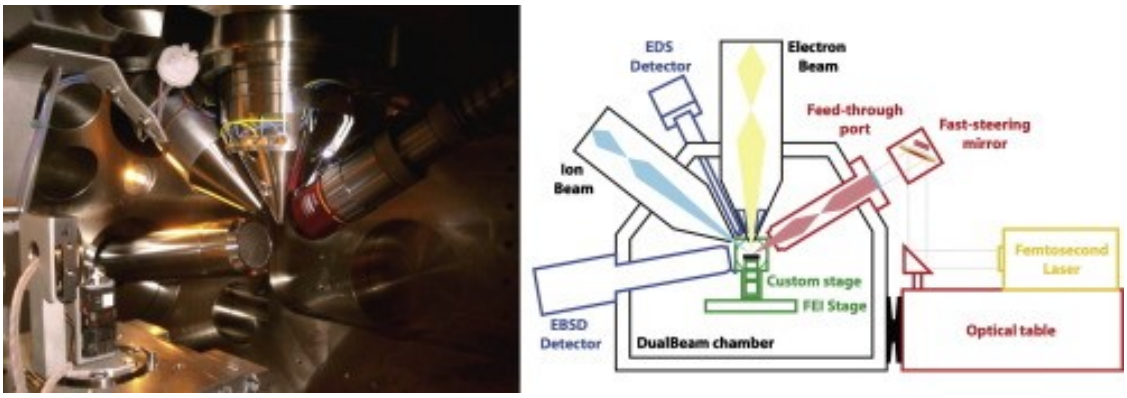

Figure 2-13: (Left) An image of the inside of vacuum chamber is shown with the EBSD camera inserted and the stage door open. (Right) Schematic of the TriBeam system with Ga + source ion beam, femtosecond laser, electron beam, and EBSD and EDS detectors [89].

The material removal rate of the laser allows for ablation at orders of magnitude faster than what was possible with FIB. In addition, the mechanism of ablation with the femtosecond laser makes the system more independent of the material being sectioned than with FIB [89]. As a result, the Tribeam is an incredibly versatile system both in terms of the speed and scale at which material can be characterized in 3D as compared to in the past. One very successful application of the Tribeam in this area is in the work of Stinville et al in characterizing crack nucleation in René 88DT. Fatigue samples of the material were tested and subsequently sectioned and characterized in the Tribeam. Using this information, detailed studies of crack nucleation sites at the interior were performed in order to determine what features in the microstructure led to crack nucleation and propagation [90]. From this, further work was done to develop a statistically-based criteria for crack nucleation which could be utilized for informing and benchmarking fatigue models and used in the development of synthetic microstructures. However, the use of this tool for explicitly characterizing microscale samples is still being investigated.

Another emerging tool in serial sectioning and 3D characterization is the Plasma FIB (PFIB). Using Xe rather than Ga as in a traditional FIB, the PFIB allows for material removal rates at the same order of magnitude as the femtosecond laser, but with less damage. Kwakman et al demonstrated that compared to Ga FIB machining, the damage layer when using Xe FIB could be reduced by up to 25% [91]. Xiao et al demonstrated that micropillars of Al, a material particularly susceptible to the effects of Ga implantation, machined with a Ga FIB showed lower yield strength than micropillars fabricated with Xe FIB [92]. Burnett et al have demonstrated the use of PFIB in serial sectioning and 3D characterization as well on a WC-Co sample [93]. Though these two tools have not yet been utilized well for explicit sample geometries, the step forward that they provide in terms of 3D characterization is very promising and optimization for sectioning at a smaller length scale could allow for collection of statistics and 3D datasets for benchmarking at a rate that was previously inaccessible.

Another emerging technique for characterizing material in 3D is the nondestructive technique of High-Energy Diffraction Microscopy (HEDM). HEDM utilizes diffraction patterns produced by a monochromatic beam from a synchrotron source to interrogate a volume of material. Two sets of detectors are used to collect information from the sample. One located only a few mm from the sample is used for near-field HEDM and can provide orientation maps with spatial locations of grains as well as their morphology and misorientation relative to neighboring grains [94]. The second detector is placed much further away and is used for far-field HEDM which provides grain centroids and elastic strain tensors [94]. These datasets combined provide a robust representation for the sample microstructure, as well as subgrain information

[95]. Many examples of using this technique for 3D characterization have been demonstrated [96-101]. However, the major benefit of this technique in terms of ICME is not just that it is nondestructive, but that it can be used to capture 3D microstructural information in situ rather than from a postmortem sample. Marguiles et al demonstrated the use of HEDM at ESRF to investigate deformation of a single grain within a Cu sample during loading [102]. The technique utilized involved loading the sample incrementally a performing a rotation in between loading steps to gather diffraction data in order to determine the strain tensor within the grain and how it developed throughout the test. Oddershede et al performed an HEDM experiment on a steel sample in a very similar manner but oriented the tensile axis to be vertical with respect to the beam [103]. In addition, this experiment did not simply study a single grain during testing, but rather about 200 grains, demonstrating the improvement in this characterization technique. More recently, Schuren, Shade et al have developed a load frame for in situ HEDM experiments known as the rotation and linear axial motion system (RAMS) [104, 105]. This load frame allows for the use of μ-CT, far-field HEDM, and near-field HEDM concurrently during a tension or compression experiment while also being able to rotate the sample 360 degrees. An image of this device is shown in Figure 2-14 to give an idea of the complexity of the system and its configuration with each of the detectors. In terms of ICME efforts, in one instance this tool was utilized to collect a HEDM dataset for a Ti-7Al sample that was then used to instantiate a CPFEM simulation to compare with [106]. The model showed a good correlation with experimental results and this work demonstrates the advantage that the HEDM provides in being able to observe the stress states of buried grains has over other techniques such as surface DIC that only allow for a

2D observation of deformation on the surface of the sample. However even a detailed experiment as this still shows some of the limitations of the technique. The resolution of the measurements spatially is limited by how focused the beam can be, usually on the order of a few microns, and the resolution of the detector.

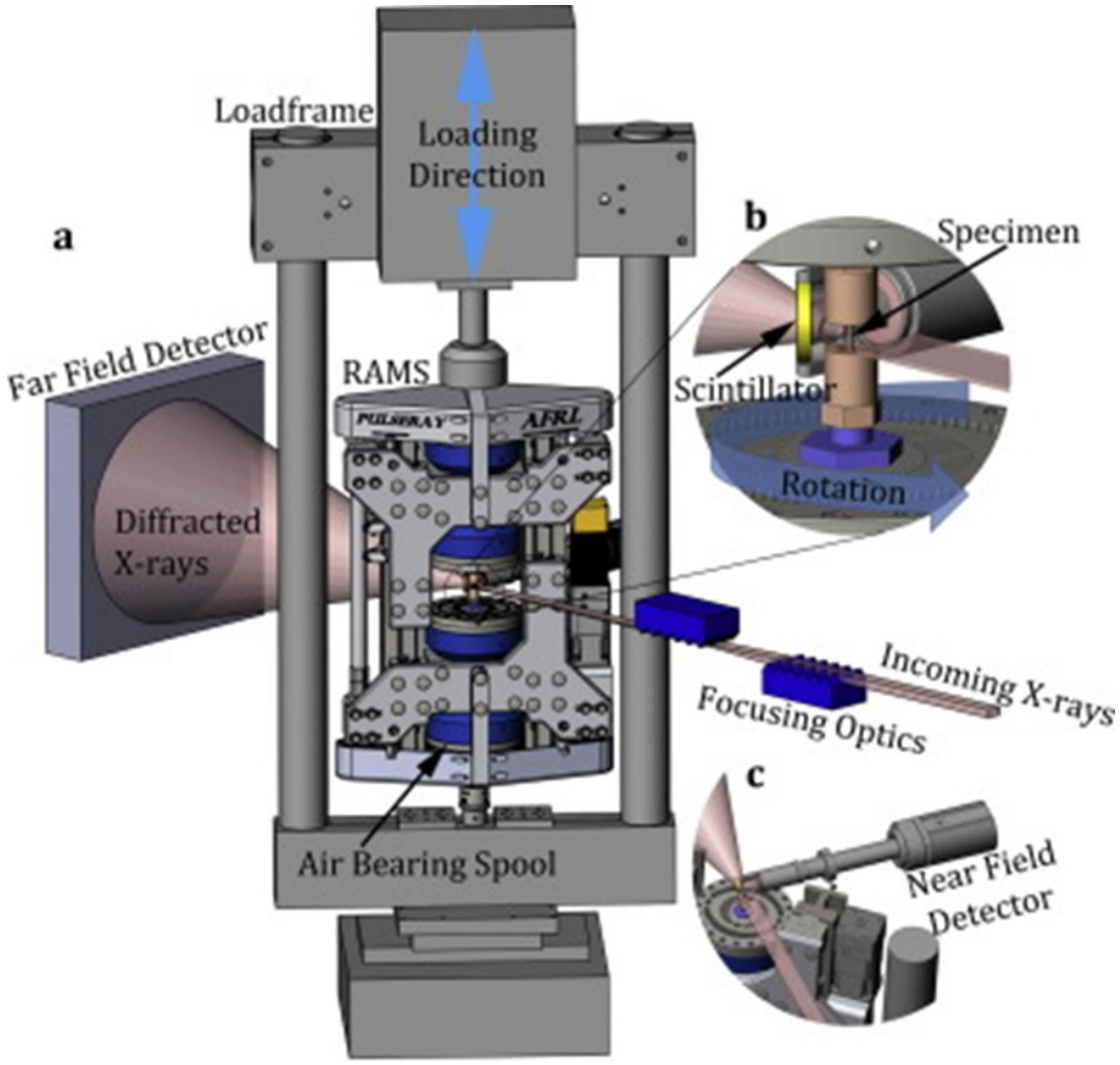

Figure 2-14: Schematic of RAMS load frame showing (a) overall view of the system, (b) magnified view of sample-beam interaction and rotation stage, and (c) orientation of near field detector relative to the sample [104].

The way the experiment is run requires that the loading be performed incrementally in order to collect diffraction data. This can cause difficulties in observing the deformation if the sample relaxes or if the stress state of a grain changes at all during these instances when the load is held constant. Finally, the ability to utilize HEDM not only because of limited access to a synchrotron system, but also in the effort and knowledge required to reconstruct a dataset, limits the accessibility of this technique greatly. Despite these shortcomings though, the use of HEDM for microstructural characterization provides a level of detail that can't be obtained with other 3D characterization techniques and is nondestructive allowing for the sample to be preserved for further characterization or tested to failure in order to observe fracture. With further improvements to the techniques and equipment, as well as further proliferation of the knowledge required to perform these experiments, HEDM could be a more common technique in materials characterization and specifically in ICME efforts.

2.5: Overview of René 88DT

The material that was investigated in the study presented in this thesis to develop experimental benchmarks for CPFEM simulations is the polycrystalline Ni-base superalloy René 88DT. The material has a nominal composition (wt %) of: 56.46 Ni, 13 Co, 16 Cr, 4 Mo, 4 W, 2.1 Al, 3.7 Ti, 0.7 Nb, 0.03 C and 0.015 B. This alloy is processed through a powder metallurgy route and as such contains a high volume fraction of annealing twins. It exhibits exceptional strength, even at very high temperatures making it ideal for its primary use in turbine engines [107].

Figure 2-15 shows images of the microstructure of René 88DT at the polycrystalline level (Figure 2-15a) and an intragranular or subgrain level (Figure 2-15b). The morphology of the subgrain structure is γ channels surrounding the larger secondary γ‘ precipitates in addition to much finer tertiary γ’ particles in the channels. These γ‘ particles have the $L1_2$ crystal structure and an ellipsoid shape with a diameter of a few hundred nanometers whereas the tertiary particles are much smaller than that, on the order of hundreds of angstroms. The matrix phase, γ, is a Ni solid solution with an FCC crystal structure [108].

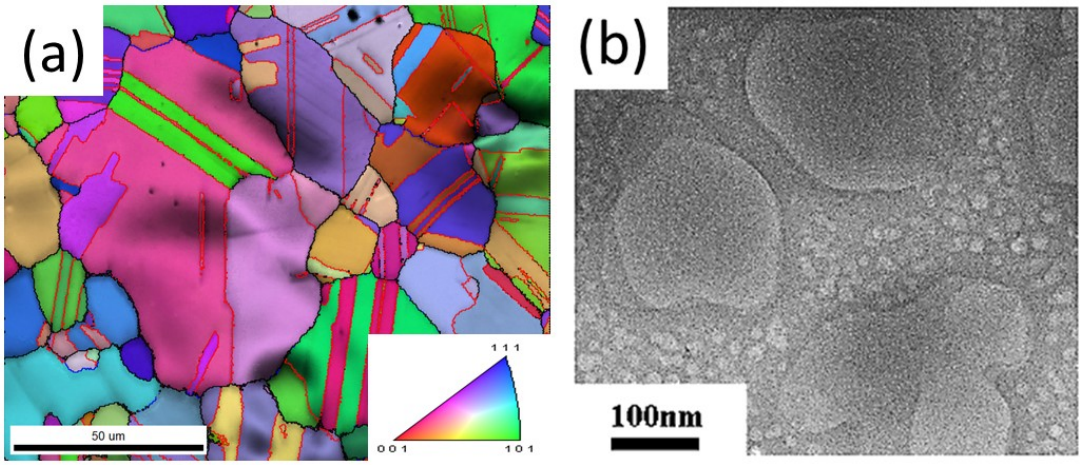

Figure 2-15: (a) Image of grains and twins in René 88DT captured with EBSD and (b) SEM image of subgrain γ- γ’ morphology (Copyright 2008 by The Minerals, Metals & Materials Society. Used with permission.) [109].

This material is a fascinating candidate for multi-scale modeling because of the features that exist within the material at multiple length scales. At the subgrain scale the two-phase microstructure gives rise to properties that affect higher order scales, especially in terms of the high temperature properties related to dislocation activity [107]. At the polycrystalline scale, the large volume fraction of twins adds complexity in terms

of being able to model these finer features as well the various boundaries that exist. A description of a CPFEM model to approach this multiscale problem is given in [110]. The model endeavors to represent the morphology of the subgrain structure in order to subsequently homogenize and develop a single crystal model. This single crystal model is then brought up to the polycrystalline scale at which individual grains are organized together to represent the microstructure of the material, including twins. The simulation predictions observed at this scale will serve as a means for direct comparisons and benchmarking with the experimental results captured at the mesoscale.

2.6: Summary

The advances in test methods at the microscale has been a remarkable development in terms of ascertaining localized and microstructure dependent material behavior. While early microscale measurements were made in single crystals of pure materials, the development of more advanced machining techniques has allowed for the characterization of more advanced materials that could not be machined using previous methods. In addition, microscale testing techniques of fragile materials such as thin films was made possible by the development of novel test structures and load frames that could be further applied in other applications as well.

Alongside the ability to machine and test samples at an expanding number of sizes and for a multitude of materials, characterization methods such as DIC to observe strain and local deformation behavior, as well as 3D techniques for characterizing microstructure have led to the ability to interrogate material behavior at extremely fine length scales. In addition, these advances in property and microstructural characterization

have supported the development of more informed models and modeling techniques such as CPFEM have allowed for the explicit representation of microstructure in-silico. Though significant progress has been made in terms of ICME to date, most work has been done in pure materials and structurally complex materials such as René 88DT remain a challenge. As such, the continued development of techniques to machine, test and characterize microtensile samples of this material is required in order to obtain the requisite information needed for model development and benchmarking.

Chapter 3: Microtensile Sample Machining Methods

3.1 Introduction

As was discussed in Chapter 2, miniaturized mechanical testing has become a widespread technique for studying material properties and provides ample benefits as compared to more traditional mechanical testing through the use of macroscale test samples. Smaller test samples allow for the ability to capture the influence of microstructure and measure local properties that can't be observed in traditional macroscale testing [111-113]. Capturing these scale-specific properties is critical to benchmarking and development of multiscale CPFEM models.

However, sample quality at smaller length scales can have a significant effect on the measured sample response. Poor quality samples, especially in terms of surface roughness, can lead to premature failure during tensile loading and that can provide inaccurate results, which can be especially troublesome when there is some uncertainty in the expected outcome of an experiment. ASTM standards give some guidelines in terms of a target of quality and dimensions of tensile samples but don't necessarily provide a methodology and best practices for fabricating samples, especially at the microscale [30]. At this length scale, more traditional machining methods aren't applicable because of the limit to the dimensional tolerance that they can achieve, and due to the surface finish that they produce. Many microscale machining methods are becoming more and more prevalent in the community but require the knowledge of the proper tools and their operation.

The three microtensile sample preparation techniques that were utilized in the studies of René 88DT presented in this thesis are focused ion beam (FIB), femtosecond laser and wire electric discharge machining (EDM). The FIB and wire EDM have been utilized for a variety of applications in the past, however the scale at which these techniques are applicable is limited. By comparison, the use of a femtosecond laser, though still an emerging technique for microscale machining, allows for samples to be made at a scale that bridges the gap between FIB and wire EDM. The discussion that follows in this chapter will cover procedures and best practices for machining high quality microtensile samples with each of these techniques. It will demonstrate and compare the level of sample quality between each of these techniques and its impact on the mechanical response of the samples. Lastly, it will discuss how these techniques can be combined to improve workflow and efficiency in machining at multiple length scales.

3.2 Extraction and Preparation of Foils from Bulk Material

Before machining of the final microtensile sample geometries, thin sheets or foils had to be excised from a bulk piece of René 88DT and polished to the proper thickness and surface finish. The foils were prepared to have a specific final thickness that would allow for samples having a square cross section to eventually be machined. Initially, slices of material were cut from a bulk piece of René 88DT using wire EDM. Due to the damage and recast layer induced by the wire EDM, foils were cut to be about 100 μm thicker than the final desired thickness to ensure that these damaged zones could be removed. These foils were then polished on both sides using SiC polishing papers starting

with 600 grit and working to 1200 grit for a near-mirror finish. This process was used both to precisely achieve the correct foil thickness as well as remove defects from the foils surfaces that would eventually be the top and bottom surfaces of the test samples. Additionally, these surfaces were imaged to measure strain in the sample using digital image correlation (DIC), so a surface with minimal defects was required. Figure 3-1 shows one such foil at different steps in the preparation process from starting with a bulk of René 88DT to achieving a polished foil ready to machine samples from. Once a foil of the correct thickness was achieved, microtensile samples were machined from it using one of the three techniques. For samples with thicknesses and widths of about 20 μm, FIB machining was performed as the final machining tool, whereas for samples with thicknesses and widths of 200 μm or larger, wire EDM machining was utilized and for samples with thicknesses and widths of 50-100 μm, femtosecond laser machining was employed.

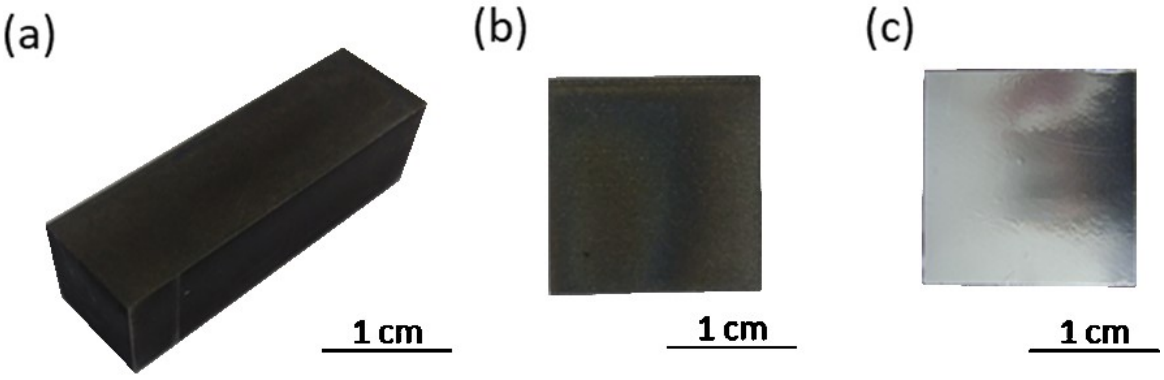

Figure 3-1: Images of (a) Bulk bar of René 88DT, (b) unpolished slice of René 88DT with thickness of 600 μm cut from bar using wire EDM and (c) foil polished to thickness of 500 μm and mirror finish.

3.3 Focused Ion Beam Machining

The focused ion beam (FIB) has become a widely used tool in microscale sample fabrication due to its very precise machining capabilities. Material ablation through the use of the FIB occurs by sputtering and focusing charged ions, typically Ga, on a target material. The interaction of these ions with atoms in the target material results in ablation at a relatively slow rate, but the nature of this process allows for delicate and precise machining and procedures, such as the extraction of TEM samples using FIB lift out. One of the first major applications of FIB machining for microscale test samples was its usage in milling micropillars for compression testing [11]. This methodology, which has inspired many subsequent microscale machining efforts, showed the viability of the FIB as a microscale machining tool and opened the opportunity for the precise machining of samples at the single digit micron scale. There has been concern with FIB induced damage in microscale samples due to Ga implantation and amorphization, which varies with material. While this effect is commonly observed, it has been suggested that it only plays a major role at the outer layer of the sample surface and with careful control of the beam size and current, can be limited to 100 nm or less [114]. While this level of damage will not play a significant role in microtensile samples with dimensions magnitudes larger than this, it is still important to be aware of in applying this machining technique.

Much of the ability to use the FIB as a machining technique for more complex geometries or three-dimensional samples such as micropillars relies on the ability to automate the machining process. One way in which this can be done is through the use of a fiducial marker and image processing to realign the sample for machining between each cut. For micropillars, a lathe milling process can be used and as the sample is rotated, it

can be properly realigned based on the fiducial marker. A similar process, which will be discussed later on in this section, can be used for machining more complex microtensile geometries even though most of the milling is done in a two-dimensional plane [31].

3.3.1 Optimization of FIB Machining

In terms of parameters that affect the quality of a FIB cut, two of the main ones are the current of the beam, which affects the material removal rate, and the focus of the beam, which affects the shape of the beam. For more of a bulk milling process a higher beam current can be used to increase the rate of material removal, and the focus and shape of the beam becomes less important [115]. Once a bulk milling process has been completed, a second finer milling process using a lower current and a more sharply focused beam can be used to achieve precision in the final geometry This two-step process provides the most efficient path to machining a microtensile sample from a foil of material.

One other technique that can lead to more efficient machining using the FIB is designing a machining path based on the shape of the beam. Even when the focus of the beam is corrected as much as possible, there is still a possibility of beam tails. These regions of the beam can be problematic not only because material can be removed in undesired regions which can cause damage or undesired taper, but the sputtering rate in this region can be higher or lower than the rest of the beam [116]. Although it seems like minimizing the tail would be the best method, it can actually be more effective to take advantage of the shape of the beam with the tail in order to simultaneously use a higher current and achieve faster milling rates without sacrificing machining quality. In addition, by calibrating the beam to have the tail occur only on one edge of the beam and having a

clean cut with the other edge, it is actually possible to have the beam cut even better than simply minimizing the effect of the tail for a symmetric beam. Most FIB systems, such as the Tescan Lyra system used in this work, have an automated process that can cycle through various settings for focus and stigmation at a desired beam current to rapidly provide an array of cuts to show the shape of the beam. From this array, it is easy to identify and select the parameters that are best suited for the machining process. Of course, when using only one edge of the beam, it is critical to maintain the orientation of that edge with respect to the edge of the sample. For this reason, not all cuts can be completed simultaneously, but rather the sample can be discretized into a series of straight cuts using the clean edge of the beam for each cut and rotating and positioning the sample using a reference to be properly oriented with the beam for each cut. In addition, tilting the sample slightly (~1 degrees) with respect to the beam can also minimize taper that arises due to the gaussian shape of the beam.

3.3.2 An Automated Process for FIB Machining of Microtensile Samples

A procedure for machining microtensile samples using the FIB was developed during an extended visit to the Air Force Research Lab, Materials and Manufacturing Directorate. This automated process used Python scripts to control a Tescan Lyra dual beam system for both imaging and milling. Starting with a thin foil of material, a circular fiducial marker was milled near the edge of the foil for each sample to be machined. These were used as a reference of where the sample grip section is located. Using image processing, the fiducial marker was identified and used to realign the beam as the sample is rotated to be cut. The geometry of the sample was discretized into a set of cutting steps with a corresponding rotation angle, position relative to the fiducial marker and beam size

for each cut that needs to be made. The sample stage was rotated to the appropriate angle, the image was centered on the fiducial mark and then subsequently moved to where the cut is to be made and the cutting process was performed. This procedure is repeated for each step of the sample geometry to complete one pass of the geometry. Each subsequent pass is performed to cut a geometry that approaches the final shape and uses less current to minimize damage in the final sample as less bulk material needs to be removed. The initial bulk passes are performed using a beam current of 3-5 nA, but for the final pass, current was reduced to 500 pA to minimize surface damage. Images of different steps of this machining process are shown in Figure 3-2 and 3-3. Figure 3-2 demonstrates a series of a few cuts at the beginning of one pass to carve out the sample geometry. Note how the sample is rotated to a new orientation before each cut. This procedure is repeated for multiple passes, bringing the cut geometry closer to the final sample geometry with each subsequent pass. Figure 3-3 shows images of the sample after 5 subsequent passes cutting with the FIB and bringing the cut geometry closer to the final geometry in addition to using a lower beam current with each pass.

Though some work is required by the user in order to program the cutting of the sample, it becomes an extremely reliable and repeatable automated process. This combination of using bulk and fine milling as well as optimizing the beam shape and taking advantage of the shape rather than working around it can be an effective and automatable method for some of the more complex geometries found in microtensile samples as compared to those in micropillar or microcantilever samples. The Python scripts used in this machining process can be found in Appendix A.

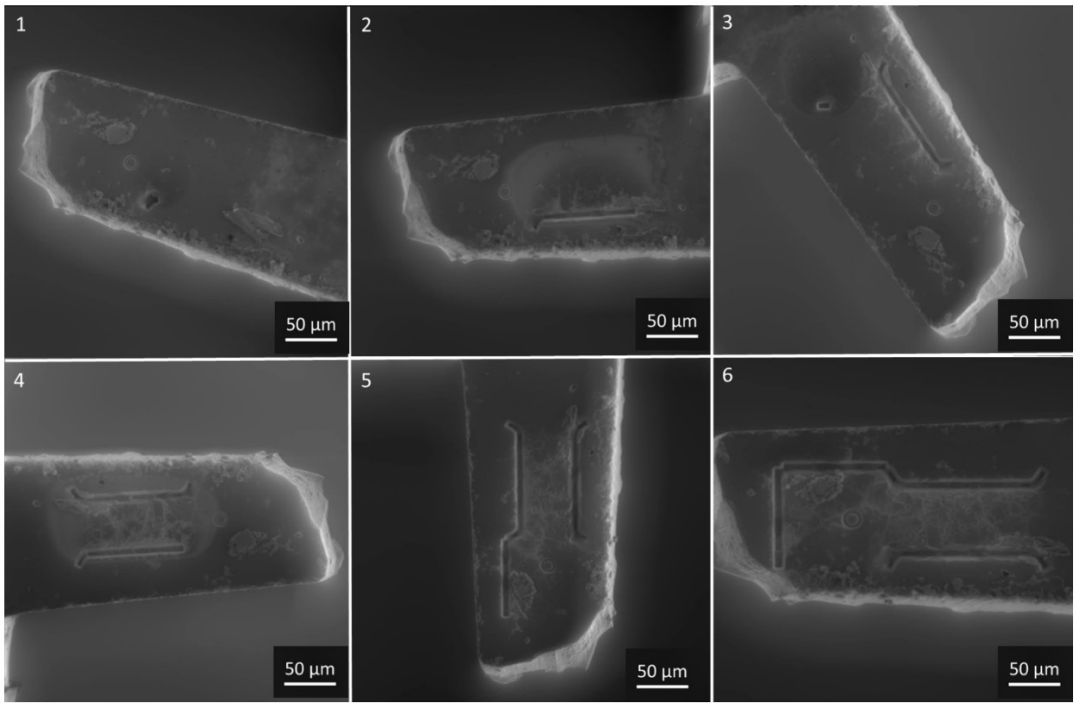

Figure 3-2: Images showing FIB microtensile sample cutting procedure. The sample is rotated to the correct angle, repositioned based on the circular fiducial marker and then the beam cuts the current segment as a horizontal box.

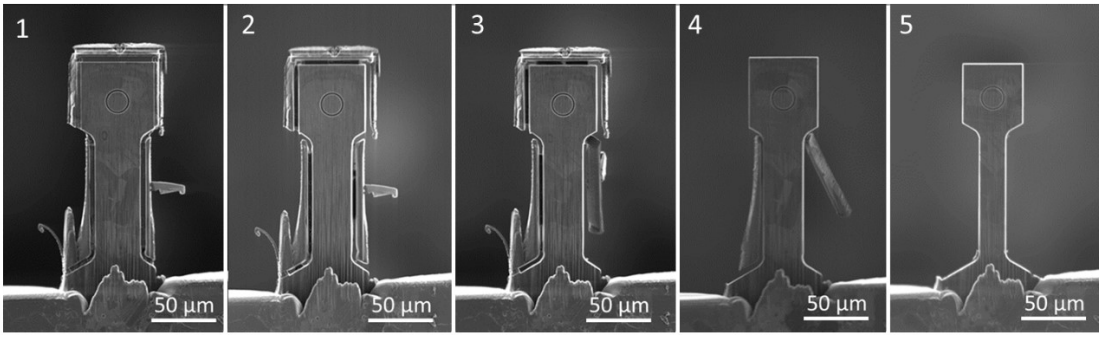

Figure 3-3: Progression of FIB milling procedure using 5 passes to reach final sample geometry. For each pass, the sample geometry is cut closer and closer to the final dimensions using a lower intensity beam

3.3.3 Discussion of FIB Machining

Despite the precision and widespread use of FIB milling, it is limited in some ways in terms of sample fabrication. One of the major limitations for using the FIB as a machining tool is the scale at which samples can be fabricated, which leads to the need

for the other machining processes that will be discussed. Slow material removal rates, typically on the order of 1 μm^3/nAs or less, that depend on the material that is being machined, can make it difficult to machine samples with dimensions larger than 50 μm in a reasonable amount of time [18, 114, 116, 117]. In addition, machining of larger samples also requires more care to be taken in the process of making a cut as machining across a longer distance makes is difficult to maintain the focus of the beam, which can lead to taper or an effect known as curtaining, and result in uneven material removal [118]. It is possible to shift the focus of the beam, but that would again require more time and effort with regards to repositioning the beam multiple times to make one cut.

Another drawback of using the FIB for sample fabrication is the difficulty in machining nonconductive samples. Due to the use of charged particles in both FIB and SEM imaging, it can be very difficult to image samples that are not conductive. Charging makes it difficult to do precise machining and utilize image processing for automated processes. Another aspect that makes working with the FIB difficult, especially with very sensitive samples is that imaging a sample with the FIB can cause ion irradiation damage at the sample surface and can continue to ablate material if the current is too high while imaging. For this reason, most FIB systems are also combined with an SEM for imaging to prevent this damage. However, this becomes a challenge when trying to automate machining using a fiducial marker because the fiducial mark usually needs to be in the plane of the machining path of the FIB, such as the fiducial mark on the grip head of the René 88DT microtensile samples. Imaging with the electron column is possible to view the fiducial mark at an angle, but it can be more difficult in term of image recognition as compared to imaging the fiducial mark head on using the FIB. If using the FIB, capturing

a single quick image rather than imaging continuously is optimal as long as the imaging conditions can be maintained throughout the machining process without damaging the sample.

3.4 Wire EDM Machining

A machining technique that is more commonly used for macroscale component fabrication but can also be applied at the microscale is Wire Electric Discharge Machining (EDM). Wire EDM, uses a wire in tension as the electrode. The sample and wire are submerged in a dielectric fluid, usually deionized water. The wire is guided along a programmed path for the shape to be cut out and as it approaches the sample, the distance between the two becomes small enough and the voltage great enough that the dielectric breaks down and allows discharge of electricity between the wire and the sample. The electric discharge locally heats the sample and the dielectric becomes a plasma. The material at the edge of the sample is heated above its melting point and the ejected material is removed once being cooled in the dielectric. This discharge process repeats rapidly and the material near the wire is removed and a cut forms along the path of the wire. A flushing flow of water cools the wire and removes the particles produced [119, 120].

Due to the nature of the wire EDM, there are some limits to the level of quality that can be achieved in sample machining, however there are multiple ways to optimize the quality of samples. The typical machining process can cause significant surface roughness and damage in the form of a recast layer because of the melting and vaporization of material that occurs. The main parameters that can be adjusted for the

machine are the cutting speed as well as the power and water flow. The Wire EDM system used in this study was Fanuc Robocut. In initial setup, the user selects a material as well as a thickness being cut, and the machine provides suggested parameters for machining. Although these parameters cut the material well at the macroscale, very rarely will the surface quality be suitable for a microtensile sample. In some cases, if the foil of material being machined is thin enough, the machine may not be able to recommend a setting at all or will give an incorrect setting in error.

3.4.1 Optimization of Wire EDM Machining

As with the other machining techniques described in this chapter, the most efficient way to use the Wire EDM for microscale machining is to perform the cutting process in multiple steps, first using a pass with higher power for more rapid material removal and then a subsequent pass using optimized parameters with lower power for a finer cut with less surface roughness and damage. Rather than relying on settings provided by the machine, the user can manually adjust the parameters which is necessary when trying to use wire EDM for such small samples. The rough pass can be done using parameters close to what is provided by the machine itself, but for the fine passes the power and speed must be lowered in order to achieve an acceptable level of surface roughness and damage. It was typically found that the parameters used for the finer cut were not able to cut through bulk material without the wire breaking, indicating the minimal amount of material removal and damage to the sample. It is also important in EDM machining of microsamples to maintain speed when cutting fillet radii or corners. Typically, the machine will slow down when machining these features, however, this option can be removed either directly in the machine or in the CNC Gcode being used.

Due to the small amount of material that needs to be removed, having a longer dwell time in these features in microscale samples can actually remove more material than desired, resulting in a stress concentration. Figure 3-4 shows an SEM image of a wire EDM machined dogbone sample along with magnified images of the surface roughness achieved with machine suggested and optimized wire EDM process and parameters and the parameters used for the rough and fine cuts of the optimized process are listed in Table 3-1.

Table 3-1: List of Wire EDM parameters used in optimized wire EDM machining process

	Optimized Rough Cut	Optimized Fine Cut
On time	6	50
Off time	28.0	20.0
Servo v.	20	80
Tension	1300	1700
Wire Feed	10	10
Water Flow	15	7
Water cnt.	0	0
Cutting spd.	0.472	0.240
Offset (in)	0.00620	0.00318

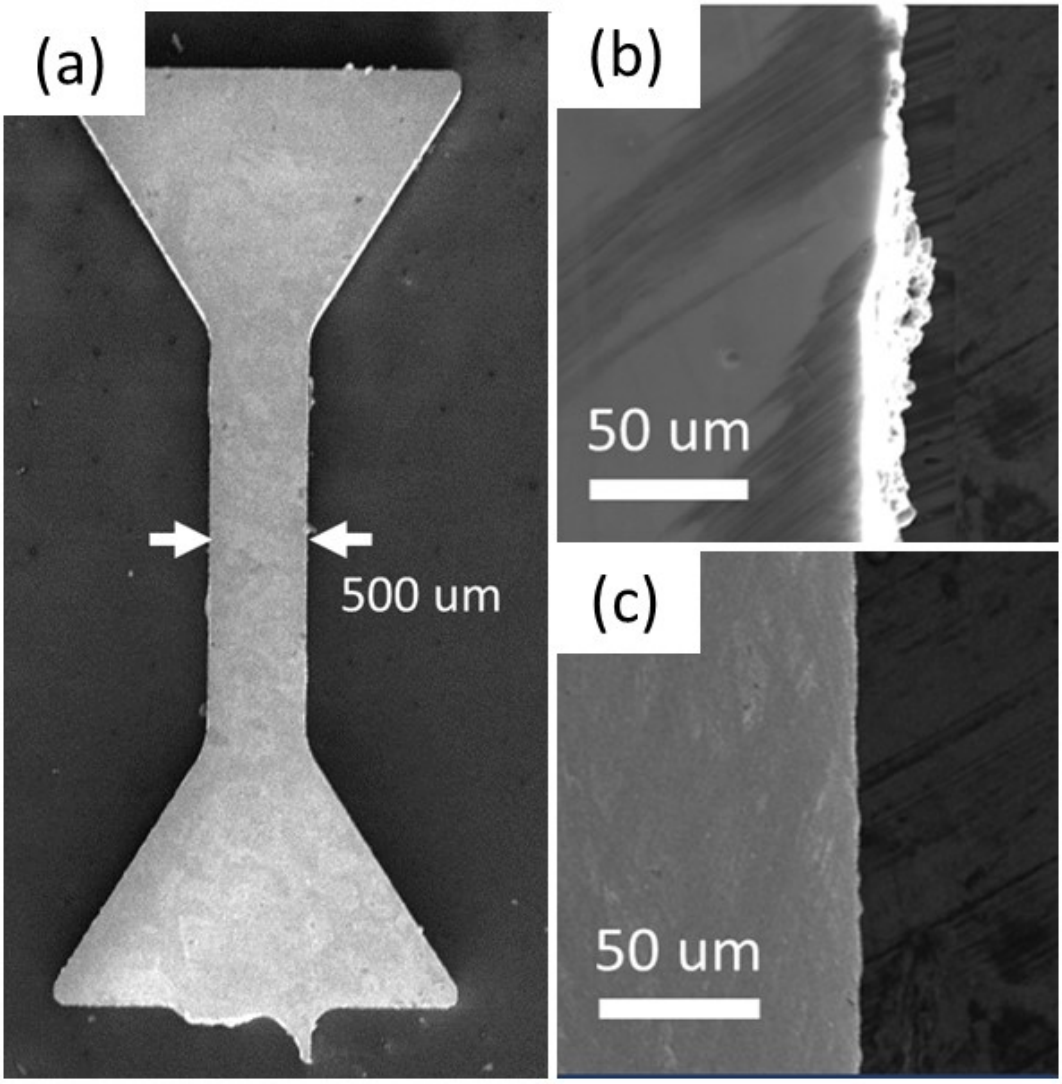

Figure 3-4: (a) Image of wire EDM machined René 88 microsample with gage dimensions of 500 um x 500 um. (b) shows the surface roughness of a sample cut using machine prescribed parameters and (c) shows the surface roughness using our optimized parameters

Figure 3-5 presents surface profiles captured using laser confocal microscopy of these two samples as well as a surface profile from a laser machined surface for reference. The improvement in quality of using a multiple pass methodology for machining microtensile samples as compared to prescribed machining parameters for wire EDM and using a single cut reduces the average surface roughness from 22 μm to 2 μm [119, 121-124]. In the laser machined sample, the surface roughness is less than 1 μm.

3.4.2 Discussion of Wire EDM Machining

As a machine typically used for larger parts, there are some drawbacks to the wire EDM as a tool for manufacturing microtensile samples. As mentioned before, samples have to be conductive in order to be able to pass a current to melt the material. As with the FIB, there is a limit to the scale of microtensile samples that can be machined using wire EDM, although in this case, it becomes difficult to cut samples below a certain size rather than trying to scale the technique up to a larger size. The limitation of sample size comes from two main factors: the tension of the wire on the sample during the cutting process and the surface roughness that can be achieved. In order for the wire EDM to cut, contact of the wire with the sample must be maintained during machining, and the wire must be kept tight in tension and a flow of water must also be maintained. For smaller, thinner samples or more delicate materials, this can lead to the sample being bent during the machining process. One means of mitigating this is fixing the sample to a rigid substrate using a conductive epoxy. In doing so, the sample can be protected from bending while still maintaining conductivity. However, there can still be challenges in using this technique as air gaps in the epoxy or between the epoxy and sample can still cause a short to occur which will prevent the wire from cutting. Using a thicker, more

rigid substrate will also typically require more power in order to cut through both materials which will limit the quality of the actual sample. In addition, if the sample has to be sandwiched in between two plates to fully protect it, it can be difficult to align the sample prior to machining.

The previously demonstrated surface roughness also poses a challenge when machining microtensile samples as this roughness will have more and more of an effect on the results of a mechanical test as the sample size decreases, as will be demonstrated in a later section. Rather than measuring the actual desired material response, the roughness can cause artifacts in the experimental data due to premature failure at a surface flaw or creating stress concentrations in the sample geometry. Depending on the material, the limit of the samples that can be created using Wire EDM is only a few hundred microns, as long as the roughness can be optimized, and the sample can be protected from being bent by the wire tension. In this work specifically, the smallest dogbone microtensile samples that were machined had a gage width and thickness of 200 μm. In addition to the wire EDM system utilized in this thesis, there are also specialized systems for machining at the microscale with a smaller wire known as microEDM. Though this smaller wire allows for holes and fillets with a tighter tolerance to be produced, the same optimization of cutting parameters must be applied in order to minimize surface damage [120].

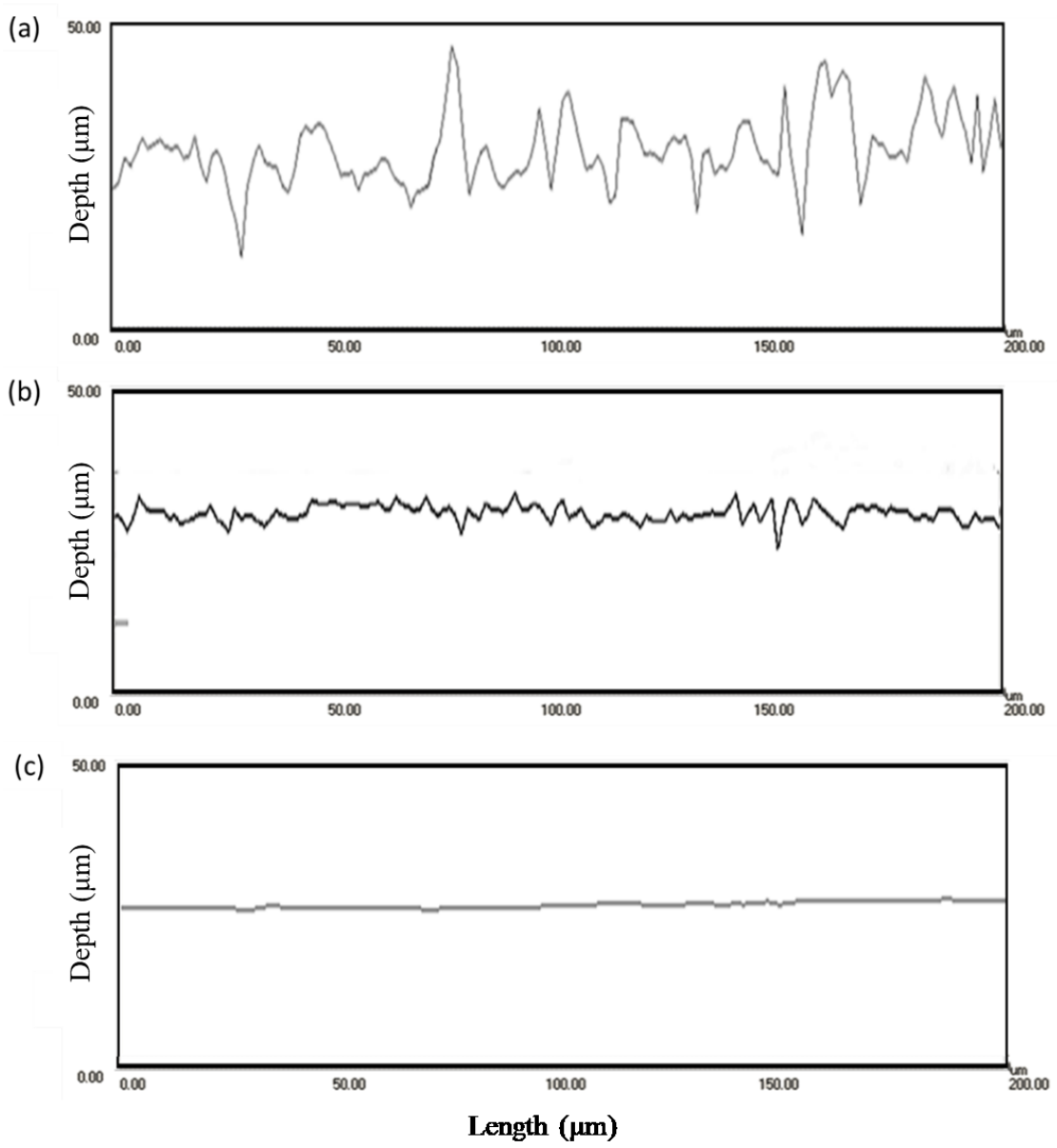

Figure 3-5: Surface roughness profiles obtained with confocal laser microscopy for: (a) EDM machined surface with machine recommended parameters (b) EDM machined surface with optimized parameters and (c) femtosecond laser machined surface

3.5 Femtosecond Laser Machining

Where the FIB is a valuable tool for machining microtensile samples at the lower length scale on the order of less than 50 μm and the Wire EDM has been shown to be a capable tool for machining microtensile samples of a few hundred microns up to the macroscale, there exists an intermediate length scale that neither technique is effective. One tool that has shown potential for machining samples at this length scale, however, is the femtosecond laser. The use of femtosecond laser for microscale sample fabrication is proving to be one of the more effective methods for both precise machining at material removal rates orders of magnitude greater than FIB machining [58, 125-128]. As well, compared to nanosecond and picosecond lasers, femtosecond lasers have been shown to create less damage and develop virtually no heat affected zone in the material being machined [129]. The use of femtosecond lasers for various material removal processes has been demonstrated already by multiple groups for both sample preparation and materials characterization [4, 57, 58, 126, 130, 131].

3.5.1 Description of JHU Femtosecond Laser Machining Setup

A femtosecond laser-based machining setup has been developed, as part of this thesis, in order to fabricate microscale samples. The main component in the setup is a Clark-MXR CPA femtosecond laser which outputs the laser beam that will be eventually used for ablation of the target material. The maximum output of the laser is 1W, but the actual power used in machining is 0.1 W or less and can be controlled from the main laser system console. The laser beam is directed into a custom built safety enclosure, where the laser optics and machining components reside. The laser beamline first passes through a waveplate polarizer which allows for more precise attenuation of the beam as well as the ability to automate the attenuation process. A software interface on the system

computer allows for precise rotation of the waveplate to carefully control the laser energy. The beam is then directed within the containment using a series of laser steering mirrors that reflect it to a final dichroic mirror. The dichroic mirror reflects the beam downward to a 10x Mitutoyo NIR Objective lens, which focuses the beam to a spot size of about 30 μm for microscale machining. Figures 3-6 and 3-7 demonstrate the optical components used from attenuation of laser power and beam steering as well as the optical setup of the camera and dichroic mirror for imaging.

The laser beam having a wavelength of 780 nm allows it to be reflected by the dichroic mirror, while visible light still passes through the mirror, allowing for imaging of the sample using the camera. This makes alignment and positioning of the beam at the beginning of a machining process much easier as long as the vertical offset between the focal plane of the camera and the focal plane of the laser beam are known. In the case of this setup the offset it typically 2.7 ± 0.15 mm. In addition to the various optical components of the setup, there is also a set of Aerotech brand stages that allows for motion on three axes. The objective lens is mounted to the stage which controls the motion in the vertical (Z) direction. The main purpose of this stage is to control the focus of the camera during imaging and the laser during machining. Once the initial height of the objective lens has been established, most stage motion occurs through the two axis X-Y stage. The sample sits on this dual axis stage during machining and the path that the stage travels is programmed using an Aerobasic script in the stage controller software. The laser beam remains focused in the same spot during machining while the sample is moved in the desired shape to be machined rather than having the beam move on the sample to perform the machining. The reason for this process is that the beam will cut the

same way every time since it is stationary, resulting in a much more consistent machining procedure.

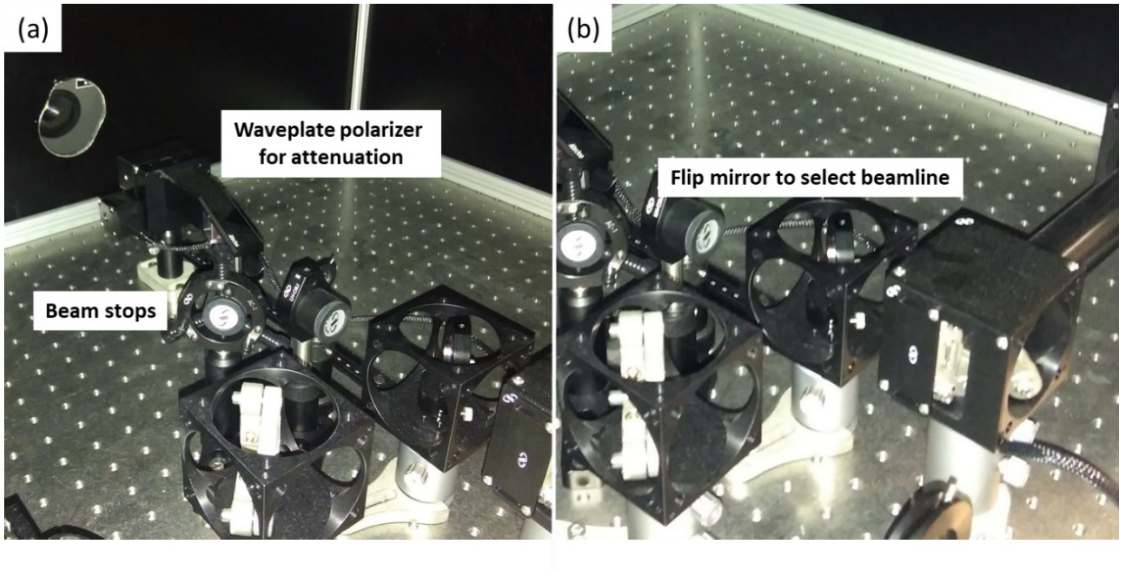

Figure 3-6: (a) Image of beam ejection site from laser and equipment for beam attenuation and (b) optics for switching between laser machining and SEM-based In-situ serial sectioning setups.

As with any laser system, safety is an important consideration, especially in this case as the 780 nm wavelength of the laser beam is in the invisible light spectrum. One main precaution that is taken during operation is that laser safety eyewear is worn by the operator and those in the nominal hazard zone (NHZ) at all times, as well as by others in the lab when the laser interlocks are engaged. A set of safety interlocks has been installed on the doors to the lab and they will trip and close the laser shutter when the doors are opened. The laser safety containment box must also remain closed while laser machining is occurring.

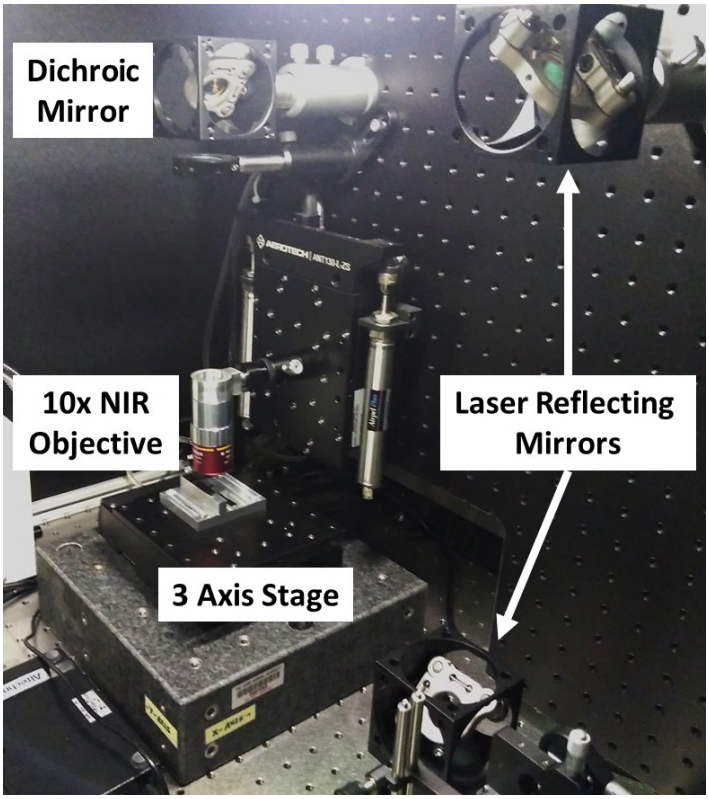

Figure 3-7: Image of 3 axis stage system and laser machining optics.

3.5.2 Optimization of Laser Machining Process

As with the other microtensile machining tools described in this chapter, there are many techniques to be used with femtosecond laser machining to improve sample quality as well as parameters that can be adjusted accordingly. Once the spot size of the beam has been properly focused, the main parameters than can be changed in the laser machining setup are the energy of the laser and the speed at which the stage moves. The laser energy is a critical aspect to material removal because of the ablation threshold that must be reached for vaporization of each material [132-135]. Increasing the energy of the beam will result in a higher rate of material removal and a larger effective spot size of the beam because more of the beam at the edges of its gaussian profile will be above the

ablation threshold. However, increasing the energy will also impose more damage in the sample. Care must be taken to select a correct energy that is above the ablation threshold of the material but isn't high enough to cause significant damage in the subsurface layer of the material [135-138]. The stage speed and number of passes can also be varied to affect the effective number of laser pulses that hit the sample during machining. A slower speed with fewer passes can remove more total material from the sample, but a higher speed with more passes can provide a higher quality sample because less redeposited material builds up on the sample as seen in Figure 3-8 and there is less chance of developing a heat affected zone by overlapping pulses.

Another challenge of femtosecond laser machining that mirrors what is seen when machining with the FIB is taper in machined sample edges. There are a few techniques that can be used, however, in order to minimize the effect of taper. One technique is to use a two-step process as has been described for FIB and wire EDM machining. An outer series of passes of the sample geometry at higher energy is first used in order to remove most of the material to be cut away. Then, a series of subsequent passes with less energy can be used in a trepanning method in order to achieve the final sample geometry. A diagram showing this trepanning method is shown in Figure 3-9 and an array of high quality microtensile samples of René 88DT machined using this technique are shown in Figure 3-10. Each sample was cut using 60 total passes with a beam energy of 50 μJ. Every 10 passes for the first 30 passes, the beam was moved 5 μm closer to the final sample geometry as depicted in Figure 3-9. The first 30 passes were performed using a stage speed of 0.5 mm/s and the final 30 passes were performed at a faster speed of 2.0 mm/s.

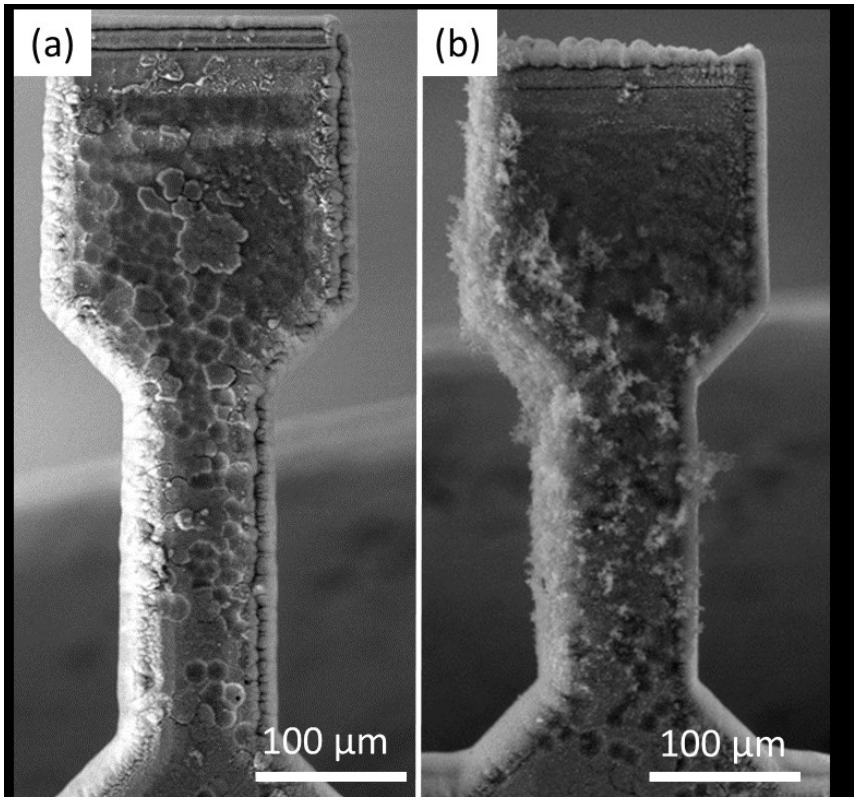

Figure 3-8: Images demonstrating redeposited material (a) on top the surface of a sample and (b) on the side surface of a sample, that can occur if redeposition is not properly removed or controlled.

Not only does this methodology provide less damage in the final sample, but the taper is reduced due to less of the beam spot size area being above the ablation threshold of the material. Another method that can be used to minimize taper is based on the idea of tilting the sample during FIB machining to minimize taper. In this case, the objective lens that focuses the laser beam can be tilted slightly in order to obtain a similar effect. The objective lens is mounted on a rotator that can be manually adjusted to tilt the objective lens by about 1 degree, allowing the edge of the beam to cut parallel to the sample edge, rather than at the tapered angle. The one drawback of this technique is that like the tilting done in FIB machining, only one cut can be done at a time rather than machining the

entire sample geometry. An image of a microtensile sample machined using femtosecond laser and a magnified view of the transition region is shown in Figure 3-11 to give some better perspective of the quality of sample than can be achieved with this technique.

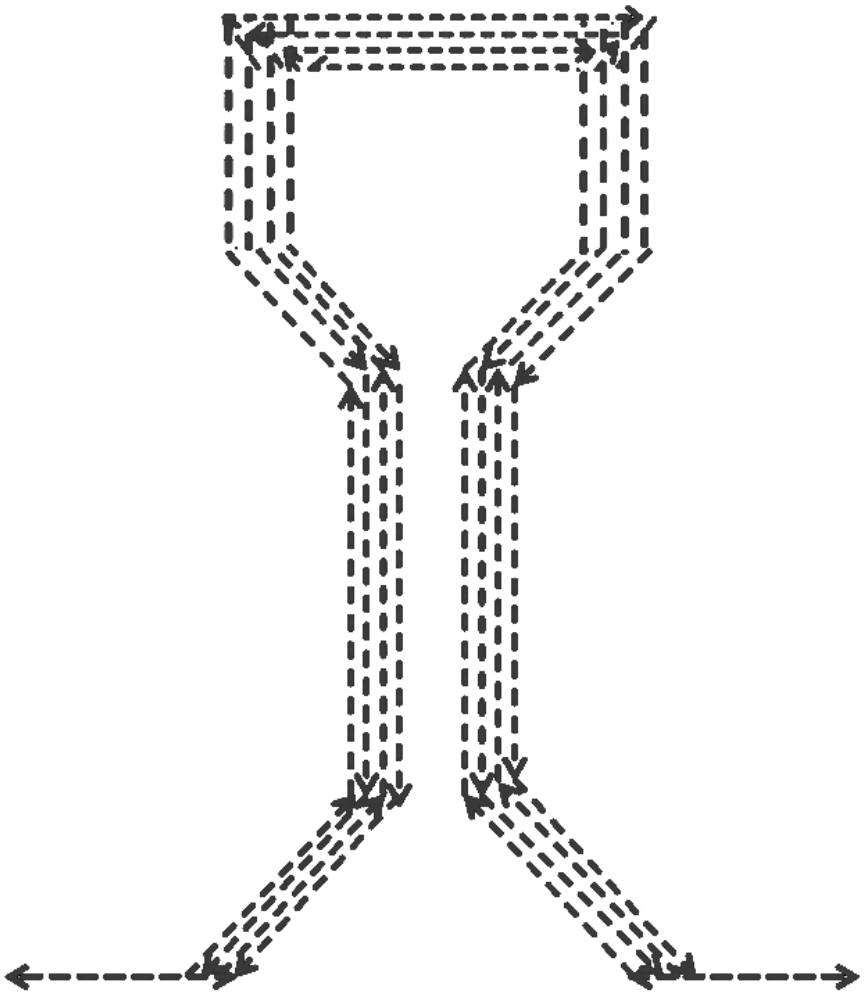

Figure 3-9: Schematic of laser machining path for microtensile sample demonstrating trepanning method. Similar to the method presented with the FIB, the sample geometry is cut closer to the final geometry with each pass. For this final shaping of the sample the laser energy remains the same for each pass and is on the order of 20 μJ for machining René 88DT.

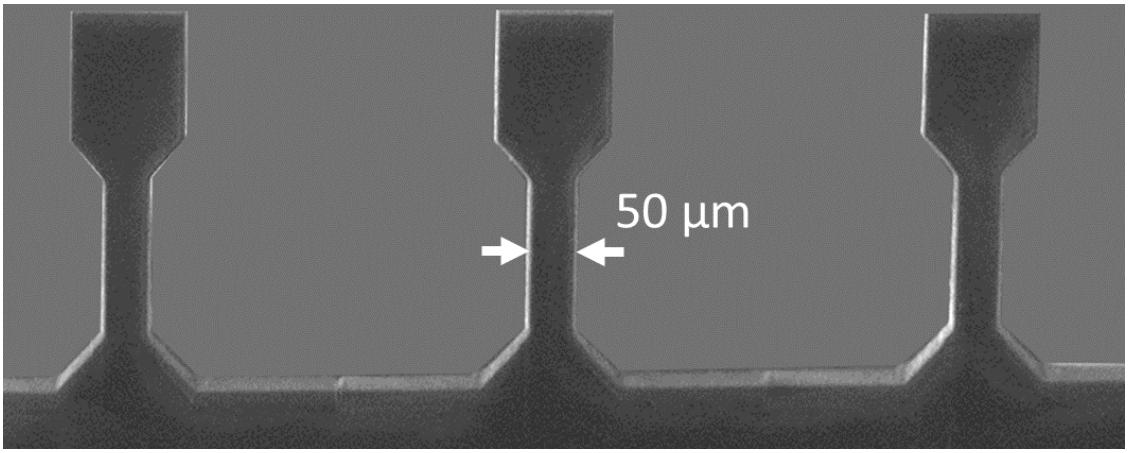

Figure 3-10: SEM Image of array of microtensile samples rapidly manufactured using femtosecond laser ablation.

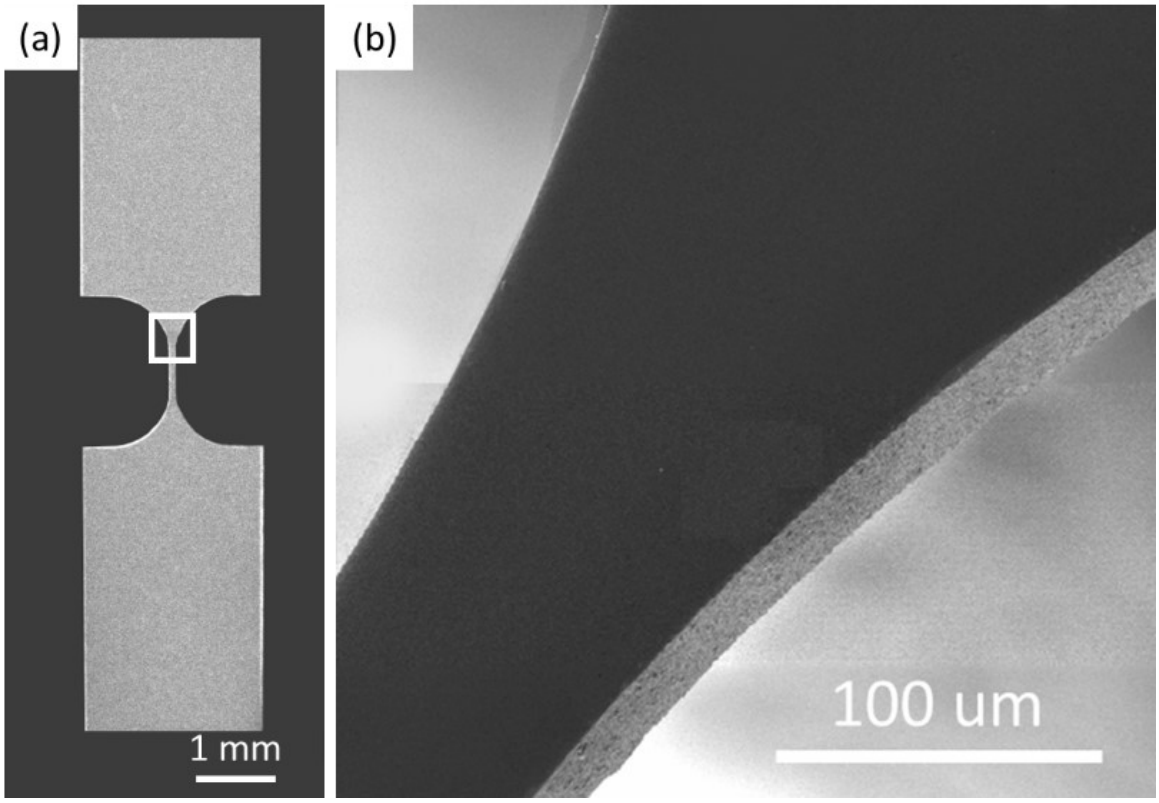

Figure 3-11: (a) Image of laser machined microtensile sample and (b) magnified view of gage to grip transition of boxed region of sample in (a).

3.5.3 Discussion of Femtosecond Laser Machining

As a promising technique in sample fabrication, there are numerous benefits to the use of laser machining and femtosecond laser machining in particular. The main reason the technique is so promising is that the scale and precision at which samples can be manufactured is close to that of what can be manufactured with the FIB in terms of the level of damage, but at orders of magnitude faster. This low level of damage and surface roughness, as seen in Figure 3-5, is the key to making the femtosecond laser a viable technique for machining samples at the microscale. As described previously, the use of femtosecond laser compared to picosecond or nanosecond lasers provide significantly different results in terms of their machining quality because of the level of melted material and redeposition. Although the ablation of material through the use of femtosecond laser is difficult to capture experimentally, MD simulations of the process provide insight into how a low level of damage can be obtained by minimizing the heat affected zone [129]. Material is vaporized more rapidly than heat can be stored in the material due to the extremely short laser pulse durations. Another benefit to the use of femtosecond laser machining is that the system that has been developed is setup in open air in a laboratory setting, whereas the FIB requires a vacuum chamber and SEM for imaging. In addition, unlike the previous techniques described in this paper, the use of femtosecond laser can more easily be applied to a broad selection of materials, not just conductive materials [89]. Due to the nature of the technique, there is no need for an electrical circuit to be established, as long an appropriate beam energy can be selected based on the ablation threshold of material, the technique is material agnostic.

However, the use of femtosecond laser machining is still being developed and there are some drawbacks. One of the most difficult things to control is the redeposition of material that accompanies ablation. A plume of material is released from the sample and tends to redeposit back on the sample or on surrounding surfaces. This can result in redeposited material collecting on other samples that are being machined if there is an array of samples or material redepositing on laser machining optics such as the focusing objective lens in particular. The redeposition can be managed during machining by blowing air over the sample, but for fragile materials or sample geometries, this can be dangerous to do. Typically, the redeposited material will have to be cleaned off after machining. Using a procedure of more passes of the sample geometry with a higher speed generates less redeposited material.

Being in an open-air laboratory setting, environmental effects can also have a nontrivial effect on the machining ability of the setup. Fluctuations in temperature and humidity can affect the positioning of optics both internal and external to the laser to a point that renders the machining setup unusable without recalibration. For this reason, the laser must be maintained within a stable climate to guarantee consistent use. Imaging during machining can be difficult because of the offset between the focal planes of the camera and laser in the setup. A second camera and objective could be implemented to observe machining of the sample from the side or at an angle, but it wouldn't provide the best view of the machining process. Finally, as with the FIB, there is a limit to the size of sample that can be machined well using the femtosecond laser. Though ablation rates are significantly higher than with the FIB, there is still a limit at which milling becomes inefficient. Milling trenches past a certain depth becomes more and more difficult

because there is less potential for redeposited material to escape and because of the depth of field of the objective lens. The femtosecond laser as a microtensile sample machining tool shows a lot of promise at a length scale for samples with thickness between 10-300 um, depending on the material being machined. It shows great promise for its ability to machine samples quickly and precisely at a length scale that inhibits other machining techniques and for many classes of materials.

3.6 Comparison of Machining Techniques

FIB machining is viable for microtensile samples on the order of tens of microns, laser machining appears viable for machining of samples on the order of tens to a few hundred of microns and wire EDM is a viable technique for any samples larger than that. However, there is some overlap between techniques regarding the scale at which they can be used. In order to better assess how well each technique could perform relative to the others, samples of René 88DT machined using each of the techniques were compared. SEM images of the edges of three samples, one machined with FIB, one with fs laser and one with optimized wire EDM are shown in Figure 3-12.

As is shown in Figure 3-5, the average surface roughness for each of the three techniques in this case is less than 1 μm for the femtosecond laser, 2 μm for optimized wire EDM cutting and 20 μm for the machine suggested wire EDM parameters. Though the surface roughness of the laser appears to be minimal, there is a machining artifact that develops the at the ablated edge of the sample known as Laser Induced Periodic Surface Structures (LIPSS) [139, 140]. The formation of LIPSS is important to note in terms of laser machining and the scale at which it can be used. These structures, though relatively low, prevents the technique from being used for applications such as lift out of a TEM

foil via FIB machining. The appearance of LIPSS in the material cannot be avoided, but it is possible to affect the orientation of LIPSS based on the polarization of the laser. The roughness of these structures is on the order of about 100 nm, so for the size of sample being machined in this study it will not impact the mechanical response.

An estimation of the effect of surface roughness on the sample strength can be determined by modeling the roughness as a stress concentration in the geometry at the sample surface. Suh et al. developed a model using the finite element method (FEM) in order to model the surface roughness in aluminum tensile bars and model its effect on the mechanical response of these tested samples [141]. They reported that experimentally the roughness of the technique that they used for sample machining increased, even with the same machining parameters, as the sample size decreased. They then used these roughness values to develop periodic boundary conditions in their FEM model. In the best case surface roughness they achieved in tested samples with thickness of 1.58 mm, the surface roughness of a few microns compares favorably with the surface roughness that we have been able to achieve with wire EDM. The results of both their experiments as well as their simulations suggested that this level of surface roughness has very little if any impact on the measured strength of the sample or it's mechanical behavior. Even when modeling the worst case of roughness for the samples, the FEM modeling suggested that a change in strength due to the surface roughness of the samples had a small effect and that any drop in strength is likely more closely related to size effects in the material rather than manufacturing artifacts [141].

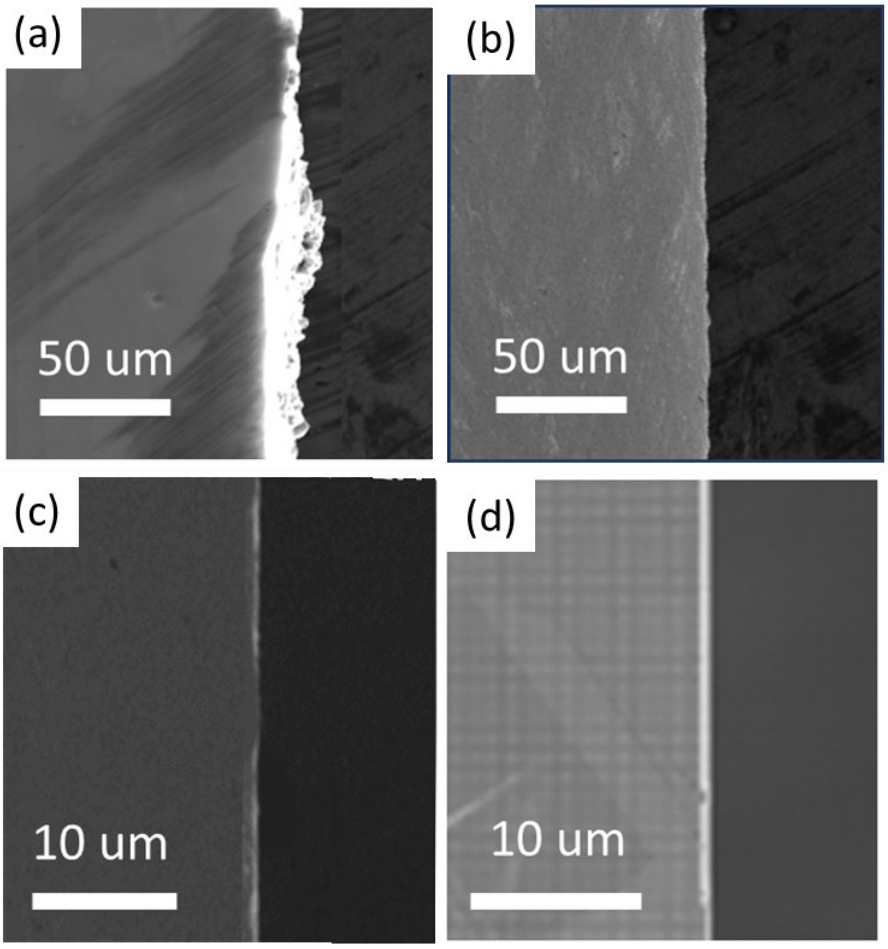

Figure 3-12: SEM images showing surface roughness of microsamples prepared by: (a) EDM with machine prescribed parameters, (b) EDM with optimized parameters, (c) fs laser machining, (d) FIB.

In order to measure the impact that sample roughness had on mechanical response in the current study, samples were cut using the suggested wire EDM parameter samples with a surface roughness of 20 μm and compared to the optimized wire EDM samples with surface roughness of 2 μm. Two sets of studies were conducted to compare the effect of surface roughness on the measured mechanical response of microtensile samples. In the first study, the roughness of the suggest EDM machine parameters with a single pass cut was compared with the roughness using optimized conditions for René

88DT. Microtensile samples were machined with nominal gage dimensions of 400 um x 400 um x 1600 um using the two different sets of parameters. Figure 3-13 shows a comparison of the stress-strain response of six samples, three from each batch of samples machined the two sets of parameters.

It's evident from the stress-strain response that the roughness in the suggested wire EDM parameters has a significant effect on the mechanical response of samples of this size. The mechanical response of the samples machined with the optimized EDM parameters is consistent across all samples tested, whereas the mechanical response of the samples with greater surface roughness shows significant scatter in the data. In addition, the average yield strength of the samples with optimized surface roughness is 1120 MPa, which matches well with the bulk response for René 88DT, whereas the average strength of samples machined with greater surface roughness was 980 MPa. And even the strongest sample only had a yield strength of 1070 MPa. It is necessary to ensure that behavior such as this resulting from machining artifacts in samples at this size scale is eliminated in order to prevent erroneous results in further experiments utilizing the same machining process. Moreover, when attempting to study the effects that microstructure has on sample properties, there must be certainty that the results are actually due to microstructural influences rather than sample machining defects, as will be discussed more in Chapter 4.

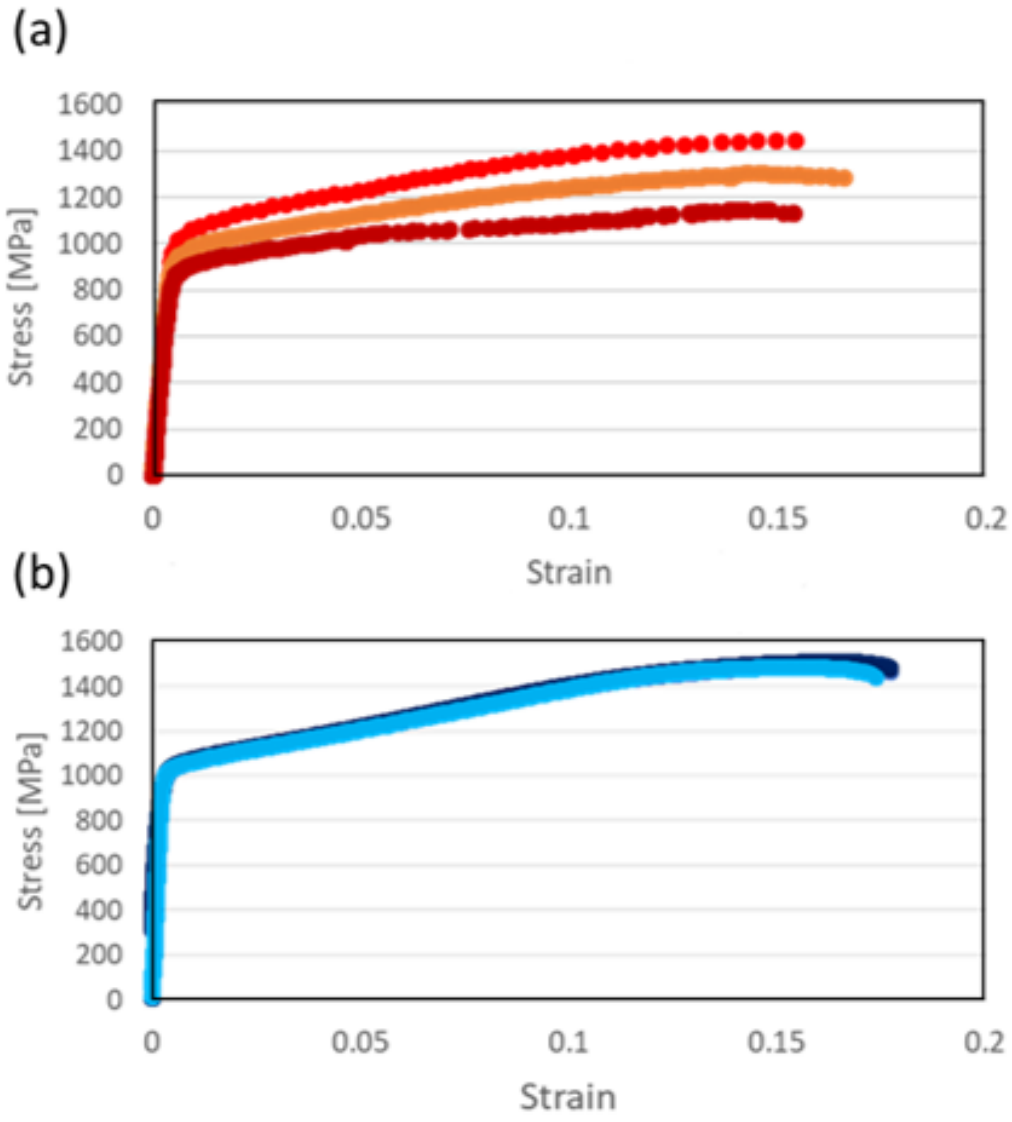

Figure 3-13: Comparison of mechanical response of microtensile samples with gage dimensions of 400 um x 400 um machined using (a) machine recommended EDM parameters and (b) optimized EDM parameters.

In a second case study, the effect of wire EDM surface roughness was compared with the effect of roughness from femtosecond laser machining. Samples of a NiMoW alloy [142, 143] were machined using each of these two tools with nominal sample gage dimensions of 20 µm x 400 µm x 1600 µm. Figure 3-14 shows images of the two sample

edges cut using wire EDM and femtosecond laser, and it shows the clear difference in magnitude of surface roughness between the two techniques.

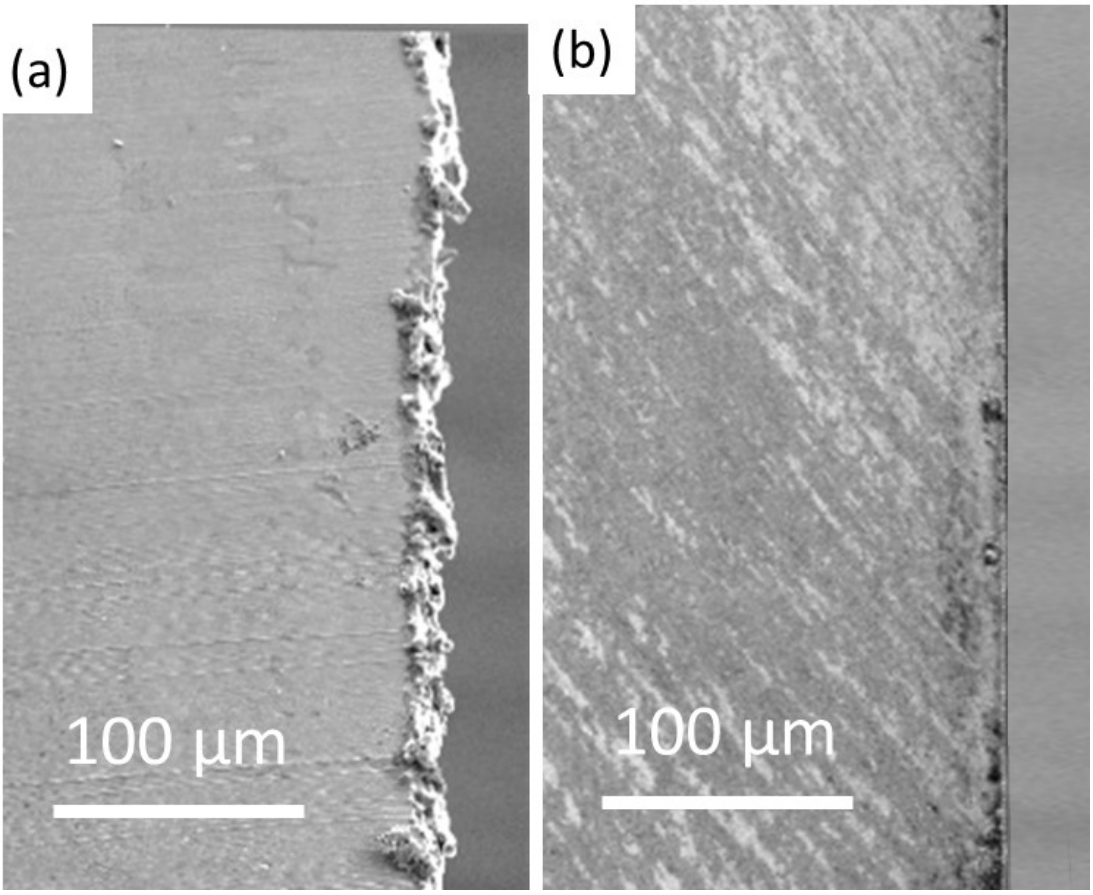

Figure 3-14: Images of 20 µm thick NiMoW microtensile sample edges machined using (a) wire EDM with optimized settings and (b) femtosecond laser.

Figure 3-15 shows a comparison of the stress-strain response between a laser machined NiMoW sample and one machined with EDM. Unlike in the previous study, the stress-strain response in both cases was much more consistent. However, the sample machined with the femtosecond laser showed an increase in ultimate strength from 3.3 to 3.5 GPa (5.8%) when compared to the wire EDM manufactured samples. There is also some plasticity seen in the fs laser machined samples, with an increase in strain to failure

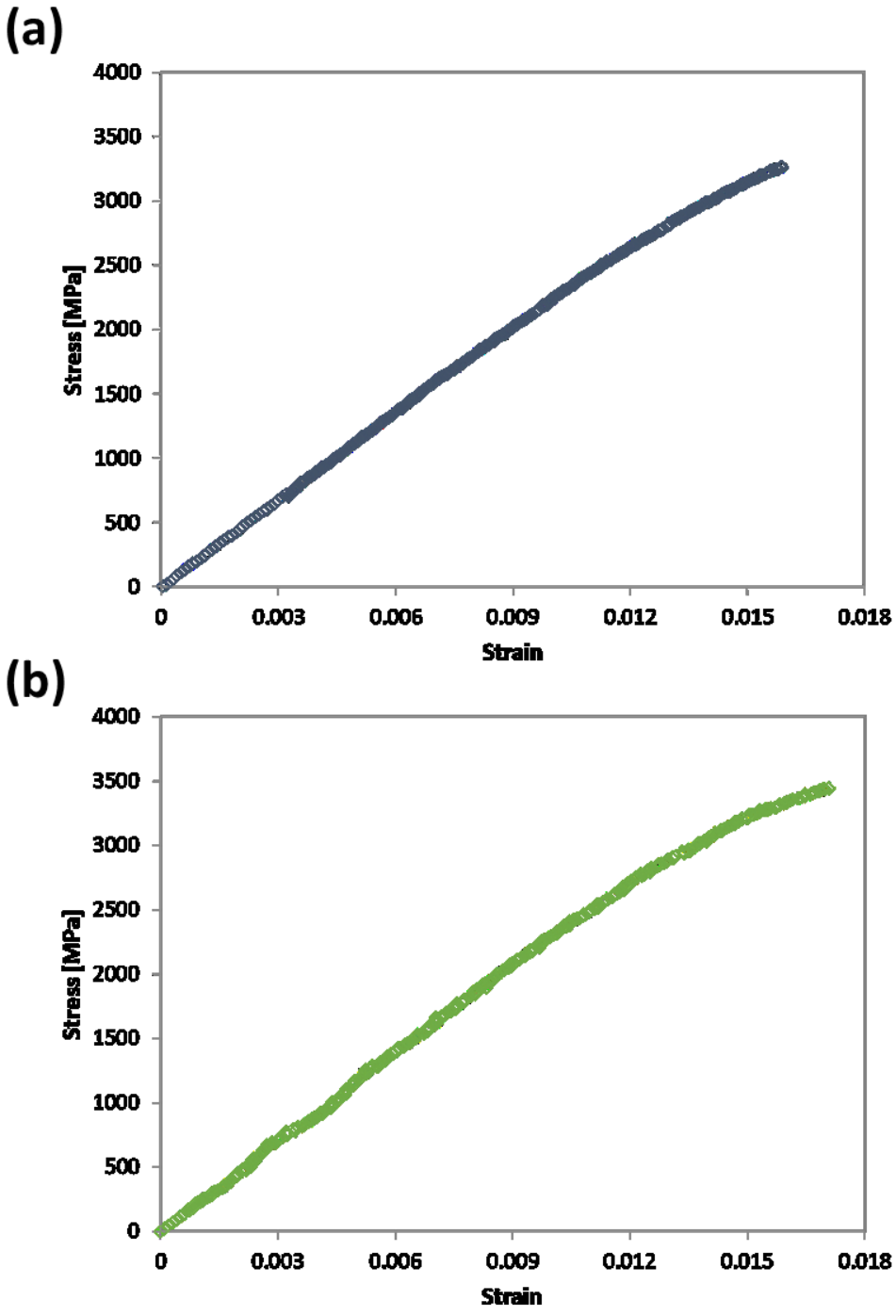

Figure 3-15: Plot comparing stress-strain response of (a) a NiMoW sample machined using wire EDM with (b) a sample machined using femtosecond laser. The laser machined samples showed increase in strength and ductility compared to the ones machined with wire EDM.

from 1.58% to 1.7%, that is not seen in the wire EDM machined samples due to premature failure of the sample from surface roughness. Although these are marginal improvements in the mechanical response and have only been seen in a small sample size, the improvement of sample quality is evident from Figure 3-14 and would play a more critical role for measuring mechanical properties in a smaller sample geometry of this material. In this case the wire EDM conditions were optimized for minimum surface roughness, the limitation of the technique can be seen in the case of sample dimensions, here the sample thickness, being at a length scale at which this level of EDM induced surface roughness is nontrivial with regards to its effect on the mechanical response.

Where understanding of these machining tools and techniques can be of significant use as well is in combining these techniques in order to develop the most efficient workflow possible for machining samples. It is clear that the scales at which these three techniques overlap with each other occurs between the FIB and femtosecond laser, and the femtosecond laser and wire EDM. Due to the fact that the material removal rates of these three techniques differ by orders of magnitude, implementing each of them at the appropriate scale in an overall machining workflow allows for a faster throughput in sample fabrication [18, 58, 93, 119]. As was demonstrated in 3.2, in order to excise microtensile samples starting from a bulk piece of material, the wire EDM is essential in order to cut foils from the material in a timely manner that can then be polished to an appropriate thickness to be cut using any of the three techniques discussed in this chapter. As long as enough material can be removed using subsequent polishing to remove any damage imparted by the wire EDM, this process can be extremely beneficial in terms of time reduction. One application of combining these machining techniques that seems to

be very promising is in using femtosecond laser for bulk milling of sample geometries followed by FIB machining of the final sample geometry.

Another application for this technique is in fabricating microbending fatigue samples, which requires removing a large amount of bulk material through the machining of bulk trenches before shaping the final beam geometry. Figure 3-16 shows an example of micropillars of single crystal Ni-base superalloy René N5 prepared by Lavenstein et al [39] that were fabricated using this process to demonstrate its viability. Figure 3-16a shows the bulk machining performed using femtosecond laser to cut a beam that will have a final gage width of 5 μm. This cut was performed using a laser energy of 100 μJ and took about 15 minutes to perform. Figure 3-16b shows the final sample geometry after FIB milling. In this case, by performing bulk milling using the femtosecond laser, the time required for FIB machining was cut from 12 hours to 5 hours, a dramatic time savings even though FIB machining is still required. This efficiency would not only save time and resources but would also allow for more thorough materials testing with more samples available in a shorter amount of time and the ability to create more robust and statistically relevant datasets.

This technique could also be applied to fabricate micropillars, which require significant bulk trench milling as well before cutting the final sample geometry. Figure 3-17 shows a schematic of how this two-step process could work in removing a large amount of material with laser machining in the first step. Figure 3-18 shows pillars of Mg with 50 μm diameter that have been bulk machined with femtosecond laser in a matter of about five minutes. Although this technique was not directly applied for machining micropillars of Mg as had been performed with microbending samples of René N5, the

expected time to machine a sample in using this technique for future applications is reduced from 90 minutes to 30.

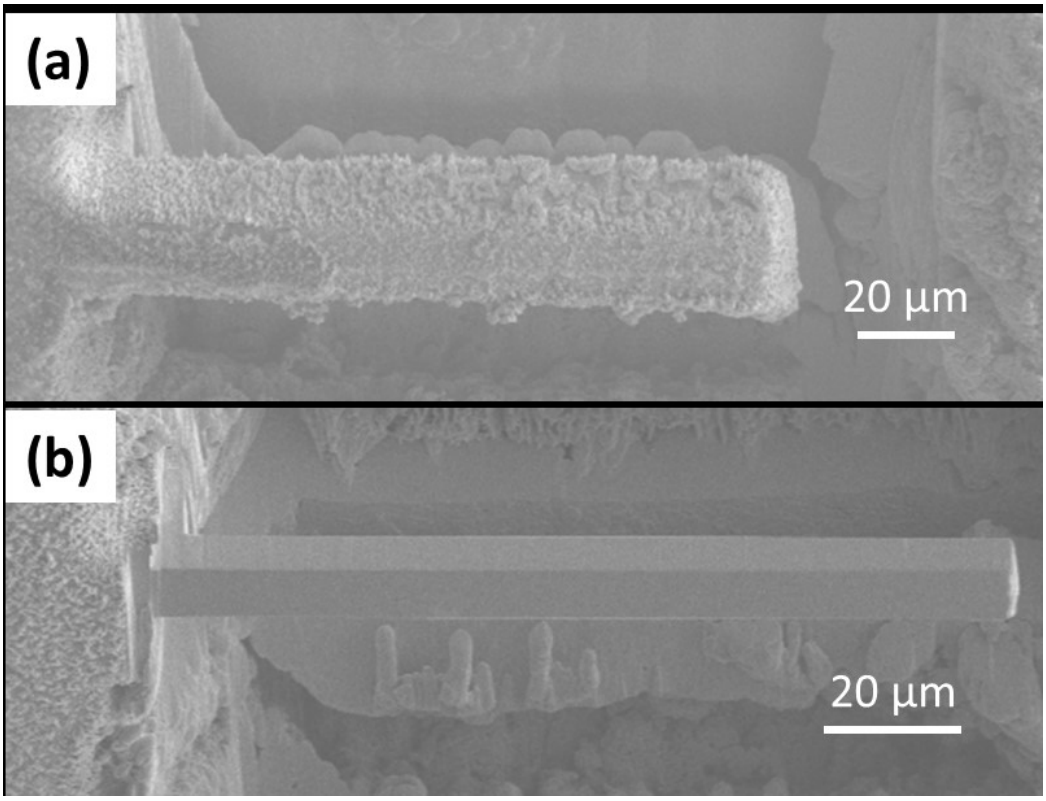

Figure 3-16: SEM images of (a) René N5 beam after bulk milling with femtosecond laser and (b) final beam shape after milling with FIB [39].

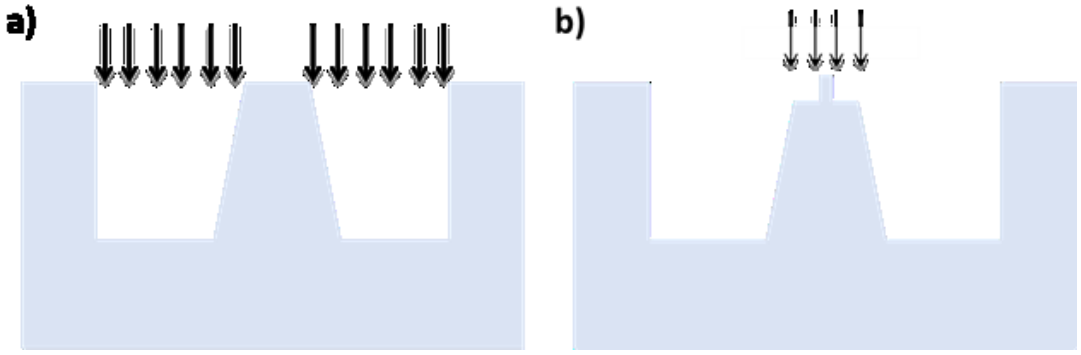

Figure 3-17: Schematic of 2 step micropillar milling process using (a) femtosecond laser milling for bulk machining followed by (b) FIB milling of the final pillar geometry.

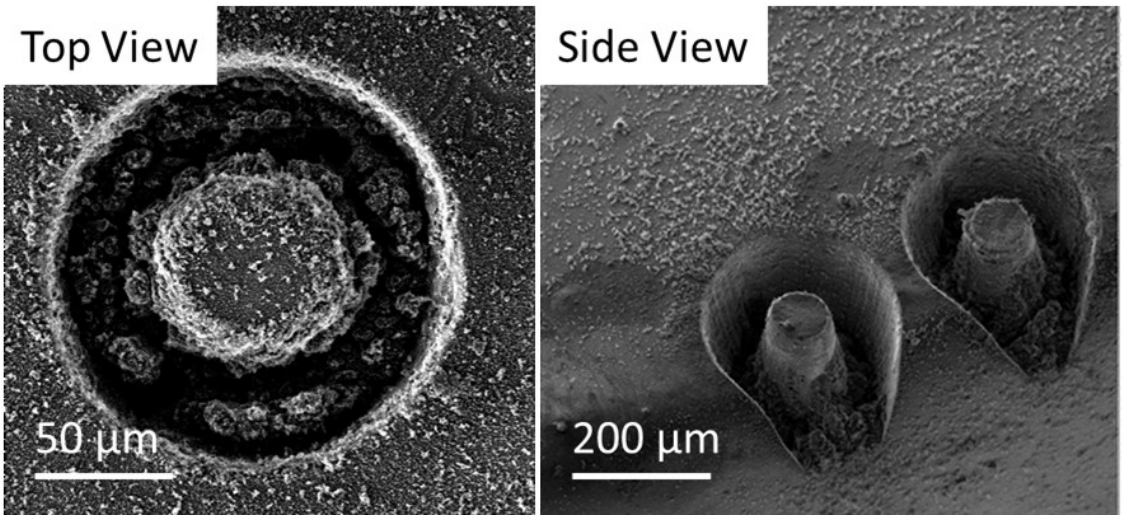

Figure 3-18: SEM images of Mg micropillars after bulk milling with femtosecond laser demonstrating bulk trench milling in initial micropillar sample fabrication

A similar procedure was also applied to machine microtensile samples of René 88DT, such as the ones shown in Figures 3-2 and 3-3, in order to minimize the amount of bulk material that had to be machined using the automated FIB machining procedure. An image of a bulk machined sample with the laser is shown in Figure 3-19a and the same sample subsequently machined using the automated FIB process previous described is shown in Figure 3-19b. Further discussion of these samples will take place in Chapters 4 and 5.

It is clear that each of these three machining techniques is relevant at a specific length scale in terms of the rate of material removal, as well as the level of damage that each imparts. The FIB has been demonstrated to be quite useful for machining sensitive materials or machining at length scales of tens of microns or less with high precision and very low damage. The femtosecond laser, though still a relatively new machining tool, has already been applied in enough cases to demonstrate its ideal usage at machining samples with a thickness ranging from tens of microns to a few hundred microns with

damage scaling with laser beam energy, but able to be controlled to less than a micron in most cases.

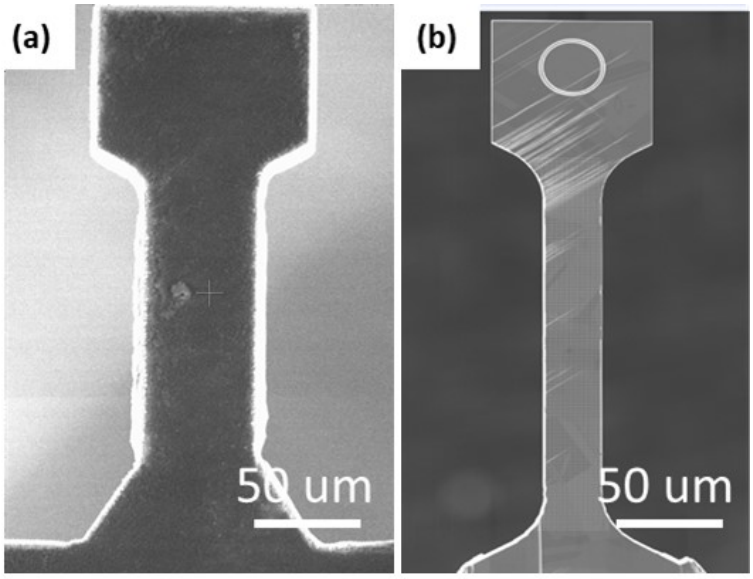

Figure 3-19: SEM images of (a) bulk machined microtensile sample of René 88DT with femtosecond laser and (b) final milling of the same sample with FIB

Though wire EDM is a technique typically applied at the macro scale, it is clear that with proper optimization, it can also be applied at a scale on the order of a few hundred micrometers up to much larger scales with damage still on the order of single digit microns. To highlight the scales at which each technique is best applied as well as to set the stage for the studies presented in Chapters 4 and 5, Figure 3-20 shows the three microtensile geometries that were tested, each machined using one of the three techniques presented in this chapter.

Understanding the capabilities of these three techniques can lead to a methodology that allows for machining of materials at multiple length scales in order to study size effects. It can also be applied to develop sample geometries not only for microtensile testing as discussed in this paper, but for developing other microscale

samples, such as microcantilevers for studying fatigue or microbending samples for studying fracture toughness. The true benefit of being able to apply these techniques well is in combining the multiple techniques to be able to improve throughput of test samples in a way that hasn't been done before by capitalizing on material removal at the length scale that each technique has shown to be most effective at.

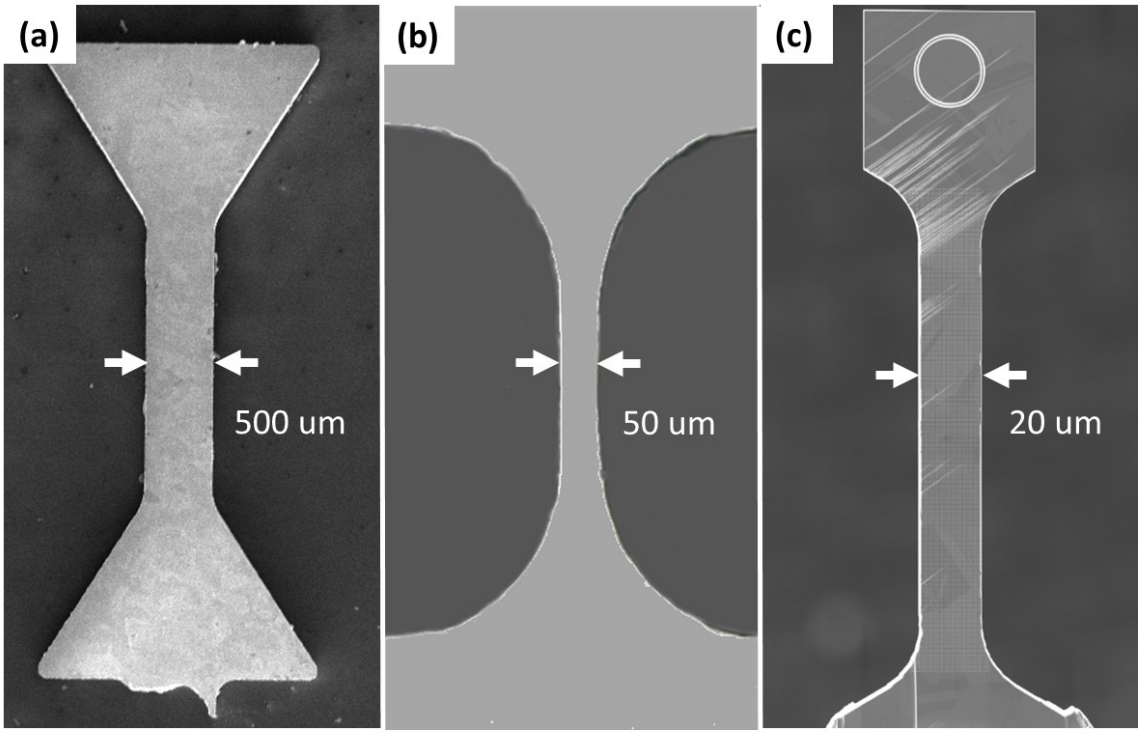

Figure 3-20: Images of microtensile samples machined using: (a) wire EDM, (b) fs laser and (c) FIB.

3.7 Summary and Conclusions

Being able to develop techniques with different material removal rates and applicable length scales, as well as the ability to optimize these techniques, is critical to being able to manufacture and test microtensile samples. Sample quality can have a

significant impact on microtensile sample results, especially when probing lower length scales. There is an inherent stochasticity that arises from testing materials at smaller length scales, as will be explored in Chapters 4 and 5, and specifically in the single crystal and mesoscale regimes where microstructural features give rise to a multitude of material responses for different samples of the same size. In order to properly study these microstructural and size scale effects, artifacts from factors such as surface roughness need to be minimized. Due to the differences in scale of microstructure between different materials, having a variety of techniques that can be applied at multiple length scales is necessary in advancing the study of microscale mechanical behavior.

Widely used machining techniques such as FIB or wire EDM have been well established and are readily accessible, but there is quite a bit of room for optimization and understanding of how best to apply these techniques. It's easy to assume that these techniques will provide quality samples, but there is no panacea when it comes to selecting parameters for the number of materials that can be machined with these techniques. FIB and wire EDM machining techniques are both capable of machining at the two extremes of microtensile sample geometries. Through this work and in other studies, the femtosecond laser has been shown to be capable of producing samples at a previously inaccessible intermediate length scales. The development of femtosecond laser machining has allowed us to probe multiple length scales in René 88DT and the development of laser machining in particular opens up the ability to develop samples at the mesoscale, which allows for the collection of microstructurally dependent measurements.

Chapter 4: A Study of Sample Size Effects on Strength in René 88DT

4.1 Introduction

It is well known that microstructure plays a significant role in the deformation of metals and their mechanical properties. Examining the microstructure at different length scales reveals unique mechanisms governing the deformation, such as subgrain level interactions of dislocations, phase morphologies at the single crystal scale, or interactions between neighboring grains and twins at the polycrystalline scale. The ability to measure material properties at different length scales is critical to the development of multi-scale property prediction models. In this type of modeling, the use of a representative volume element (RVE), which can be further characterized as a property volume element (PVE) or microstructural volume element (MVE), is a key building block for the multi-scale framework [144, 145]. These elements represent the volume of material that must be considered to reach a convergence in the mechanical response or physical property, ensuring the results of the model at a larger volume have no size effects. However, there is a lot to be gained in understanding what factors microstructurally affect the convergence of properties so that the models can be used to capture this behavior on smaller length scales. Observing these trends experimentally and investigating the role of microstructure across length scales can lead to further development and benchmarking of well-informed models that utilize frameworks, such as the crystal plasticity finite element method (CPFEM), to accurately model the microstructure of materials at the polycrystalline scale [110, 146].

Although a lot of work has been done to investigate these size scale effects on sample strength in pure metals [13, 141, 147-153], more work can be done in this area with regards to structural alloys such as René 88DT. Samples were tested across multiple length scales, ranging from one grain through the sample thickness up to the bulk scale, and their yield strengths were determined in order to evaluate the divergence from the bulk strength. It was expected that the amount of variability in the data would increase with decreasing sample size as discrete microstructures were realized. As the sample size decreases, close to one grain through the thickness, we expected to observe various mechanical responses while approaching the single crystal length scale. This scatter in mechanical response is reported in literature [115] for various experimental designs [4, 145]. Experimentally capturing the size effects over many length scales can provide a systematic approach to defining a RVE, particularly in materials that have not been previously modeled in this manner [149]. Using the data collected in these experiments can lead to a better understanding of the role of microstructure and size scale effects in René 88DT and other FCC materials. Additionally, these methodical studies aid in the development and benchmarking of models that capture mechanical behavior.

4.2 Experimental Methods

4.2.1 Overview of Tested Samples

Figure 4-1 shows an image of the three different samples geometries used to test at different scales, each manufactured from a foil of René 88DT using the machining techniques discussed in Chapter 3. The largest dogbone shaped samples, with thickness and width ranging from 200-500 μm, were manufactured using wire EDM, Figure 4-1a. The smallest samples (Figure 4-1c), with thickness and width of 20 μm, were manufactured using the automated FIB machining process described in 3.3.2.

Intermediate sized samples, shown in Figure 4-1b, with thickness and width between 50 and 100 μm were machined using the femtosecond laser. The microstructural volume tested in the intermediate laser samples and small FIB samples represent the mesoscale of René 88DT. A more in-depth study of the characterization and analysis of samples in this mesoscale regime will be explored in Chapter 5. While the automated FIB process was described in Chapter 3, the laser machining process for these 50-100 μm samples will be described in the subsequent section.

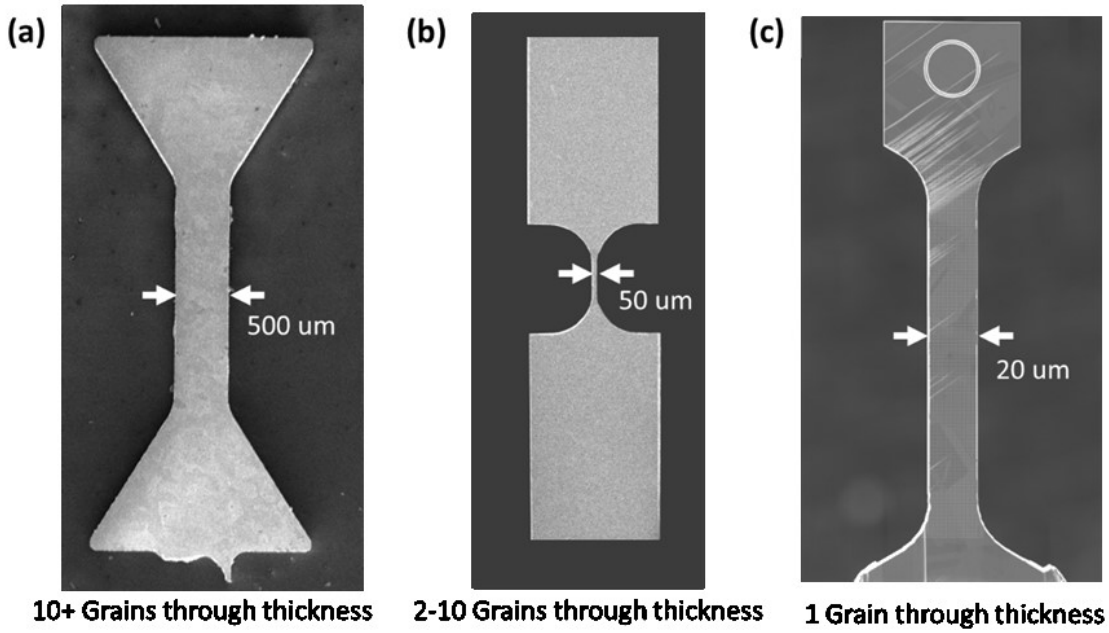

Figure 4-1: Images of René 88DT microsamples at different length scales machined using: (a) wire EDM, (b) femtosecond laser and (c) FIB.

4.2.1.1 Laser Machining of Mesoscale Samples

The geometry for the laser machined mesoscale samples was inspired by previous work done by the Hemker group in manufacturing and testing thin films. As shown in Figure 4-2, the sample consists of two large grip sections that transition to a much smaller gage section of 100 μm, or smaller. Using both the laser machining techniques of a

trepanning cut trajectory and inclining the beam to reduce taper in the sample edge, these mesoscale samples were cut using a multiple step process as illustrated in Figure 4-3.

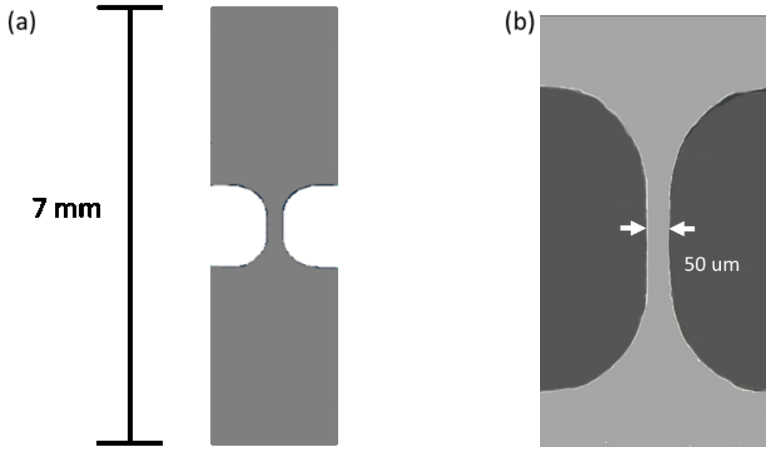

Figure 4-2: (a) Schematic of femtosecond laser-machined mesoscale sample of René 88DT and (b) magnified view of sample gage section.

First, each side of the gage and transition sections of the sample are cut out from a foil using the optimized process that was developed for this material as follows. The entire D-shaped bulk cut uses 300 total passes, shifting the location of the focused laser spot down by 10% of the sample thickness every 30 passes, a stage speed of 3 mm/s and a laser energy of 50 μJ. To achieve the final dimensions of the D shape, 3 sets of 200 passes of the beam are made for a total of 600 total passes using a beam energy of 20 μJ. The location of the focused laser spot is shifted down by 10% of the sample thickness every 20 passes and then returned before the beginning of the next set. For each set, the beam is moved 7 μm closer to the center of the sample gage, cutting the gage width to be 21 μm narrower after this procedure than the initial bulk cut. Once the entire gage and grip transition geometry is cut, the final step is cutting out the outer sample geometry,

consisting of the large grip ends of the sample. This process is executed using higher beam energy, 100 μJ, to reduce the amount of time. No specific number of passes is executed for this step; the cutting is performed until the sample is released from the bulk foil. Laser damage and accuracy is not a concern for this last step since the tolerance of the geometry of these sections is not critical to mechanical testing. Thereafter, a freestanding sample is separate from the foil for further preparation, characterization and testing.

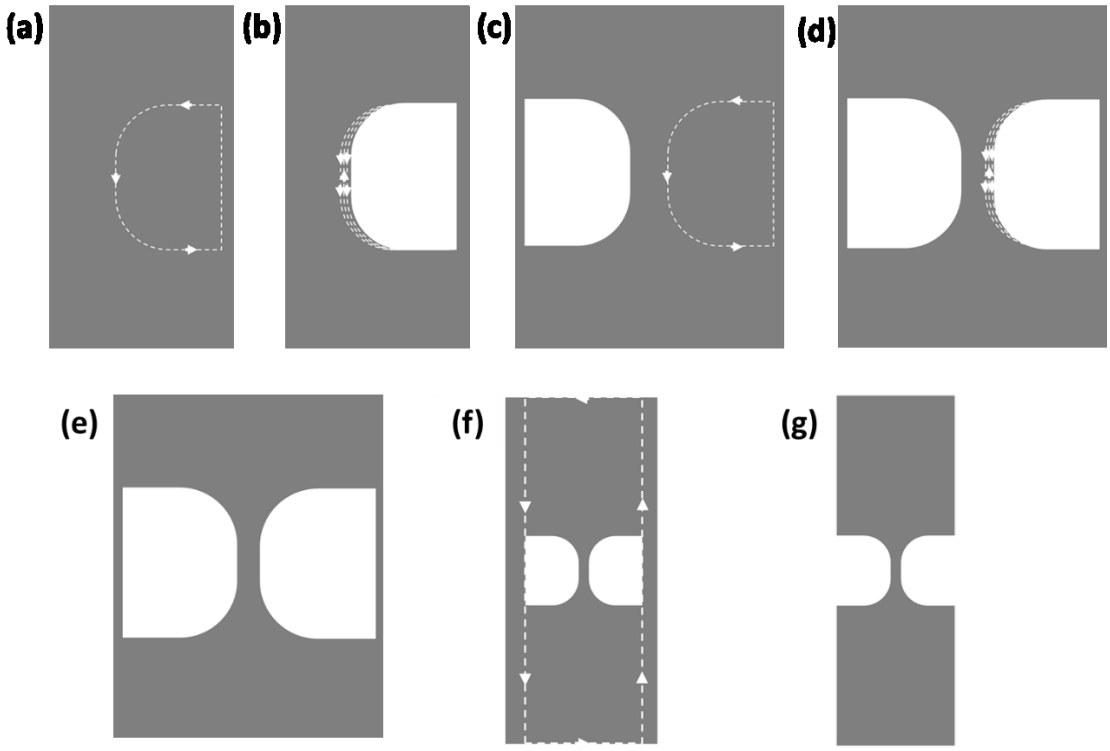

Figure 4-3: Schematic of laser machining process for mesoscale samples. In (a) the bulk cut of the gage and transition regions is performed, followed by (b) rapid passes at a lower energy to shape the final geometry. The sample is then rotated, and the process is repeated as shown in (c) and (d) to achieve the final gage geometry shown in (e). Finally, as shown in (f) the outer sample geometry is cut using a higher beam energy, leaving the freestanding sample geometry in (g).

4.2.2 Microtensile Testing with JHU Ex Situ Load Frame

In the Hemker lab, there are multiple microtensile testing setups that utilize similar configurations. An image of the particular load frame used in this study is shown in Figure 4-4. This load frame has a load capacity of 1200 N and consists of 4 main components: the air bearing, the load cell, the linear actuator and the mechanism for gripping and pulling the samples during a test. The air bearing assures alignment and eliminates friction from the pull bar as it slides during the test, removing the possibility of erroneous load readings. A Futek load cell is mounted in line with the tensile axis of the sample and is set to record load data at a rate of 10 points/second. A screw drive Zaber linear actuator that retracts at a constant speed to maintain a constant strain rate of 10^{-4}/s was used.

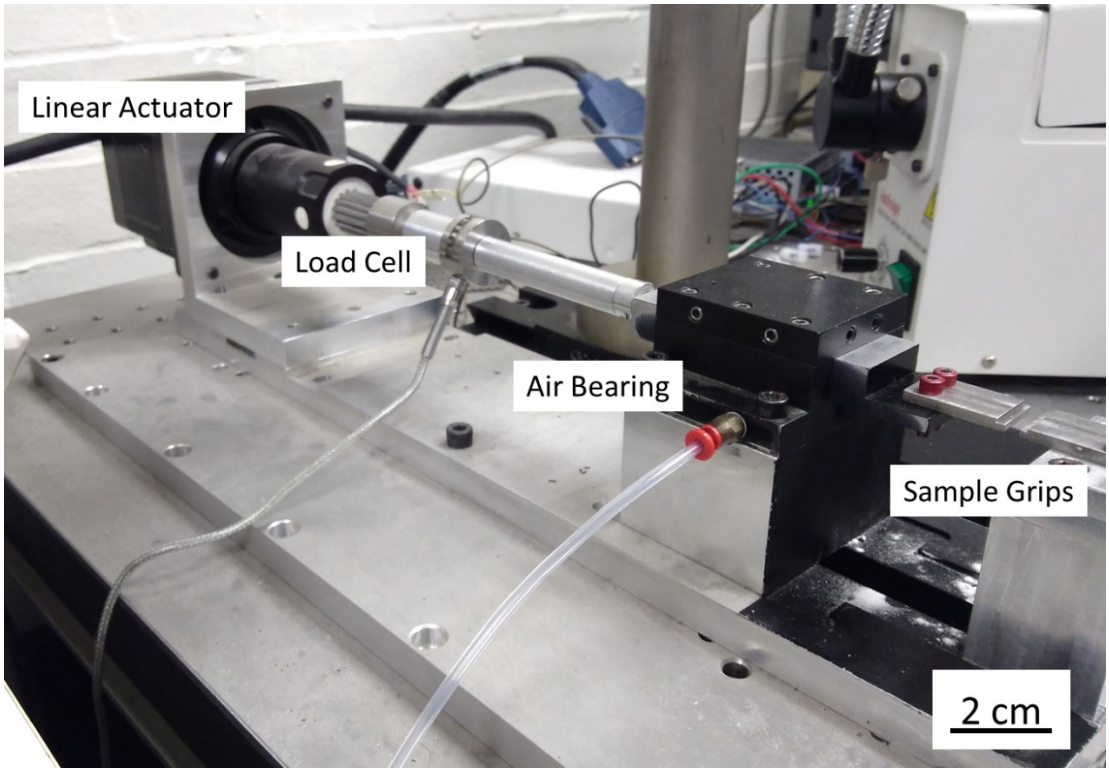

Figure 4-4: Image of ex situ load frame with major components labeled.

For the dogbone shaped samples sized 200 μm and larger, a custom set of high strength titanium grips were utilized, model and dimensions shown in Figure 4-5. One grip was attached to the end of the pull bar that slides within the air bearing while the other grip is mounted on a block opposite from the pull bar, which remains stationary during the test. At the beginning of the uniaxial tension test, the sample self-aligns as the shoulders of the sample slide into place of the custom designed grips. Once the sample and grips come into complete contact, the sample begins to load up in tension as the actuator continues to retract.

For the laser machined mesoscale samples, the same load frame was used as for the larger samples, however, a different set of grips were designed. Despite the gage section of these samples only being 400 μm long, as shown in Figure 4-2, the overall geometry of these samples is 7 mm in length and composed of two large grip sections on either end of the sample. This modified grip geometry allows for the samples to be more easily handled despite the small gage section. Additionally, since the grip geometry remains invariant for these intermediate gage size samples, the same set of grips can be used across all samples machined using this methodology. Unlike the pocket grips used for testing the dogbone samples, these grips were machined as plates with a 2 mm ledge cut out at the end. A model and dimensions of these plates are shown in Figure 4-6.

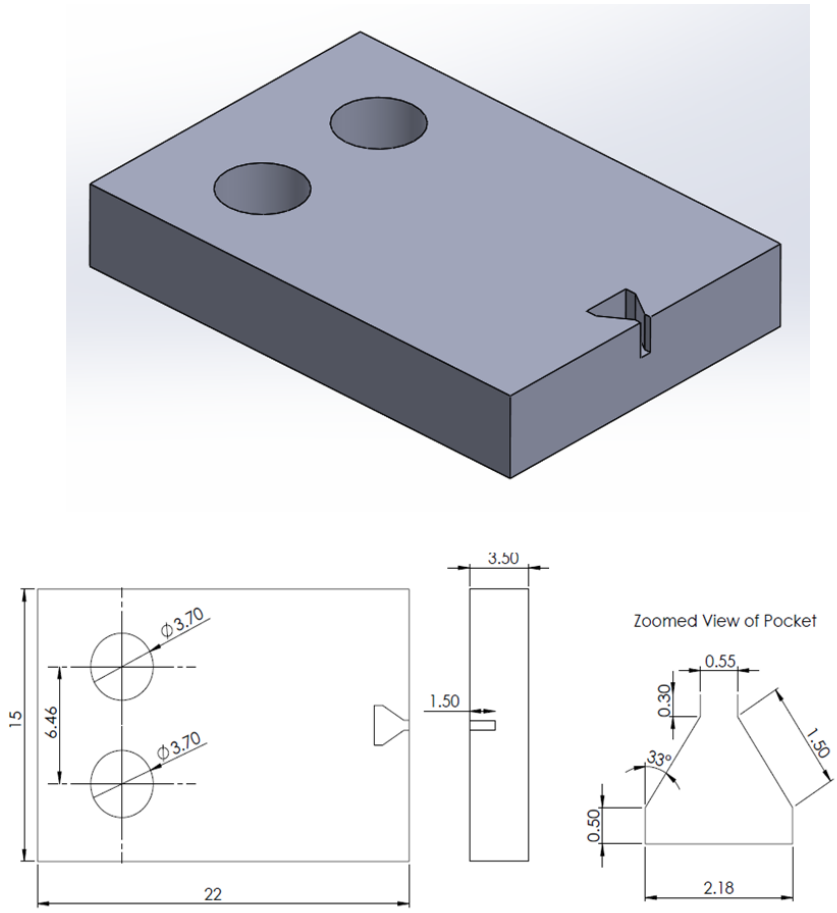

Figure 4-5: (a) Model of test grips for dogbone samples used in ex situ load frame and (b) drawing of test grip with dimensions labeled in mm.

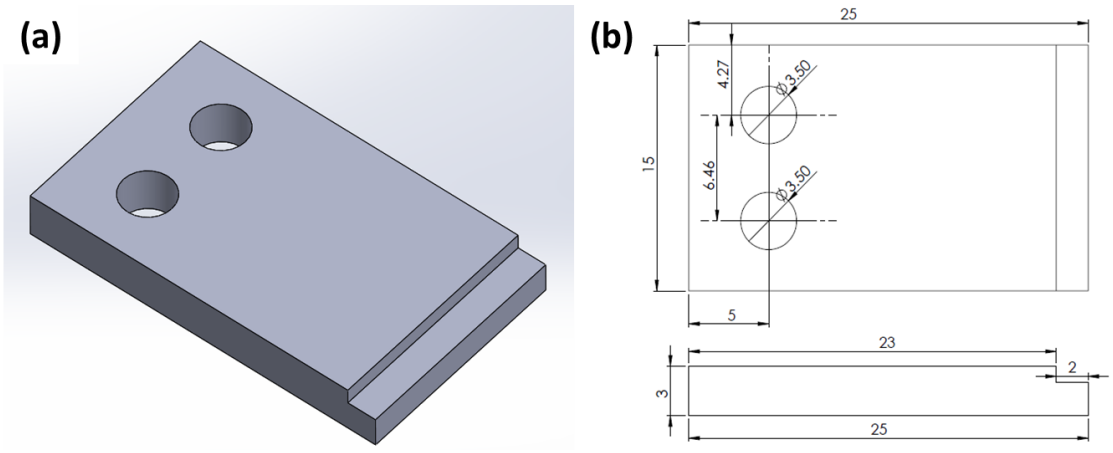

Figure 4-6: (a) Model of sample test plates for laser-machined samples used in ex situ load frame and (b) drawing of test plates with dimensions labeled in mm.

The grips are checked for alignment while in contact with each other, then the moveable grip is retracted enough to set the sample in place. The sample rests on each end of the cut-out ledges and is subsequently affixed to the test plates by applying Loctite 420 adhesive and allowing it to dry. The mechanical strength of the dried adhesive is strong enough to hold the sample fixed on each plate as it is pulled in tension.

4.2.3 Ex Situ Imaging

A digital camera is mounted above the sample during testing to collect images of the sample during testing that can be post processed using digital image correlation (DIC) to calculate strain. The camera used with this setup was a 6.6 MP PixeLink camera that interfaced with a computer via Firewire cable. PixeLink brand cameras utilize proprietary software to control the image settings and the acquisition rate. For the tests performed, images were acquired once every second during testing for several reasons: to ensure a long enough exposure time of 0.2 s, to allow the computer to save images accurately without being slowed down by acquiring too many images at a time and to simplify the process of obtaining the stress-strain response of tested samples. The latter will be discussed in more detail in this chapter.

For the large and intermediate sample sizes, different sized fields-of-view (FOV) were required based on the sample geometry. Thus, two different lens setups were utilized. For the dogbone shaped samples, the camera was equipped with an Edmund Optics R-200 rear assembly and OBJ-9 front objective, giving a 5.25 x 3.86 mm^2 view field. For the laser machined mesoscale samples, an Edmund Optics R-6 lens was used in

conjunction with a Mitutoyo 10x microscope objective allowing for a significantly smaller field of view of 1.05 x 0.77 mm^2. During imaging, symmetric and consistent lighting was required to capture images. For the R-200 rear assembly and OBJ-9 front objective setup, a ring light mounted around the objective to provide diffuse lighting. Although the ring light provided ample lighting for this optical setup, it could not be mounted with the 10x microscope objective, so a dual gooseneck illuminator was used instead. This light source was still able to provide adequate lighting since the surface area of the gage section was relatively small. Images of both lighting setups and the positioning of the camera and lenses for each set of tests are shown in Figure 4-7.

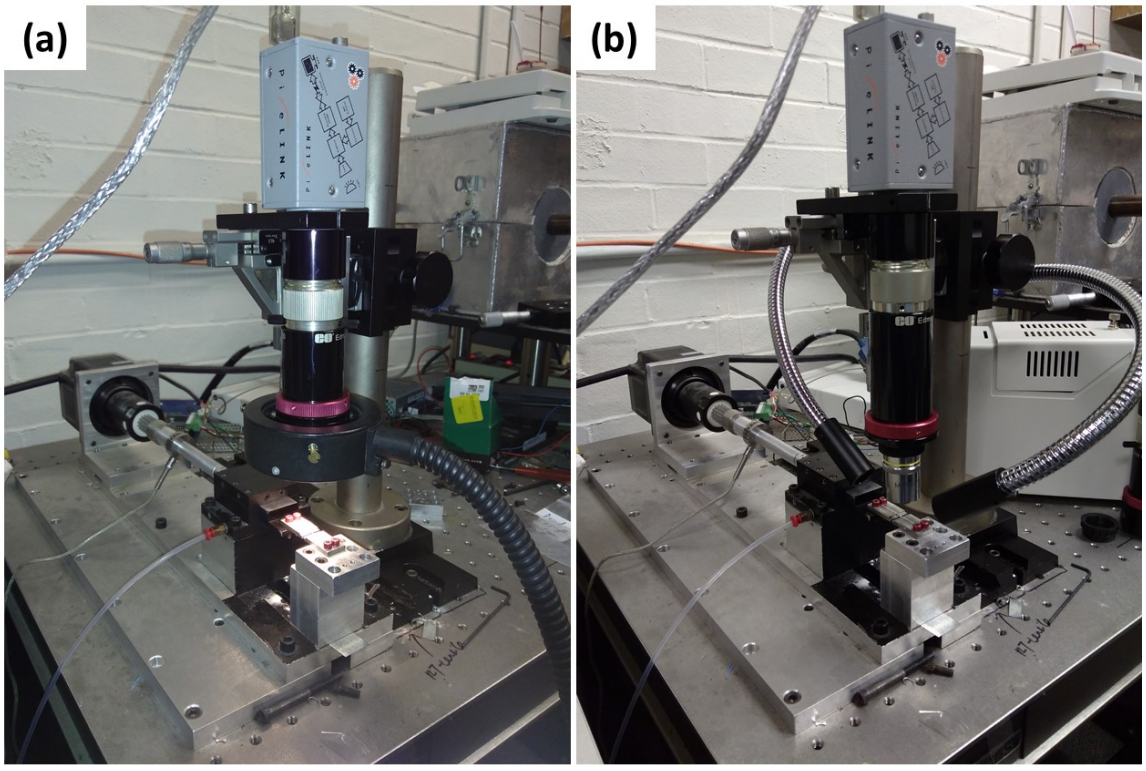

Figure 4-7: Image of lighting arrangements in test setup using (a) ring light and (b) dual gooseneck light.

4.2.3.1 Digital Image Correlation of Ex Situ Imaging

Microscale samples are both too small and too fragile to utilize traditional strain measurement techniques, such as strain gages and extensometers. DIC was implemented in post processing images of the sample surface captured during testing. The technique was initially introduced in the 1980s by Peters [154] and Sutton [155], and has become a common technique in mechanical testing. DIC relies on obtaining a series of images of the test sample, one before it deforms and then all throughout the deformation. Within those images, a selected region of interest is discretized into subsets, the positions of those subsets are tracked in each image, and then obtaining the raw displacements from the motion of these subsets relative to one another in sequent images. In order for the subset tracking algorithm to perform well, it is necessary that there is enough contrast on the sample surface for each subset to have a unique grayscale profile that can be identified image to image. The well-polished surface of a sample alone does not have enough contrast in order to track each subset well, so a suspension of acetone and 1 μm average diameter alumina powder, in a ratio by volume of 10:1 acetone to alumina powder, is applied to the sample in order to create a speckle pattern to provide the necessary contrast. With the proper lighting as outlined previously, the alumina particles show up bright on the dark background of the sample surface in the images captured by the digital camera. Figure 4-8 shows an example of an image captured during testing to demonstrate what a speckle pattern on the sample surface looks like and the contrast between the sample and the contrast that is created by the speckling technique.

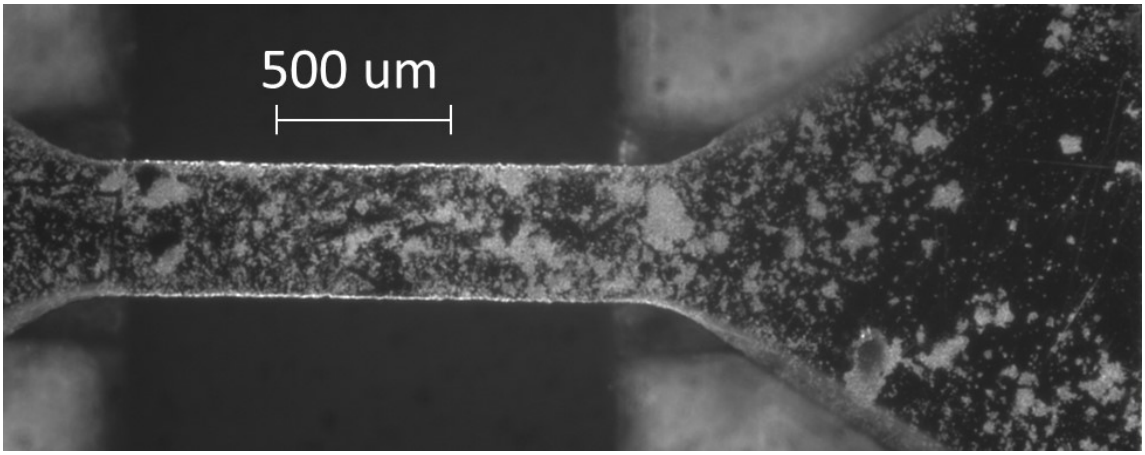

Figure 4-8: Image of sample gage section captured during mechanical testing showing alumina speckle pattern on the sample surface.

The strain that is subsequently calculated from the displacements obtained from DIC can be 1D, 2D or 3D depending on the manner in which images are captured. In the results presented in this chapter, a MATLAB based code developed by Chris Eberl and collaborators [156] was used to calculate the 1D average linear strain along the tensile axis in each sample. For each image, a plot of the measured uniaxial displacement, obtained from the DIC results, versus subset position is fit with a linear function for that particular image. The slope of the line that fits the data is the true strain for the image and is recorded along with the image number and timestamp, to be utilized later. An example of this is shown in Figure 4-9, demonstrating a linear fit of data from tracking points on a Displacement vs Position plot.

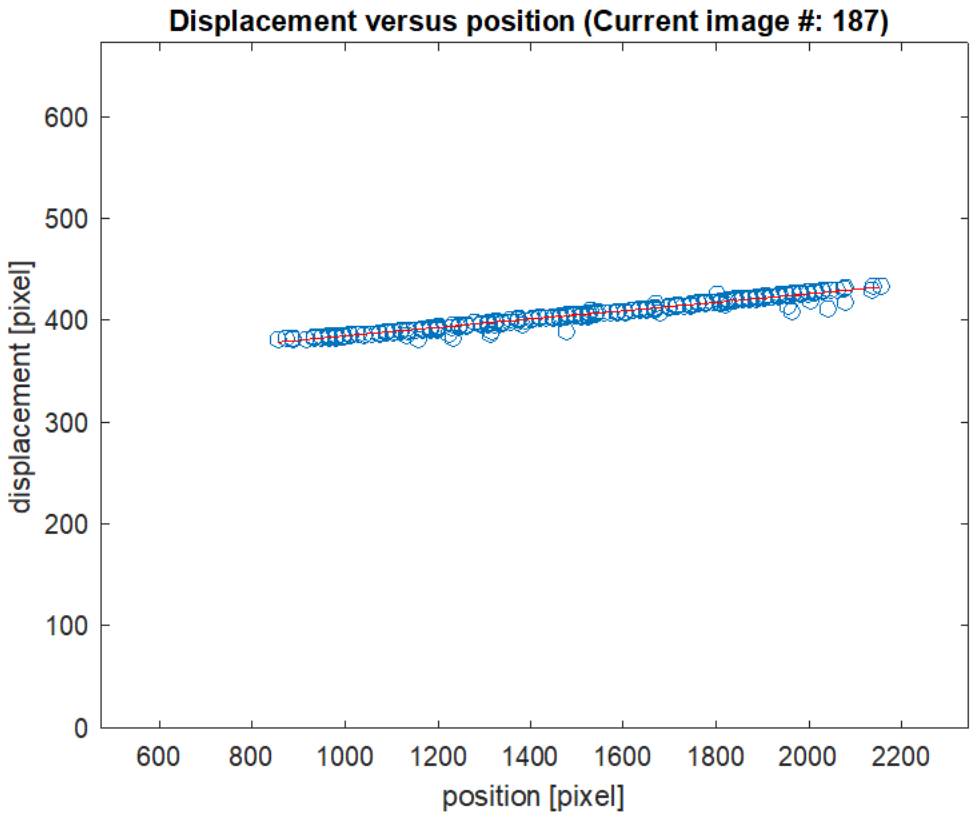

Figure 4-9: Plot of Displacement vs Position for DIC tracking points with linear fit line in red.

This method only provides 1D strain data along a particular direction, here the tensile axis of the tested sample, which is sufficient for this experiment to obtain the uniaxial stress-strain response of each sample and the requisite mechanical properties. Although there may be inhomogeneous strain localizations in the samples, especially after yielding, the global average strain in the sample is all that is required for the stress-strain curve since DIC tracking around localizations yields higher or lower levels of displacement than the rest of the sample. A discussion of the implications of these locations and how the averaged strain remains unaffected are included in 4.4. However, these strain localizations are important in developing and analyzing 2D surface strain

maps in tested samples. In Chapter 5, a methodology using the commercial software VIC-2D (Correlated Solutions) to do so will be explored. In addition, for a more detailed discussion of DIC and calculation of the strain using the technique see [157].

4.2.4 Microtensile AFRL In Situ Load Frame

For the 20 μm FIB machined samples, a separate custom-built load frame was utilized. The frame was displacement-controlled using a piezoelectric actuator, load was measured with a strain gage-based load cell and mechanical testing was performed in situ using a FEI Quanta SEM. The foil that the samples were machined at the edge of was attached to a bulk sample holder that was subsequently mounted to an Attocube controlled x-y-z micro positioning stage allowing for precise movement and positioning. The samples were positioned and lowered into a SiC grip that is 8 mm long and 0.1 mm in diameter connected directly to a load cell. The tests were conducted in a quasi-static manner at an average strain rate of 10^{-4}, where the samples underwent cycles of loading at a constant actuator voltage ramp rate and then held fixed for acquisition of an SEM image. A schematic of the load frame and the sample loaded into the grips are shown in Figure 4-10. A more detailed description of the in-SEM load frame and testing procedure can be found in [158, 159].

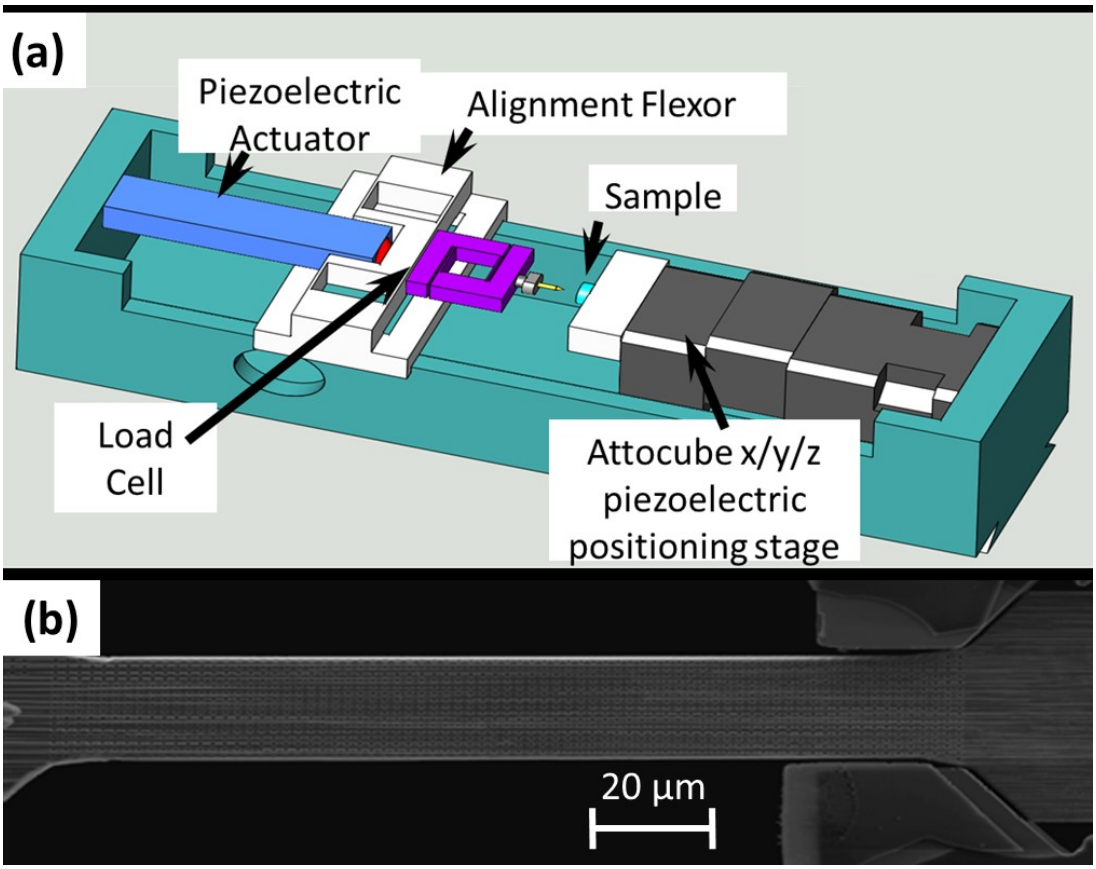

Figure 4-10: (a) Model of in situ load frame with major components labeled and (b) SEM image of microtensile sample loaded in SiC grip. The head of sample on the right side of the image is pulled by the SiC grip and the left end of the sample is fixed as it is attached to the bulk foil it was machined from.

4.2.5 In Situ Imaging and Digital Image Correlation

Unlike for ex situ testing, images were captured during periods in which the actuator was held still at a constant voltage, allowing still image collection given the scan speed and resolution of the SEM. The entire process of performing the mechanical test and collecting SEM images was automated using custom scripts written in LabView. In the samples tested ex situ, a speckle pattern was applied to the surface of the sample to create contrast for DIC. While this can be done for samples tested in situ [160, 161], a different method was used for these samples. A periodic grid of 250 nm circular markers, each 200 nm deep with 1 µm spacing was FIB milled onto the surface of the samples

after the final sample geometry had been machined, seen in Figure 4-11. The grid of markers extends from the end of one grip-to-gage transition to the other along the entire length of the sample gage.

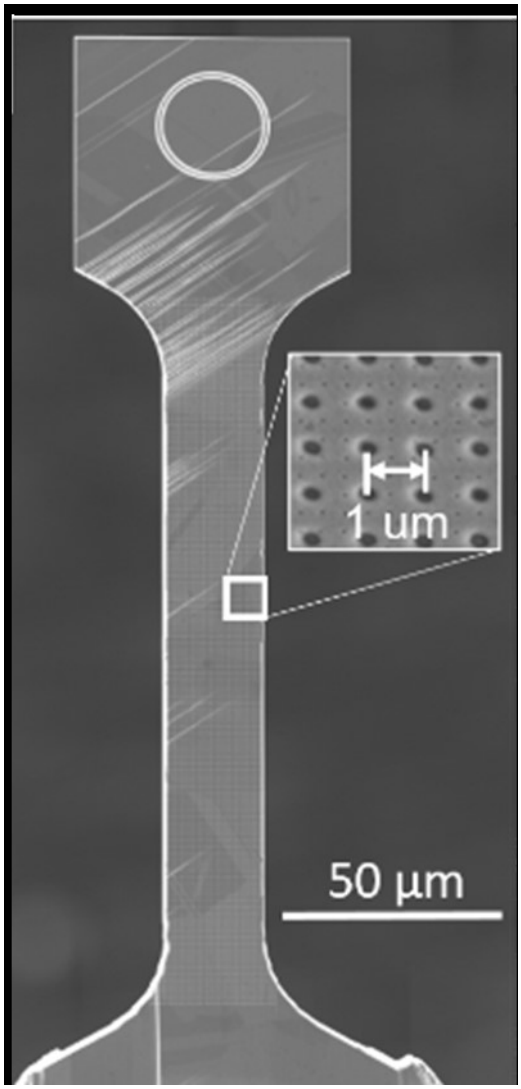

Figure 4-11: 20 µm thick sample with a magnified inset showing FIB marks used for DIC tracking.

A MATLAB script was used in order to determine the position of each marker from the images taken during a test. In each image, the grayscale was inverted so that each of the dark markers (inset Figure 4-11) would appear as a bright circle. A gaussian

peak finding algorithm was then applied to the image to find the position of the centroid of each bright spot from image to image. This tracking method of finding the position of each subset is similar to the DIC method discussed previously. Once the position of each marker could be determined, the 1D displacement and strain in the sample could be calculated as well using the same procedure develop by Eberl as before [156].

4.2.6 Obtaining the Stress-Strain Response of Tested Samples

Once the load data from a test was collected, the engineering stress could be determined from the recorded load and the measured undeformed cross-sectional area of the sample. Since the strain calculated from the DIC MATLAB script was the true strain and the calculated stress was engineering stress, the stress had to be converted to true stress before extracting mechanical properties. In order to convert the data accordingly, the following equations were utilized:

Equation 4-1:

$$\varepsilon = ln(1 + e)$$

Equation 4-2:

$$\sigma = s(1 + e)$$

Where ε is the true strain, e is the engineering strain ($\frac{\Delta L}{L_0}$), σ is the true stress ($\frac{P}{A}$) and s is the engineering stress ($\frac{P}{A_0}$).

Each image had a corresponding strain and time stamp, while each load value recorded had a corresponding stress and time stamp, the stress-strain response was obtained by stitching these two datasets together. The timestamp was matched every one second and the associated stress and strain values were extracted. A plot of engineering

stress vs engineering strain was made for each sample. The elastic modulus of the sample was determined from the plot of engineering stress versus strain using the slope of the linear elastic loading of the curve. Alternatively, the elastic modulus can be measured in the plastic region if unload and reload of the sample is performed during testing. The yield strength of each sample was determined by using the 0.2% yield strength offset method. A line parallel to the elastic region was drawn on the curve that passes through 0.2% strain and its intersection with the stress-strain curve of the tested sample provides the yield stress [162]. The results of the mechanical testing for all tested samples are presented in the next section.

4.3 Experimental Results

Figures 4-12 through 4-17 present stress-strain curves of polycrystalline René 88DT samples from 20-500 μm and demonstrate the drop in yield strength and increase in variability of mechanical response as the sample size decreases. The samples in Figures 4-12 through 4-15 were tested to failure, whereas the samples in Figures 4-16 and 4-17 were tested to a limited amount of plastic strain in order to preserve the sample for 3D characterization. Sample 4 in Figure 4-13 and Sample 5 in Figure 4-14 appear to have failed prematurely, however their modulus and strength values match within 5% of the other tested samples at their corresponding sizes.

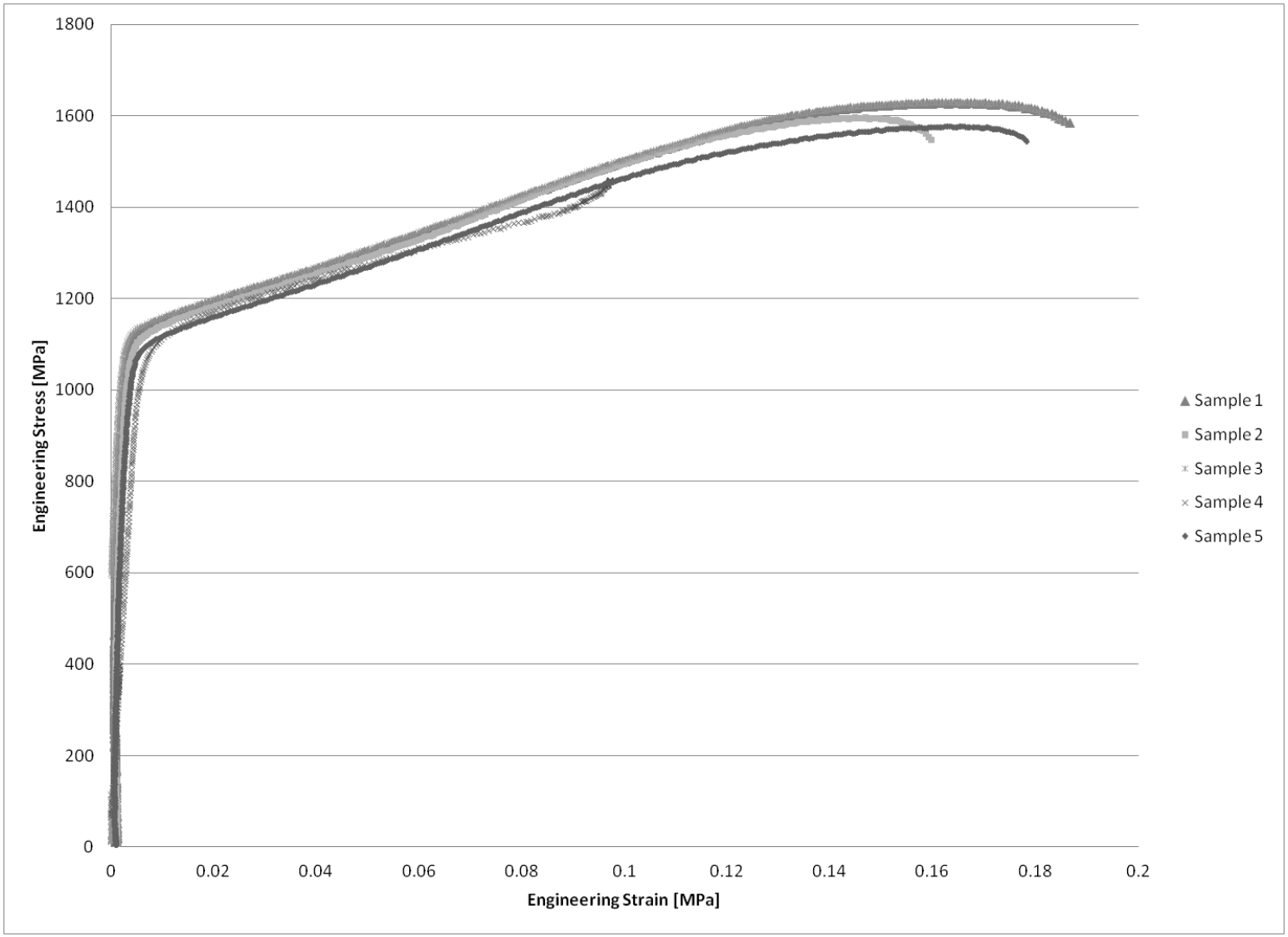

Figure 4-12: Stress-strain curves for tested samples with nominal thickness of 500 μm.

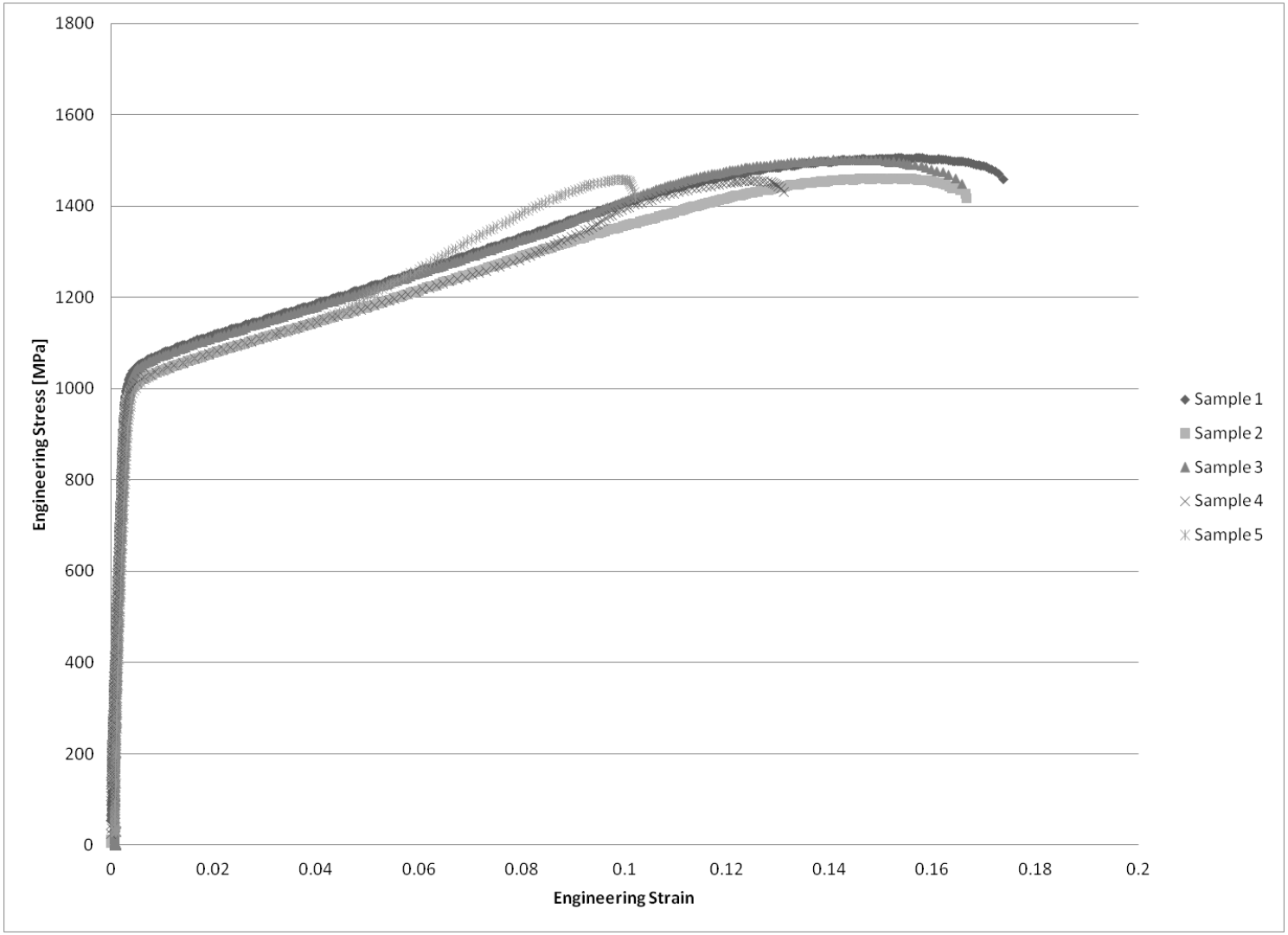

Figure 4-13: Stress-strain curves for tested samples with nominal thickness of 400 µm.

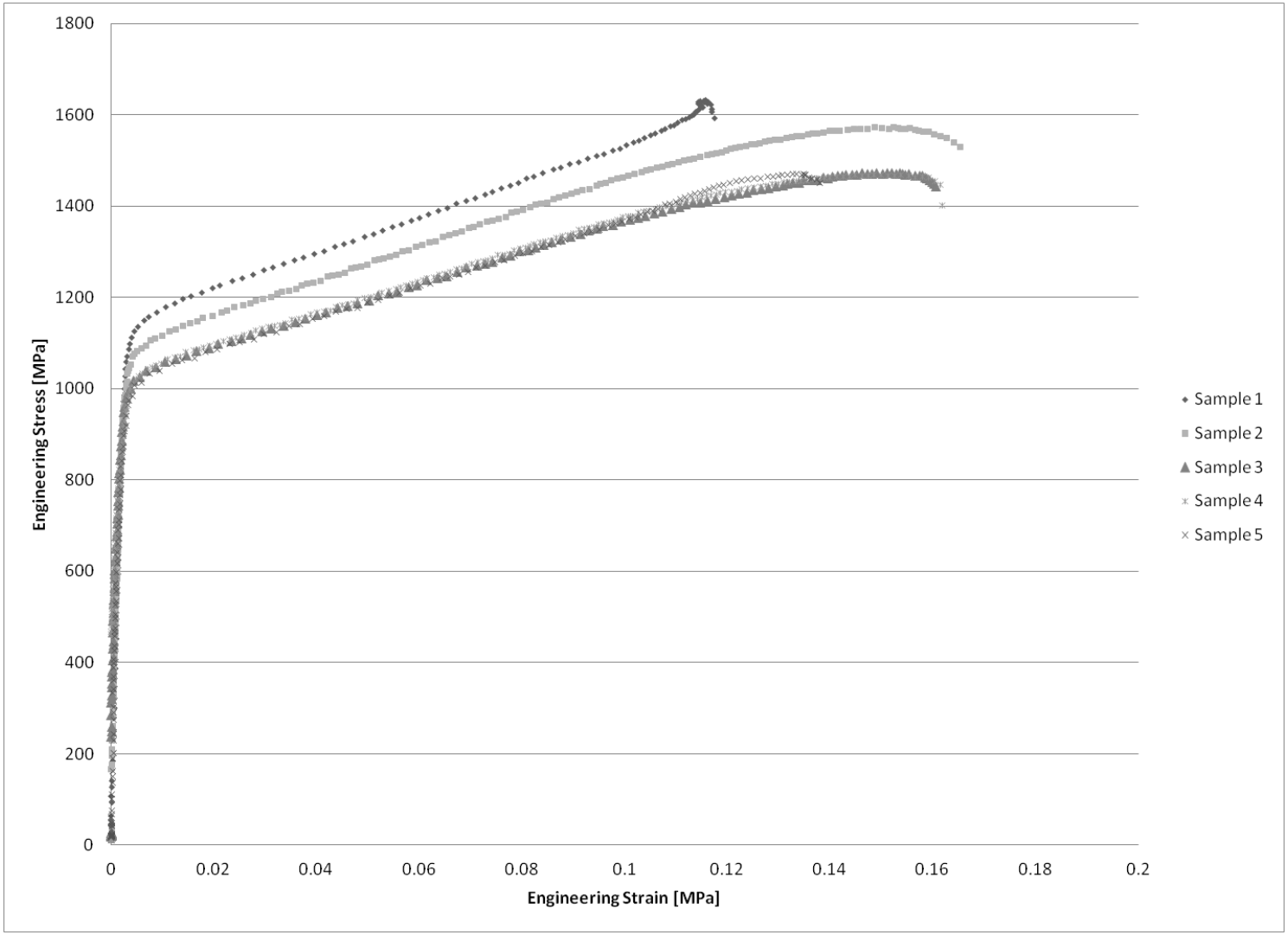

Figure 4-14: Stress-strain curves for tested samples with nominal thickness of 300 μm.

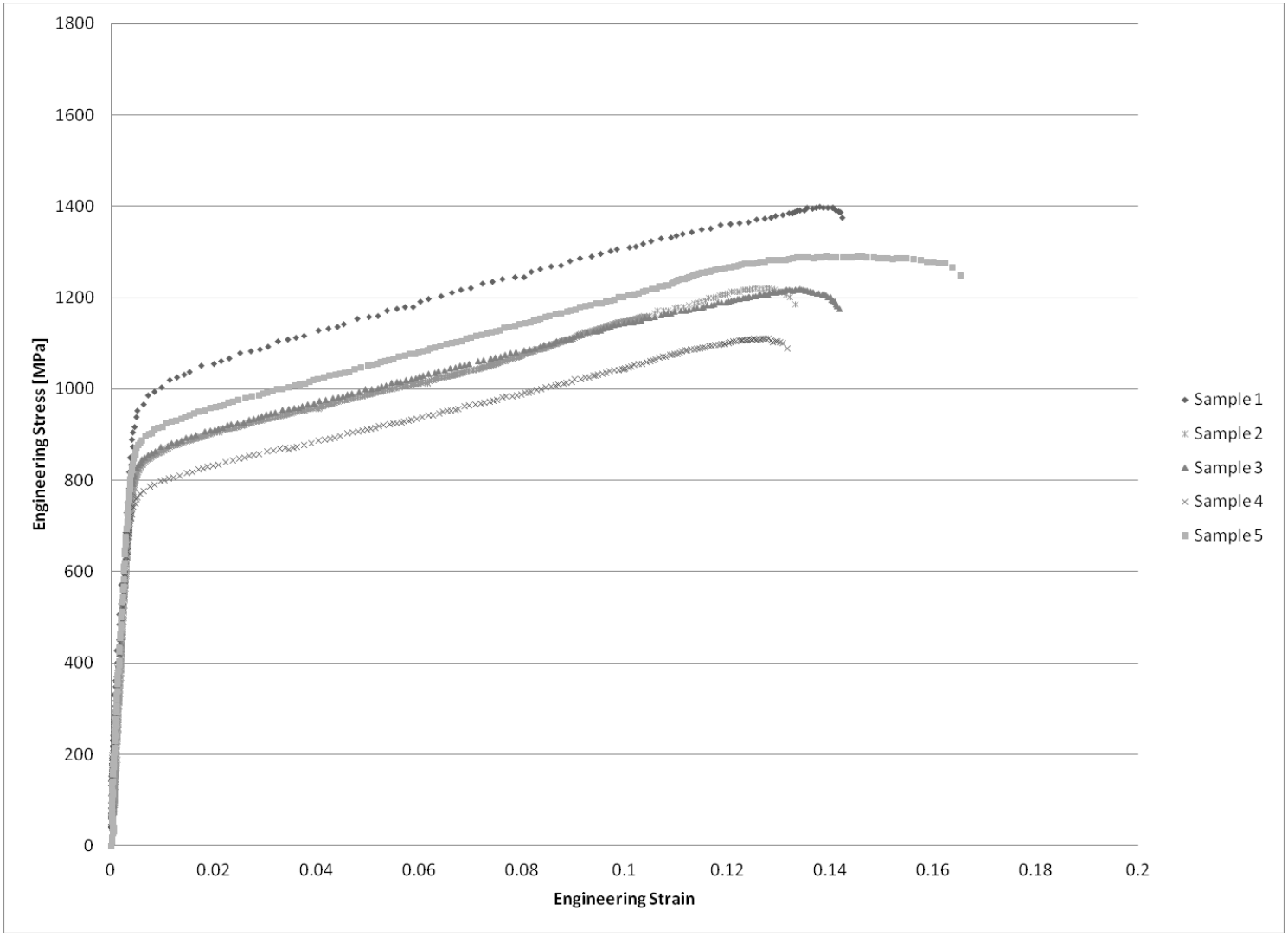

Figure 4-15: Stress-strain curves for tested samples with nominal thickness of 200 μm.

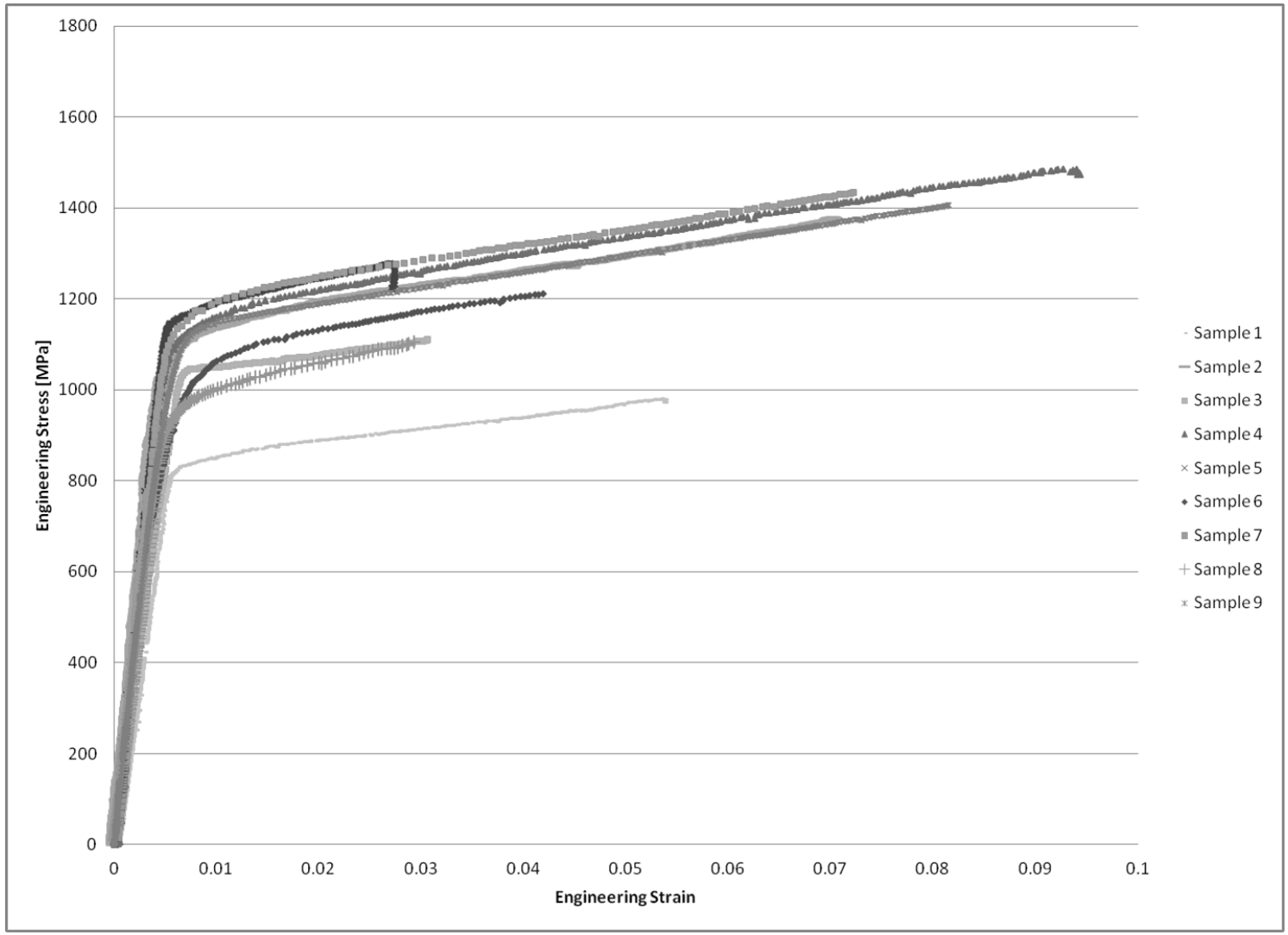

Figure 4-16: Stress-strain curves for tested samples with nominal thickness of 100 μm.

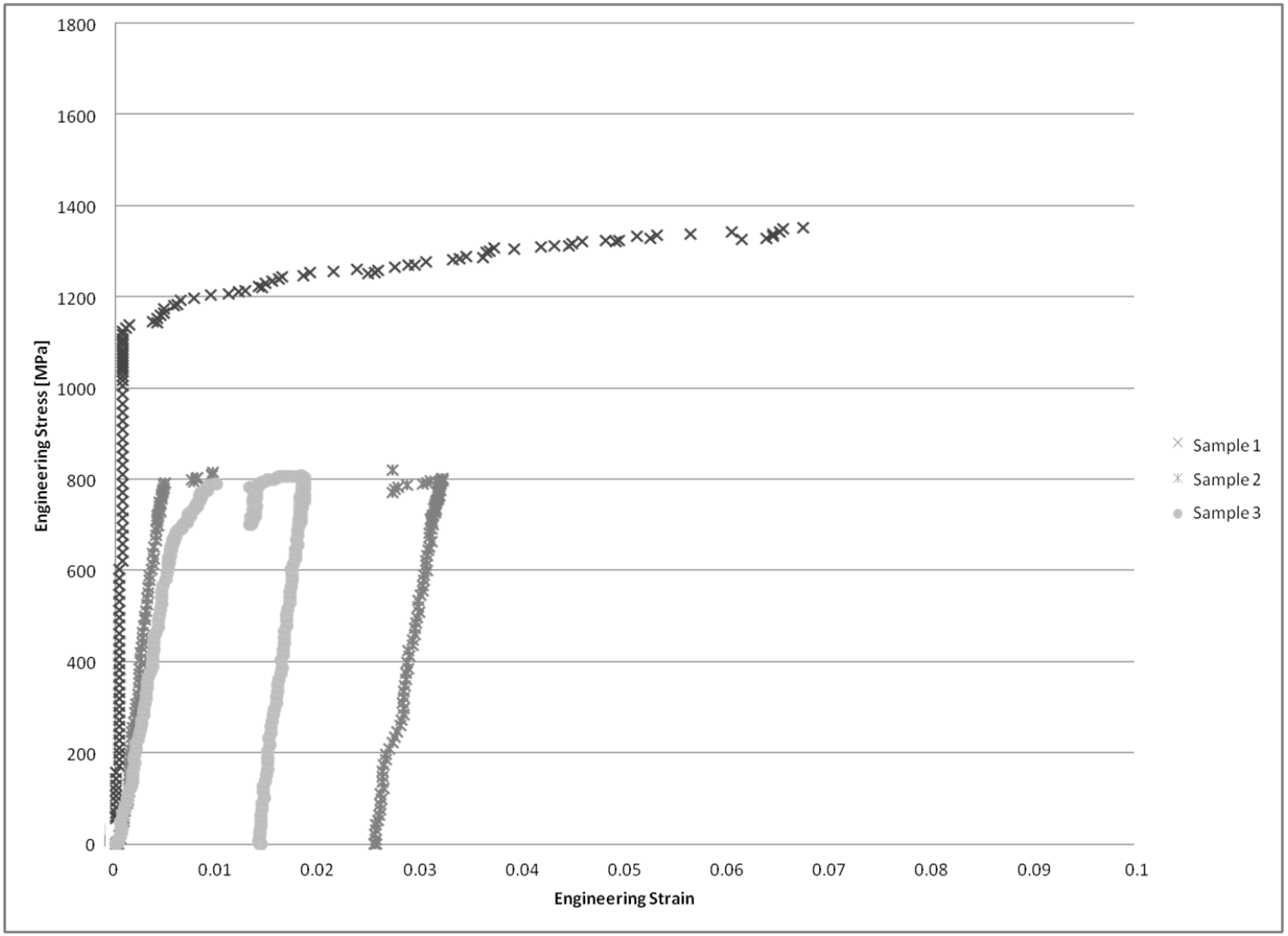

Figure 4-17: Stress-strain curves for tested samples with nominal thickness of 20 μm.

For each of the tested samples, the yield strength was determined from the stress-strain response collected using the method of 0.2% offset yield strength previously described. Figure 4-18 presents a summary of this yield strength data from the tested samples as a function of the normalized sample width and thickness. This normalized width and thickness was calculated by dividing the sample thickness by the 20 μm average grain size of the material. Using this parameter allows for comparisons between samples of different sizes, but also gives an idea of the number of grains through the thickness and with of the sample, and therefore the total number of grains within a sample gage volume.

In the largest samples 500 μm in thickness (normalized thickness of 25), the yield strength is consistent and matches with bulk values from the literature [67, 163]. As the sample thickness decreases to 300 μm (normalized thickness of 15), the average yield strength decreases slightly but the strengths remain consistent from sample to sample, varying by less than 3%. Below this size, however, we begin to see the sample strengths vary significantly down to a strength of about 650 MPa for samples 20 μm in thickness (normalized thickness of 1). The calculated strain hardening exponent ranged from 0.17 to 0.21 across all tested samples with no apparent size effect.

Two data points of the bulk strength of the material from literature are given as reference points to compare the experimental data with [108, 164]. The error bars for each sample represent the maximum potential error for the measurement which will be discussed in 4.4. What can be seen is that the error cannot account for the scatter in the data, but rather this is an effect of the microstructure being sampled. The overall decreasing trend as well as scatter in this data matches with the behavior that was expected that as the sample size decreases, the effect of

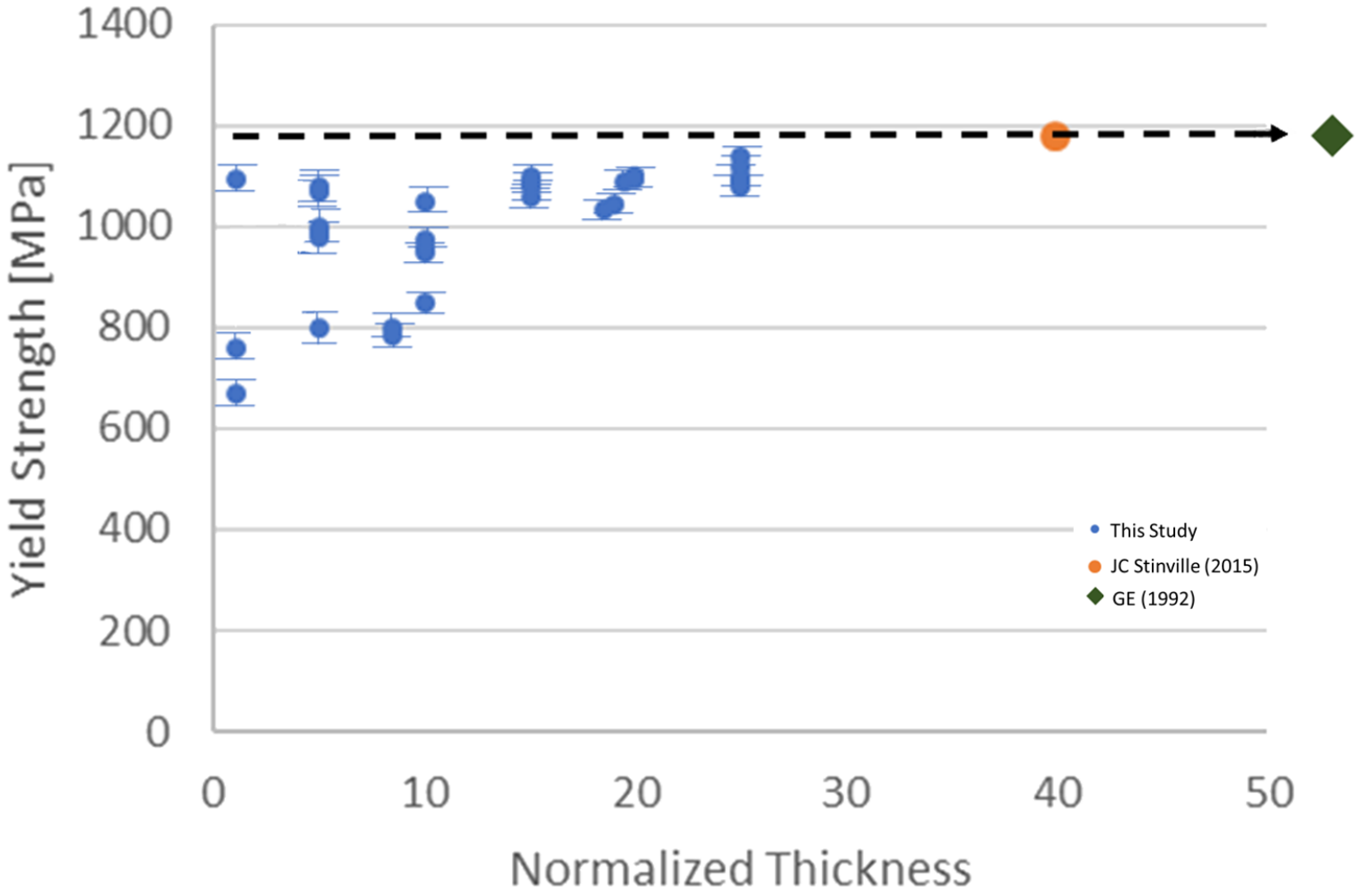

Figure 4-18: Plot of sample yield strength vs normalized sample thickness and reference data from literature. The error bars on each data point represent the maximum potential error of each measurement.

microstructure will play more of a role in determining the strength of the sample as compared to in the bulk size of sample where microstructural effects are averaged out.

4.4 Error Analysis of Experimental Results

A concern with regards to deducing the effect of microstructure on flow behavior is experimental error in the data. These potential errors result from the measurement of sample dimensions, load values during a test and error in the strain calculated using DIC, all of which could affect the measured yield strength.

4.4.1 Description of Measurement Methods and Errors

There are a potential number of sources of error that can affect the measurement of stress being made for each sample in our study. These errors can arise from the inaccuracy associated with equipment as reported by the manufacturer, as well as potential human error. The main value being calculated for the experiments is the stress that the sample experiences throughout the course of a tensile test. For the purposes of extracting a useful mechanical response from our experiments, we are interested in the stress of the cross section of the sample gage. Since it is difficult to determine the changing sample gage dimensions as a function of time, the initial sample dimensions are used with the measured load to produce engineering stress, which can be converted to true stress if desired. The calculation of engineering stress is simply:

Equation 4-3:

$$s = \frac{P}{A_0} = \frac{P}{(W)(T)}$$

where s is the engineering stress, P is the load on the sample in units of force and A_0 is the cross-sectional area of the sample, which can be calculated from the width W and thickness T of the sample.

It can easily be seen that three measurements must be made to calculate the engineering stress. Measurements of the width and thickness of the undeformed sample, which are assumed to stay constant and are taken before the test begins, and measurements of the load on the sample, which is measured and recorded

Sample dimensions are measured using a variety of methods in the laboratory, however, for this study a micrometer and an optical microscope were employed. The micrometer used to make measurements was a Mitutuyo 293-340-30CAL Digimatic Micrometer. This specific model has a NIST certified calibration with a resolution of 1 um and an error of ± 1 um as reported by the manufacturer. For this study a Zeiss Axiocam digital camera and optical microscope outfitted with 5x, 10x and 20x objective lenses was used. Images were captured with corresponding Axiocam software for measuring distance, with resolution of 0.1 μm with an error of ± 0.05 um. For this systematic experiment, the sample width and thickness were measured using the optical microscope while the thickness was verified using the micrometer. In all tested samples, the thickness measurements between these two methods were in good agreement, within 1 um, which is the resolution of the micrometer.

In addition, for samples 100 um and smaller that were tested in this study, machining was performed using FIB or femtosecond laser as the machining tool. Due to the size of these samples and the need to perform EBSD analysis, measurements of the dimensions was performed using a Tescan MIRA III SEM. The resolution of the SEM is

0.01 um, which has been calibrated to accurately measure within ± 0.005 um at 200x magnification. The load for the tested samples was measured using a Futek Load cell. This load cell has a resolution of 0.001 N with an error of 0.05 N reported by Futek.

The strain data was obtained via DIC, which included images acquired every one second and post processing in an open source MATLAB code [18]. The best way to measure the inherent error from the optical setup for DIC is to calculate strain from a sample undergoing rigid body motion. In theory, a sample in this state will not actually experience any strain, and therefore DIC methods should calculate zero strain in the sample. However, some small amount of strain is typically calculated depending on the test conditions and the resolution of the equipment. This calculated strain provides a baseline for the amount of error in the optical setup for DIC measurement technique. A series of rigid body displacement tests were performed using the same camera and load frame for the tensile tests carried out in the study. The sample was displaced at a constant rate while images were captured. Three different actuator speeds of 20, 50 and 150 steps/s were used to also examine if the actuator speed had any effect on the error generated, as the actuator speed varies for different sample sizes in order to maintain a similar strain rate.

For 1D average strain, it is only necessary to measure the displacement between two points at the ends of the sample gage section. However, using DIC to track the displacements of the entire gage section ensures improved accuracy during the strain calculation (linearization process) compared to two points. To show this, the error of including points in the middle of the sample gage as compared to only points at the

sample edges was determined. The strain was measured between points on either side of the sample gage and compared it to the strain measured for the sample using all tracking points.

4.4.2 Results from Error Analysis

A summary of the error associated with each of the physical measurements is presented in Table 4-1.

Table 4-1: Summary of Physical Measurement Errors

	Micrometer (µm)	Optical Microscope (µm)	SEM (µm)	Load Cell (N)
Resolution	1	0.1	0.01	0.001
Maximum Error	±1	±0.5	±0.05	±0.05

From these errors, we can establish a calculation of upper and lower bound for the stress calculated for a sample using these measurements. Previously measured stress will be compared to a range of potential erroneous stress values assuming error. This is considered the maximum possible error, assuming a worst-case error from all measurement sources. Incorporating the measurement errors from Table 1, the stress incorporating measurement errors are given as:

Equation 4-4:

$$s_{error} = \frac{P \pm E_{LC}}{(W \pm E_{DM})(T \pm E_{DM})}$$

where E_{LC} represents the error introduced in measuring by the load cell and E_{DM} represents the error introduced by some method of distance measurement (micrometer, optical microscope or SEM). Using this formulation of stress, we define the stress with maximum error incorporated as:

Equation 4-5:

$$s_{error,max} = \frac{P \pm E_{LC,max}}{(W \pm E_{DM.max})(T \pm E_{DM,max})}$$

Using this calculation provides an upper and lower bound for the values that would be expected for a measurement based on the equipment used.

For an example, a sample with a measured cross section of 500 μm x 500 μm under a measured load of 275 N would be subjected to a stress:

$$s = \frac{P}{A} = \frac{P}{(W)(T)} = \frac{275\ N}{(0.5\ mm)(0.5\ mm)} = 1100\ MPa$$

Now, incorporating measurement errors from the load cell and optical microscope, the upper and lower bound of stress measurement can be found by using the maximum load and minimum dimensional measurements for the upper bound and the minimum load and maximum dimensional measurements for the lower bound:

$$s_{error,upper} = \frac{P + E_{LC,max}}{(W - E_{DM.max})(T - E_{DM,max})} = \frac{275\ N + 0.05\ N}{(0.5\ mm - 0.0005\ mm)(0.5\ mm - 0.0005\ mm)} = 1102.4\ MPa$$

$$s_{error,lower} = \frac{P - E_{LC,max}}{(W + E_{DM.max})(T + E_{DM,max})} = \frac{275\ N - 0.05\ N}{(0.5\ mm + 0.0005\ mm)(0.5\ mm + 0.0005\ mm)} = 1097.6\ MPa$$

For the given example, the resulting error when comparing with the actual measured value is only ±0.2% for this worst-case scenario. The actual error that one would typically encounter using this measurement technique, assuming a normal distribution, will be closer to 0.1%.

Of course, as the size of the sample and load the sample experiences decreases, more error will be introduced by these measurement techniques. To demonstrate the maximum error more generally, the worst-case scenario calculation was performed for numerous sample dimensions and a range of load values. Thus, demonstrating the maximum error seen in the measurements of this study, which can be compared to the experimental scatter that has been observed. The results of these calculations are provided in Table 4-2.

Table 4-2: Calculation of Measurement Error in Theoretical Experiments

Sample Width (μm)	Sample Thickness (μm)	$E_{DM,max}$ (μm)	$E_{LC,max}$ (N)	Stress σ (MPa)	$s_{error,u}$ (MPa)	$s_{error,l}$ (MPa)	% max error
500	500	0.5	0.05	1100	1102.40	1097.60	0.22%
400	400	0.5	0.05	1063	1065.47	1059.54	0.28%
300	300	0.5	0.05	1056	1059.64	1051.49	0.39%
200	200	0.5	0.05	1000	1006.28	993.77	0.63%
200	200	0.5	0.05	900	905.77	894.27	0.64%
200	200	0.5	0.05	800	805.27	794.77	0.66%
100	100	0.05	0.05	1000	1006.01	994.01	0.60%
100	100	0.05	0.05	900	905.91	894.11	0.66%
100	100	0.05	0.05	800	805.81	794.21	0.73%
50	50	0.05	0.05	1000	1022.04	978.04	2.20%
50	50	0.05	0.05	760	781.56	738.52	2.84%
50	50	0.05	0.05	640	661.32	618.76	3.33%

The same analysis can be carried out for any of the actual experiments that have been reported. However, the range of the data presented in Table 4-2 covers the entire scope of all experiments in this study. The maximum error for the measurement techniques is below 1% for all samples 100 μm or larger and 3% for samples in the range of 50 um. These physical measurement inaccuracies correlate with less than 21 MPa error.

Similar to the stress error analysis, the inaccuracy in strain from DIC must also be considered. Errors in the strain measurements cause the 0.2% yield criteria to have some spread in the data. More specifically, when finding the elastic modulus with incorrect strain measurements, the slope of the elastic portion of the stress-strain curve will change. Thus, when extrapolating a line of the same slope through 0.2% strain to define the yield stress, it too will have some error.

As described earlier, a series of rigid body motion tests was performed to calculate a baseline strain associated with the software and equipment used. These rigid body motion tests were performed at three different actuator speeds of 20, 50 and 150 steps/s to determine if the speed has any effect on the amount of error. However, typical actuator speeds for the experiments were between 10 and 50 steps/s. The measured strain from the rigid motion tests is presented in Table 4-3.

Table 4-3: Results of Rigid Body Motion Strain Measurements

Actuator Speed (steps/s)	Actuator Speed (μm/s)	Average 1D Strain	Maximum DIC Calculated Strain
20	4	1.42×10^{-5}	7.6×10^{-5}
50	10	2.75×10^{-4}	5.0×10^{-4}
150	30	2.83×10^{-4}	5.7×10^{-4}

The average error calculated is small compared to the actual strains that are measured, especially at the levels of strain at which yielding occurs. There appears to be some effect from the speed at which the sample was displaced, however, the strain error remains low.

Additionally, the measured strain via DIC for the rigid body motion tests was compared with the strain measured through points at the ends of the sample gage section

as well as the interior of the gage. The average difference in strain for these two methods is reported for a subset of samples, sizes of 100, 200, 300, 400 and 500 μm, in Table 4-4. The results presented here represent an average of 3 tests of each of the sample sizes.

Table 4-4: Calculated Strain Difference With and Without Interior DIC Tracking Points

Nominal Sample Width/Thickness (μm)	Average Strain Difference	Average % Strain Difference	Corresponding Maximum Stress Error (MPa)
100	0.0018	1.13%	±9.9
200	0.0015	0.97%	±8.25
300	0.0017	0.96%	±9.35
400	0.0013	0.75%	±7.15
500	0.0019	0.473%	±10.45

There is a minimal effect from including the data from these interior tracking points such that all sample sizes showed about 1% or less error.

Lastly, the difference in time resolution from the load cell data acquisition and the image acquisition rate can produce potential errors. Images are only collected at a rate of 1 image/sec due to the time resolution of images and the time necessary for proper exposure with the camera. However, the load data is collected at a rate of 10 points/second to maximize the amount of data recorded. The MATLAB code used to run the DIC for this study, that is also used to calculate the 1D average strain, has post-processing options to stitch the stress and strain data using the recorded timestamps. Due to the difference in time resolution between stress (load) and strain (images), the error for matching data points is limited by the time resolution of the images. In a worst-case scenario, the stress-strain data could be stitched incorrectly within up to 10 load data points for a given image, based on the mismatch in time resolution. The tests from Table 4-4 were used to show the average load increment per data point, close to where yielding

is expected, and is given in Table 4-5. The 10-point average load variation is calculated and also given in the table with the corresponding maximum range that the stress can vary with respect to the resolution mismatch.

Table 4-5: Load Increment Per Data Point, 10 Point Data Averages and Corresponding Stress Error

Nominal Sample Width/Thickness (µm)	Average Load Increment/Point (N)	Average 10 Point Load Data Range (N)	Corresponding Maximum Stress Error (MPa)
100	0.0197	0.197	±9.7
200	0.0216	0.216	±2.7
300	0.0205	0.205	±1.1
400	0.0222	0.222	±0.7
500	0.0207	0.207	±0.4

Combining the DIC, physical measurements and the stitching resolution errors, finally the absolute maximum amount of error in the yield strength is determined. The total error for each sample size is presented in Table 4-6.

Table 4-6: Summary of Errors and Maximum Total Error

Measured Sample Width (um)	Measured Sample Thickness (um)	Measured Sample Load (N)	Calculated Stress (MPa)	Maximum % Error
500	500	275	1100	1.2%
400	400	170	1062.5	1.1%
300	300	95	1055.56	1.4%
200	200	40	1000	1.17%
200	200	36	900	1.9%
200	200	32	800	2.1%
100	100	10	1000	2.56%
100	100	9	900	2.84%
100	100	8	800	3.2%
50	50	2.5	1000	4.29%
50	50	1.9	760	5.6%
50	50	1.6	640	6.6%

The maximum total error, combining all sources, is 6.6%, which corresponds to a maximum error in stress of about 43 MPa. A comparison of the measured yield stress deviation to the error analysis is shown in Table 4-7.

Table 4-7: Comparison of Experimental data with Calculated Errors

Nominal Sample Width/Thickness (μm)	Experimental Yield Stress Scatter (MPa)	Maximum Error Spread (MPa)
500	34.7	13.25
400	57.8	10.85
300	43.2	14.35
200	202.5	17.23
100	286.7	25.61

It is clear that the variations in the experimental measurements is much greater, sometimes by an order of magnitude, than the error that would be introduced by the measurement methods.

4.4.3 Discussion and Conclusions from Error Analysis

The potential sources of error in the measurements are not large enough to account for the experimental scatter that is seen in the results. The larger sample sizes yield results that are very consistent and close to the reference bulk values with negligible measurement error. Across all length scales, the maximum error in measured yield strength is under 7%, showing the reliability of these larger sample measurements and confirming that the microstructure being sampled is the underlying factor for the scatter observed in mechanical properties.

Recall, the errors presented in this worst-case analysis for each sample size is based on the largest error for each potential source identified. Assuming the error has a normal distribution, the maximum expected error would be less than 5% for all sample sizes when considering the error within two standard deviations of the distribution.

There are improvements that can be made to minimize the error for future experiments. The accuracy of the load cell has a much greater effect on smaller samples because the error remains static while the sample dimensions used to calculate stress decrease, especially when yielding occurs at less than 10 N. For smaller samples, a load cell with better accuracy and resolution would reduce the error for measuring load, making it comparable to the larger samples. In addition, more work can be done with the setup for DIC to minimize error. The rigid body motion test showed an increase in error in strain measurement as the speed of the actuator increased. This could be a function of the subsets in DIC not tracking well with too large of a displacement being applied However, for quasistatic loading there are not large displacements between subsequent images. Nonetheless, acknowledging the aberrations for testing at higher strain rates and higher levels of strain in general is necessary. In addition, improvement of speckle patterns and lighting conditions for DIC can improve strain calculations because poorly tracked points in an image can cause errors in the raw displacement, which are later used to calculate strain.

The potential sources of error in the experiments to measure the strength of René 88DT at varying sample sizes have been identified, explained and analyzed to determine the effect that they have on the results. The experimental data shows more scatter as the sample size is decreased, which is expected to be linked to the increase in variations in microstructure of samples as the volume being sampled is decreased. However, due to the resolution of equipment, it can be expected that with decreasing sample size there is also the potential for more error in measurements. Quantifying the maximum effect of each source of error revealed that the experimental scatter was not due to these errors but is

truly an effect of the underlying microstructure. At the smaller sample sizes, the maximum potential error is not nearly significant enough to account for the variations in the data. Thus, there is confidence in the experimental measurements varying as a function of microstructure, which can be accurately used for benchmarking models.

4.5 Discussion

4.5.1 A Numerical Model of Size Effects in Polycrystalline FCC Volumes

It was expected that as the sample size decreases, the effect of microstructure will play more of a role in determining the strength, as compared to that for a bulk sample, where microstructural effects are averaged out. Although the downward trend in the data and the scatter matches well with the predicted variability of yield strength as a function of sample size, there was no observed increase in yield strength above the bulk value at any sample size. In order to understand this behavior in more detail, a numerical study was performed, in collaboration with George Weber et al. at Johns Hopkins University, in order to investigate the role of microstructure on yield strength as it scales with sample size [115]. This simple numerical study was based on Schmid factor analysis and conducted to gain insight into how finite sampling of grain orientation may affect the strength as a function of sample size. This is a qualitative approach since it ignores grain-to-grain interactions and the complex non-uniaxial loading states that may arise in individual grains [20].

For this estimate, cubic grains of a uniform size, such that distributions in grain size and shape did not play a role, represented the synthetic gage volume of a tensile sample. The sample was modeled to have a square cross-section and 5:1 aspect ratio as

can be seen in Figure 4-19 for the example of 3 grains through the sample width and thickness. Each grain within the gage was assigned a random orientation and its associated maximum Schmid factor was determined, with respect to the loading direction, defining the corresponding strength of that grain. The strength of a sample was given as follows. The individual strength of each cross section was first defined to be equal the strength of the grain with the lowest Schmid factor contained in that cross-section. Subsequently, the yield strength of the sample was defined using a weakest link approximation along the length of the gage. The strength of each cross-section was compared, and the overall sample strength was determined by the weakest cross section, assuming that yielding would initiate in that cross-section. This assumption of strength was made based on the uniaxial tensile loading that the sample is assumed to experience. In a row of grains loaded in tension serially, the grain that would be expected to deform first is the one with the highest Schmid factor. However, in a series of grains loaded in parallel, such as in a sample cross section, it would be expected that the grain with the lowest Schmid factor would determine the strength of the collection of grains. These two configurations are what is seen in the formation of the model microstructure and lead to how the sample yield strength is determined.

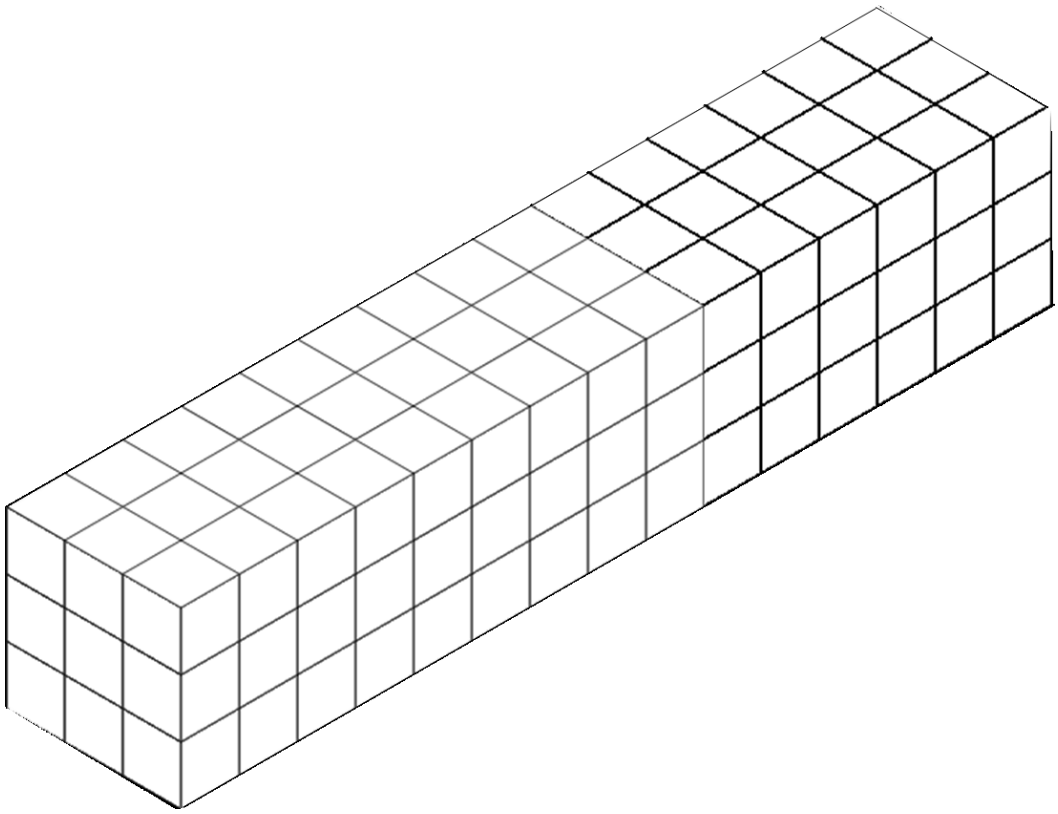

Figure 4-19: Example of representation of sample microstructure in numerical model, in this case with 3 grains through the sample thickness.

In developing this model, some interesting trends with regards to Schmid factor distributions in a randomly textured FCC material were observed. Figure 4-20 shows the probability density function (PDF) of Schmid factors for a randomly oriented grain in a face centered cubic (FCC) system under uniaxial tensile stress. This PDF was generated by randomly generating one million FCC grain orientations and calculating the Schmid factor of each. From Figure 4-20, it can be seen that there is a tendency for grains to have a relatively high Schmid factor in an FCC material with random texture as 50% of grains have a Schmid factor of 0.45 or higher.

Figure 4-21 shows this distribution of Schmid factors as a function of orientation on a Lambert azimuthal equal area projection of the standard triangle. From this plot, it can be seen that the distribution of Schmid factors in a randomly textured FCC microstructure is biased towards higher Schmid factors. Thus, in a randomly textured microstructure, there is low probability of finding a grain with a low Schmid factor that is resistant to deformation.

Due to the sample geometry, when there is one grain through the thickness, it is possible for the strength to be low. Even if a single grain along a cross section has a high Schmid factor, the weakest link assumption will ensure that the entire sample will have a lower overall strength. As the sample size increases, the probability of having stronger grains in the microstructure increases, resulting in increased sample strength approaching the bulk strength. Overall, it is unlikely that the sample strength will be increased, even as the volume is decreased because it is very unlikely to contain a series of grains oriented for low Schmid factor.

Analysis with this model was conducted for thousands of synthetic samples from as small as one grain through-thickness to up to 30 grains through-thickness. The distribution of normalized yield strengths was plotted against the normalized sample thickness for sample geometries of 1 grain through the cross section up to 30 grains through the cross section. The trend in this numerical study is strikingly similar to the trend observed in the experimental data as can be seen in Figure 4-22.

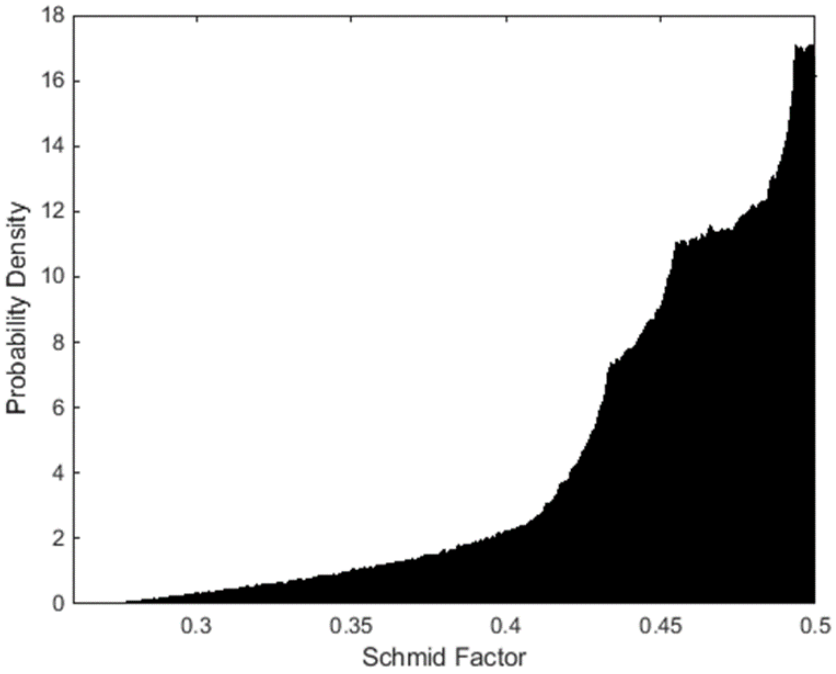

Figure 4-20: Probability density function of Schmid Factors in randomly oriented FCC grains.

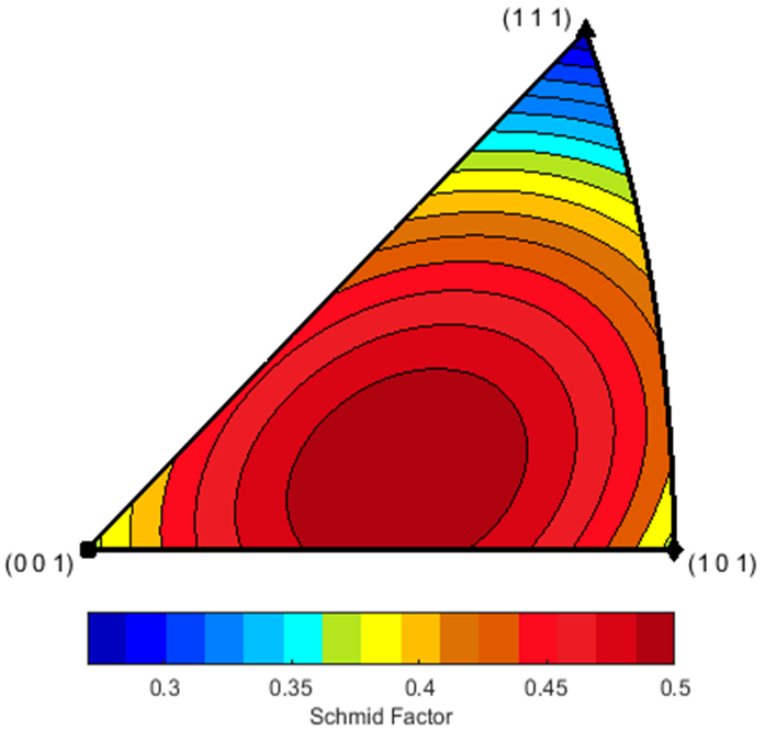

Figure 4-21: Equal area projection plot on stereographic triangle of maximum Schmid factor with respect to loading direction for FCC crystals. Note the bias towards larger values for Schmid factor.

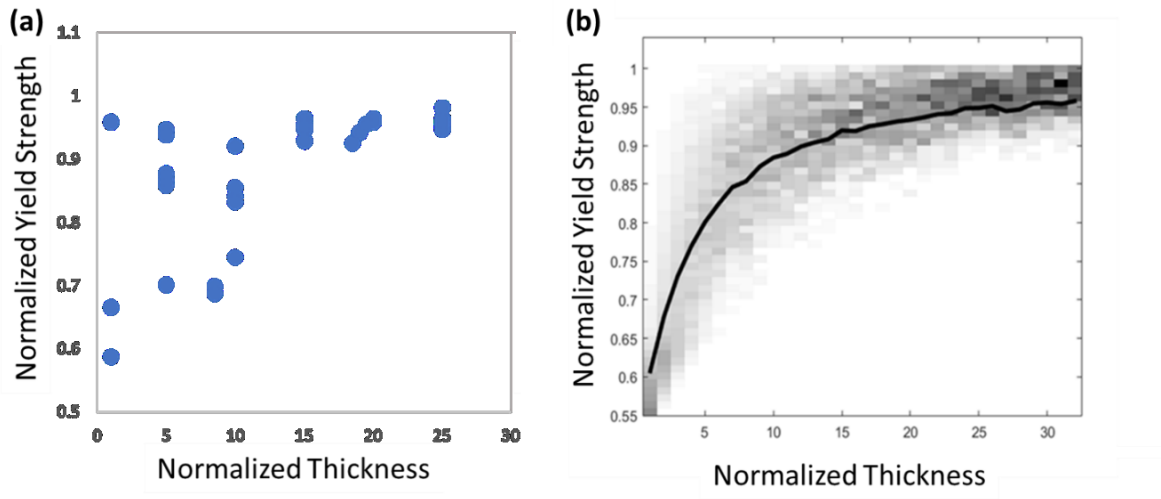

Figure 4-22: Comparison of (a) experimental data with (b) numerical simulation results.

Although this simple numerical analysis employs many assumptions and ignores the effects of load shedding, free surfaces, and grain size and shape, the qualitative influence of how the finite sampling of grain orientations leads to decreasing strength and large scatter as sample size decreases.

4.5.2 A Dislocation-mediated Crystal Plasticity Model of Size Effects in FCC Volumes

Building on the work done in the numerical study from 4.5.1, in collaboration with Yejun Gu et al. at Johns Hopkins University, a dislocation-based theoretical model was developed to further explore the trend of strength as a function of sample size with the role of microstructure. Unlike in the numerical model, three different cases were observed using this model using Al as a model material. The first case was single crystal samples (Figure 4-23), which were simulated to observe the effect of single crystal size on the critical resolved shear stress (CRSS). The second case was quasicrystal, or 2.5D, samples (Figure 4-24) having one grain through the sample thickness, but multiple grains

in both the width and length. For the quasicrystal samples, the yield strength was observed as a function of the normalized sample thickness based on the average grain size for the material. For both the single crystal and quasicrystal cases, the observed behavior matches the typically observed trend of smaller is stronger, with observed increases in strength as the single crystal thickness or thickness of the quasicrystal decreases. The third case represented in the model was polycrystalline samples (Figure 4-25), which had multiple grains in sample width, length and thickness. For this case, as with the quasicrystal case, the yield strength was observed as a function of the normalized sample thickness. However, in the polycrystalline case, the observed trend was that the average strength decreased and became more stochastic as the normalized thickness decreased, which is similar to what was observed in the René 88DT experimental data.

These polycrystalline simulation results have been performed using Al as a model material and therefore cannot be compared quantitively with the experimental results of the tested René 88DT samples. However, as these are both FCC materials, quantitatively the overall trend in the data matches well, as seen in Figure 4-26, and gives further credence to the microstructural effects resulting in this trend.

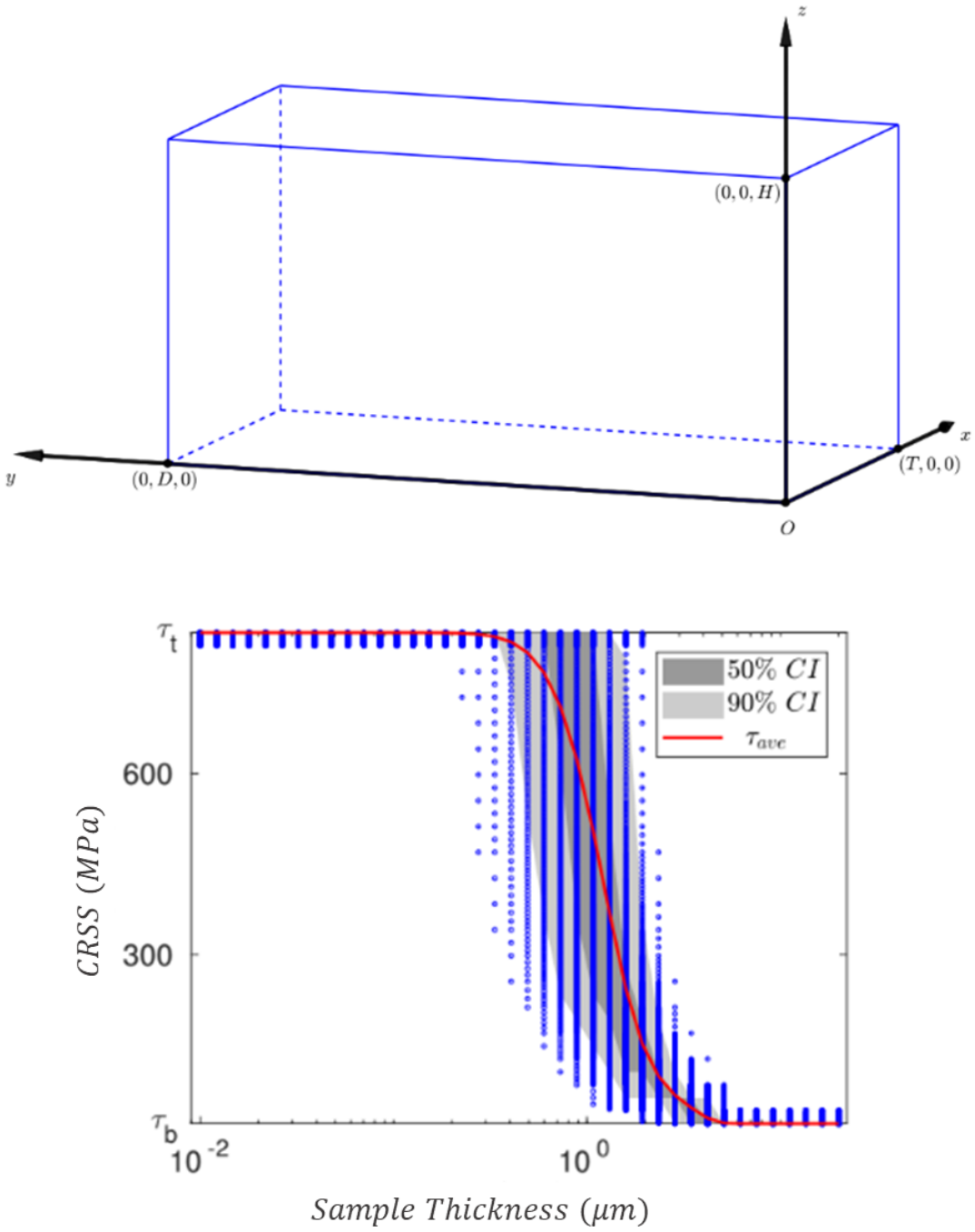

Figure 4-23: Representation of single crystal case in model and simulation results of CRSS vs sample thickness

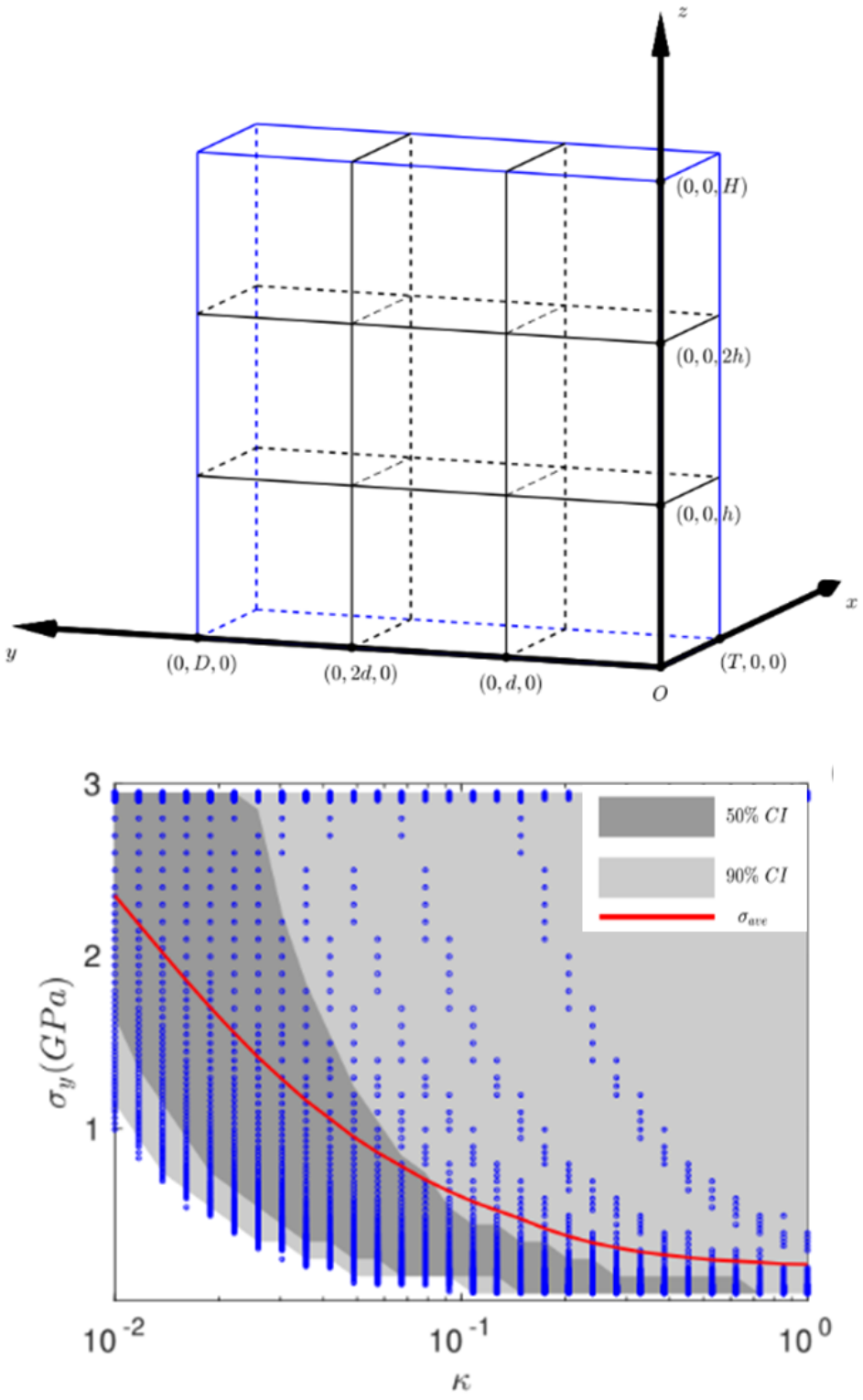

Figure 4-24: Representation of quasi-single crystal case in the model and simulation results of yield strength vs normalized sample thickness

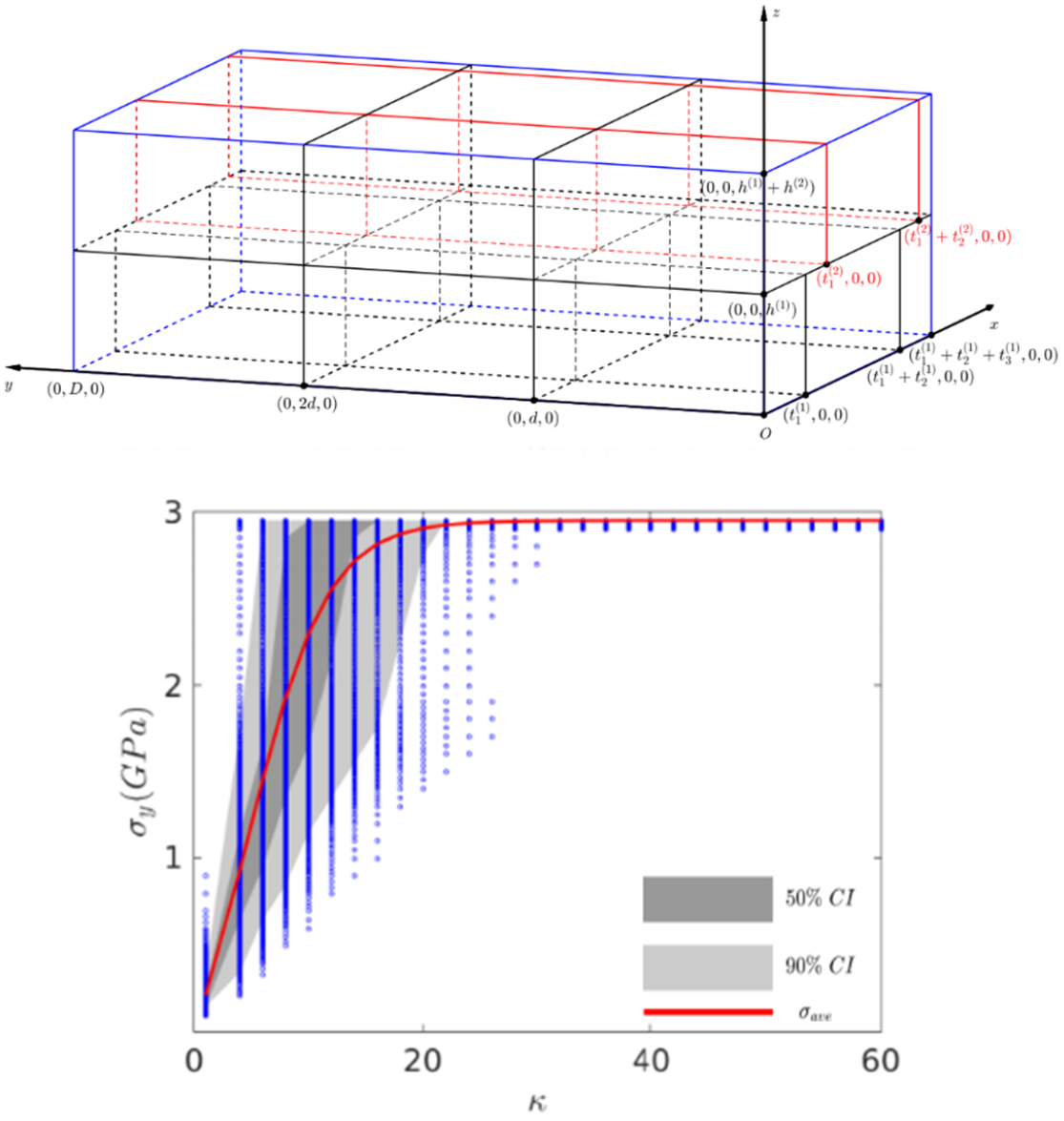

Figure 4-25: Representation of polycrystal case in the model and simulation results of yield strength vs normalized sample thickness

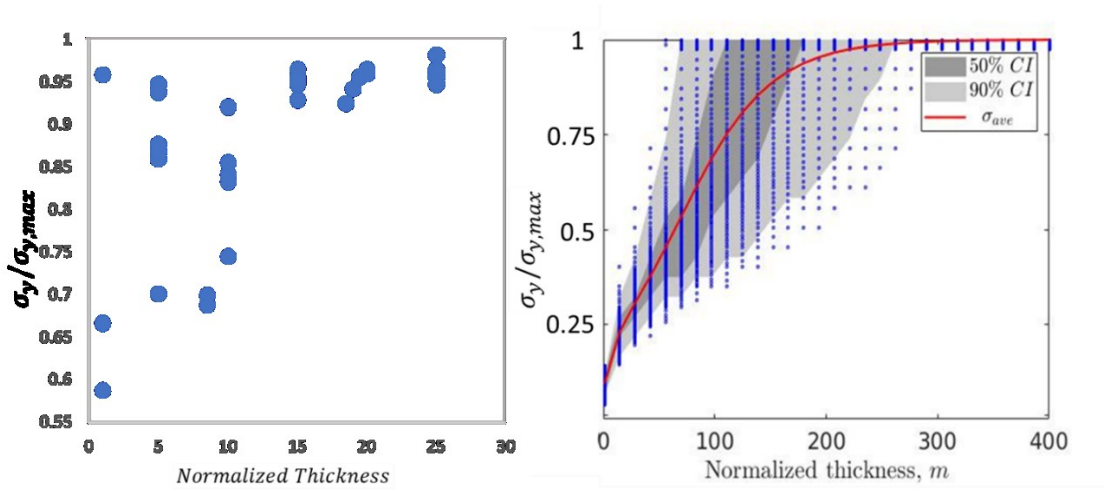

Figure 4-26: Comparison of experimental data with dislocation-based crystal plasticity simulation results.

The average strength decreases with sample size but the scatter in the mechanical response increases as the size decreases. However, intermediate sizes display a range of properties from bulk to much lower strengths for the same sample size. Alternatively, the quasi-single crystal and single crystal tests, which both have free surfaces, provide results consistent with the typical evidence that smaller is stronger with respect to sample size. At these sample sizes, the effect is driven by the need to nucleate a dislocation for deformation and the applied stress that is required to do so. The effects of subgrain microstructure at these length scales is an important factor in determining the strength of a sample, which explains the overall trend that sample strength increases with decreasing sample size as seen in Figure 4-26.

4.5.3 Comparisons with SERVE Results and Further Considerations

The previously described models of sample strength with size and the more statistical approach in the model developed with Gu, can provide a better path forward for both experimental testing and modeling efforts. By using this model developed by Gu

as compared to a full CPFEM simulation, computationally the convergence of an RVE can be determined very quickly for a material and could be used to provide more statistics than multiple iterations of a more computationally intensive code. Capturing this behavior with this model could give some insight into predicted experimental values before performing any mechanical testing, giving an idea of at what scale testing would need to be performed to capture either a bulk or mesoscale behavior.

Computational work done by Bagri et al. at Johns Hopkins University also provides insight into this experimental size-strength trend. A statistically equivalent representative volume element (SERVE) is a tool used as a part of the multi-scale modeling effort of René 88DT, which can be used to determine convergence of properties as a function of the size of a sample microstructural volume [165]. Although this tool is typically used in order to find a measurement of the proper size RVE needed for convergence of a property, it can also be used in a similar manner as to what has been done experimentally to observe the effect of sample size on strength. Starting from a larger SERVE size producing a bulk value for yield strength then decreasing the SERVE size, the trend in strength with size appears to again match well with what was seen experimentally. As the SERVE size decreases, there is greater scatter in the mechanical SERVE response, but the values of sample strength both increase and decrease.

This behavior is consistent with the initial predication; however, this is not observed in the experimental data or previous models where the sample strength was shown to only decrease at the polycrystalline scale. A plot of the yield strength results from SERVE simulations presented in [165] is shown in Figure 4-27.

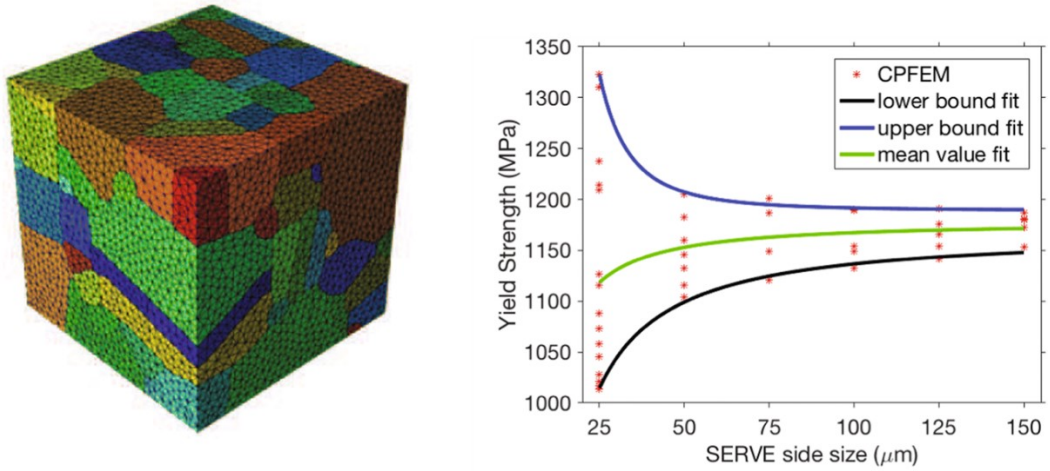

Figure 4-27: Example of SERVE geometry with 10 μm side length and plot of SERVE yield strength vs SERVE side size [165].

There seems to be a difference in the SERVE geometry as compared to the tested sample geometry, which may account for the differences. The SERVE geometry is a cube with equal dimensions on all sides, whereas the sample geometry has a rectangular shape in order to comply with ASTM tensile testing standards. As the sample size increases, the sampled microstructure is large enough to provide a bulk value and average out any microstructural effects. As the size is decreased, however, because of the weakest link effect and the lower probability of low Schmid factor grains being present in the sample volume, the geometry of the microtensile sample gives a lower strength than the cube geometry of the SERVE. The cube volume of a SERVE with a small sample size of 20 μm or less can capture the single crystal behavior, and thus, shows the full range of feasible single crystal strengths. Conversely, the microtensile geometry will still have multiple grains along the sample length, causing a higher probability of lower yield strength. In addition, the smaller sample volume exposes more grains in the microstructure as surface grains, and although this effect may be captured in the free

surface boundary condition of the SERVE, the area of surface grains is larger in the microtensile geometry.

These combined factors provide understanding for the discrepancy between the experimental results and SERVE predictions, even though the behavior observed is based on the same microstructure. It is also important to note that for the SERVE results, the overall trend in the sample yield strength still shows a decrease in strength with size, especially at smaller sample volumes. This further highlights the effect of a lower probability of a grain to be oriented for low Schmid factor in an FCC system. It would be prudent in the near future to run CPFEM simulations that more closely represent the microstructure of the full sample gage than a cube in order to compare more directly with the experimental results and the two other models described in this section.

4.6 Summary and Conclusions

An experimental methodology for machining and testing microtensile samples of Ni-base superalloy René 88DT across multiple length scales was developed with the intention of studying the effect of sample size on yield strength. The expectation was that sample microstructure would play a larger role at smaller sample sizes. The overall trend in the strength was found to decrease with sample size while increased scatter was observed as the sample size decreased. However, no tested sample exhibited greater strength than the bulk value for this material, which differed from the initial predictions of the sample strength. It was expected that both increasing and decreasing strength would be observed when decreasing sample size from the bulk value. To understand the trends seen in the experimental data and the predicted behavior, multiple simulations of increasing complexity were used to describe the effect. It was determined that the

distribution of Schmid factors for random orientation of grains in an FCC material is biased towards higher Schmid factors, owing to the decrease in sample strength as more of these grains influence the mechanical response of a sample. Additionally, both the reduced constraint [149] in surface grains and the finite sampling of grain orientations in small volumes are contributing factors. The geometry of the sample can also have an effect as seen in the difference between the trends of the SERVE data as compared to the experimental data and the results of the other two models discussed in this study. The results provide insight into the effects of polycrystalline microstructure on the mechanical properties of this material and a means of quantifying this behavior in a way that can inform selection of RVEs in multi-scale modeling. Further work should be done to compare more explicitly between experimental results and CPFEM simulations by running simulations of synthetic microstructures more accurately representing the geometry of tested samples.

Chapter 5: Mesoscale Testing and Characterization

5.1 Introduction

Being able to predict and model how the microstructure of materials affects their performance and how to tune the microstructure for future applications is an important area of study and one that is becoming increasingly more viable through linking of experimental results with multiscale computational models through the MGI and ICME [1]. Traditional methods for qualifying structural materials using bulk material testing provide a solid foundation but fail to capture the detailed underlying microstructural dependences that can now be included in high-fidelity multi-scale models. As such, development of multiscale crystal plasticity modeling is a challenging but important thrust area within the ICME paradigm. These multiscale deformation models depend on detailed characterization of microstructure and experimental benchmarks obtained at salient length scales [166]. These models can predict the development of intragranular gradients in the deformation field, as well as the evolution of grain morphology and local lattice rotations, but they have known limitations such as difficulty in accurately accounting for length scale effects. Experimental validation of such methods is critical to guide their further development and implementation; however, due to experimental and computational challenges, validation studies which compare experimental data to simulations that explicitly incorporate the experimental microstructure have historically been limited. One method for capturing information about the experimental microstructure is serial sectioning combined with EBSD mapping (3D-EBSD) [84, 85]. Microscale mechanical testing enables interrogation of test volumes that are appropriate

in a pragmatic sense for both 3D-EBSD characterization and developing benchmarks for modeling of the explicit structure [31]. The combination of all these techniques allows the collection of rich datasets for model development and validation.

While in the previous Chapter, experimental benchmarks and observed trends in size effects were investigated, this chapter will focus on efforts undertaken to perform detailed microstructural characterization of René 88DT samples in 2D and 3D. In addition, the use of 2D DIC will be demonstrated as a means of providing quantitative benchmarks in terms of local strain magnitudes, as well as qualitative benchmarks of where strain nucleates and accumulates within the microstructure. In addition, this strain data can be used to investigate microstructural properties that lead to the observed deformation behavior, thus serving as a key insight for further model and material development. While being able to capture properties such as yield strength, elastic modulus or strain to failure can be important benchmarks for modeling, it is the ability to capture these local, scale specific benchmarks and explicit microstructural details in a complex material, such as René 88DT, that sets apart these experimental efforts in ICME from work that has been done in the past.

5.2 Testing and Characterization of 20 μm Thick Samples

Initial testing for this study was carried out at the Air Force Research Lab in Dayton, OH on FIB-machined samples having a nominal gage thickness and width of 20 μm. The selection of this sample size was made based upon the desire to capture an explicit polycrystalline volume within the sample gage within the limitations of sample size that can reasonably be manufactured with the FIB. In addition, the attocube

positioning system for the in SEM microtensile frame had a load capacity of 0.5 N, which was also a limiting factor in tested sample size. Although this sample size was close to the average grain size of the material, ostensibly there would still be several grains spanning the gage cross section which was desired to avoid sampling individual grains in a single crystal mechanical response.

As previously described in Chapter 3, sample fabrication was carried out using a femtosecond laser for bulk machining followed by an automated FIB machining procedure to achieve the final 20 sample geometry. The same mechanical testing performed using the AFRL in situ load frame as part of the study presented in Chapter 4 was used to produce the results that will be presented in this Chapter.

5.2.1 2D Digital Image Correlation

Whereas determination of the stress-strain response of tested samples in Chapter 4 relied only on the use of 1D DIC, the distribution of local surface strains is a direct output of CPFEM and is also measurable experimentally through the use of 2D DIC surface strain mapping. This technique allows for the observation of strain localizations on the sample surface, which can provide insight to microstructural features that govern deformation in a sample and can also be used as an explicit benchmark when compared with CPFEM simulation results.

As described in Chapter 4, the procedure for performing DIC on the FIB samples included tracking of circular markers, machined into the sample surface using the FIB, from image to image using an image processing and a gaussian peak finding algorithm. From these marker positions, location specific displacements and therefore strains can be calculated. However, whereas the determination of 1D average linear strain as performed

in Chapter 4 is relatively straightforward, the calculation of 2D local strains is more involved. In this study, a method was followed similar to that described by Biery et al [167] in calculating strains using images taken in an SEM. Although the application of markers and tracking to determine their positions from image to image was different, once the marker positions are recorded, the calculation follows in the same way presented by equations 1-3 of [167]. First, a reference image of the sample before testing is taken and the marker positions from that image are recorded. Then, in each image taken during testing the marker positions are also determined using the same methodology presented in Chapter 4. A polynomial fit is used to map the coordinates of a central point and its neighbors in the reference image to those in the distorted image. From the polynomial fit, the strains can be determined by taking the derivative of this fit either with respect to deformation on the X or Y axis of the sample to determine the normal strains in both axes or with respect to both X and Y in order to determine the shear strains. Once this calculation is complete for all markers in an image, the marker coordinates can be associated with a calculated strain and from this data, contour plots of the strain can be created. This method is analogous to generating strain maps by tracking subsets of speckles on the sample surface in that this technique tracks explicit points on the sample surface instead. As such, the 1 μm spacing would provide similar resolution to a subset size of 2 x 2 μm with a step size of 1 μm.

5.2.2 3D Characterization via UCSB Tribeam

A 3D dataset of one of the tested samples was collected by Will Lenthe at UCSB through destructive sectioning and EBSD data collection using the TriBeam system [89]. The intention was to utilize this dataset and the attendant mechanical behavior and strain

captured from digital image correlation as an explicit benchmark for the CPFEM model being developed. The sample was sectioned into 250 nm thick slices by scanning a femtosecond laser parallel to the SEM imaging plane at 40 mW. After each cut with the laser, the surface was cleaned with a 30 kV, 15 nA Ga+ FIB at a glancing angle of 3°. A total of 33 EBSD scans were collected during the sectioning process with an in-plane resolution of 250 nm x 250 nm, resulting in a voxel size of 250 nm^3 in the 3D reconstruction. Reconstruction and analysis of the EBSD data was performed using DREAM.3D [168]. The EBSD scans were first stacked with a 180° rotation about [010] applied to the sample reference frame and a 90° rotation about the [001] to the orientation reference frame to account for manufacturer orientation definitions. A threshold of 0.1 on confidence index and 120 on image quality was applied to remove poorly indexed voxels. The slices were subsequently aligned along the sectioning direction by maximizing voxels within a 5° disorientation angle tolerance relative to the previous slice. Grains were defined in the aligned dataset using a 5° segmentation tolerance with grains smaller than 16 voxels removed by isotropically dilating their neighbors. The final digital reconstruction was composed of 3 million 250 nm^3 voxels and contained 286 grains. An image of the reconstruction can be seen in Figure 5-1.

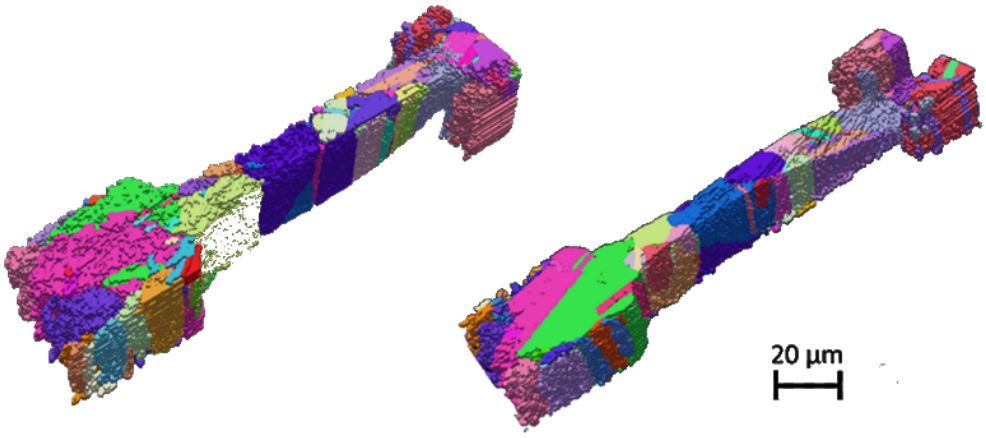

Figure 5-1: 3D microstructure reconstruction of René 88DT microsample with gage cross section of 20 x 20 µm. Each grain is colored according to its orientation.

5.2.3 Results and Discussion

For the three 20 µm samples tested as part of the study presented in Chapter 4, 2D strain maps were created using images captured during testing. Figure 5-2 presents strain maps for the three tested samples taken at the point of maximum strain during the test. With limited images being taken during testing, most strain activity that could be observed from mapping occurred at the point of maximum strain, which is also a reason why larger samples were eventually tested. These samples were not tested to complete failure in order to preserve the samples for further characterization after testing.

The local strain tends to concentrate in select regions as is expected in such small microstructural volumes [31, 87] and in this case, within just a few grains of the tested samples. In addition, the strain map data was correlated with the EBSD data captured for samples B and C. These results are presented for sample B in Figure 5-3 and sample C in Figure 5-4.

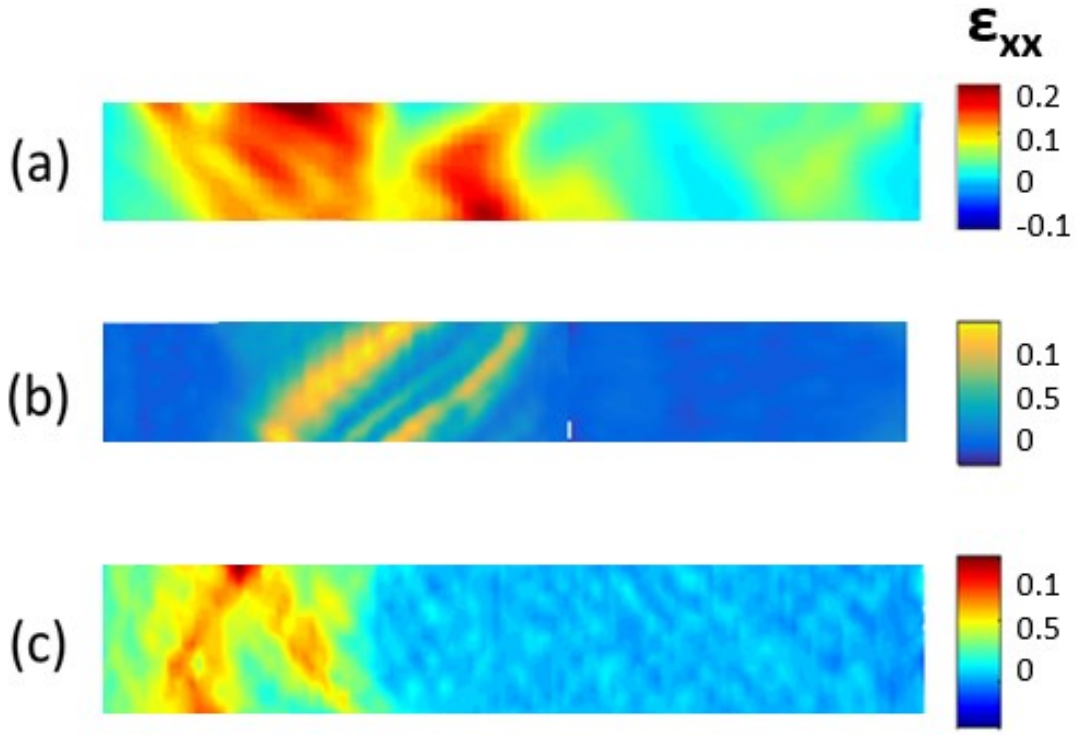

Figure 5-2: Images of local axial strain plots for samples deformed to (A) 7.0, (B) 3.5, and (C) 1.7% axial strain.

As seen in Figures 5-2 and 5-3, and the reconstruction of Figure 5-1, most of the strain in these samples was concentrated in a few grains. In addition, although the Schmid factor in the grains with strain concentrations appears relatively high between 0.45 and 0.5, there are other grains present in the sample with higher Schmid factors. In addition, as seen in Figure 5-1, for Sample B the grain where strain is concentrated spans the gage width and thickness, and for Sample C there is unfortunately EBSD data missing from a grain in the neighborhood of the strain concentration. Also, from the stress-strain curves for these samples presented in Chapter 4 (Figure 4-17), the mechanical behavior for these two samples showed a strain burst, a behavior more indicative of a single crystal test As a result, it is difficult to discern whether the geometric effect of free surfaces in the grains played a role, and if a true polycrystalline behavior was observed.

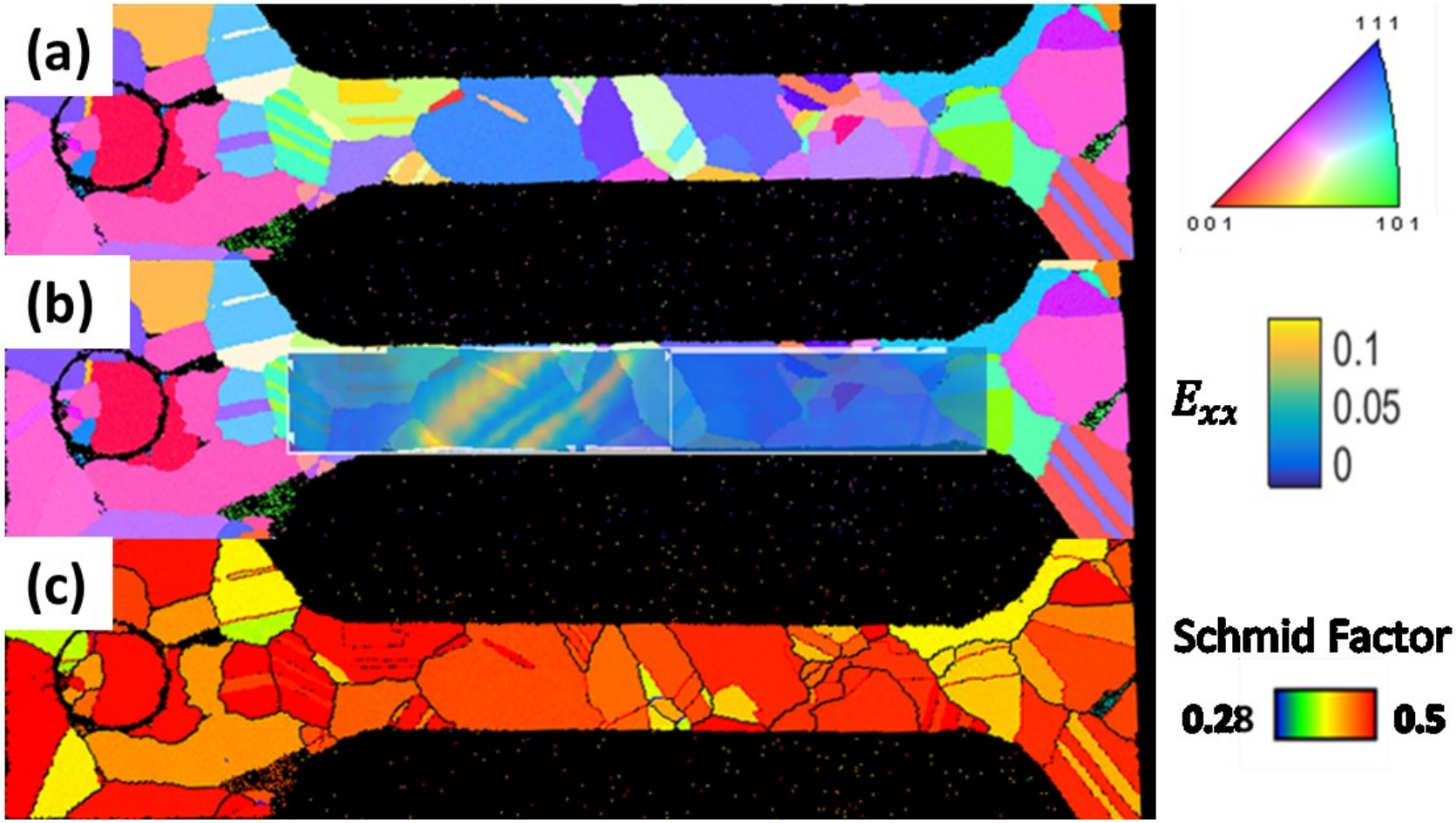

Figure 5-3: (a) Surface microstructure from EBSD for Sample B without and (b) with strain map from Figure 5-2b overlaid. (c) shows a Schmid factor map for this sample.

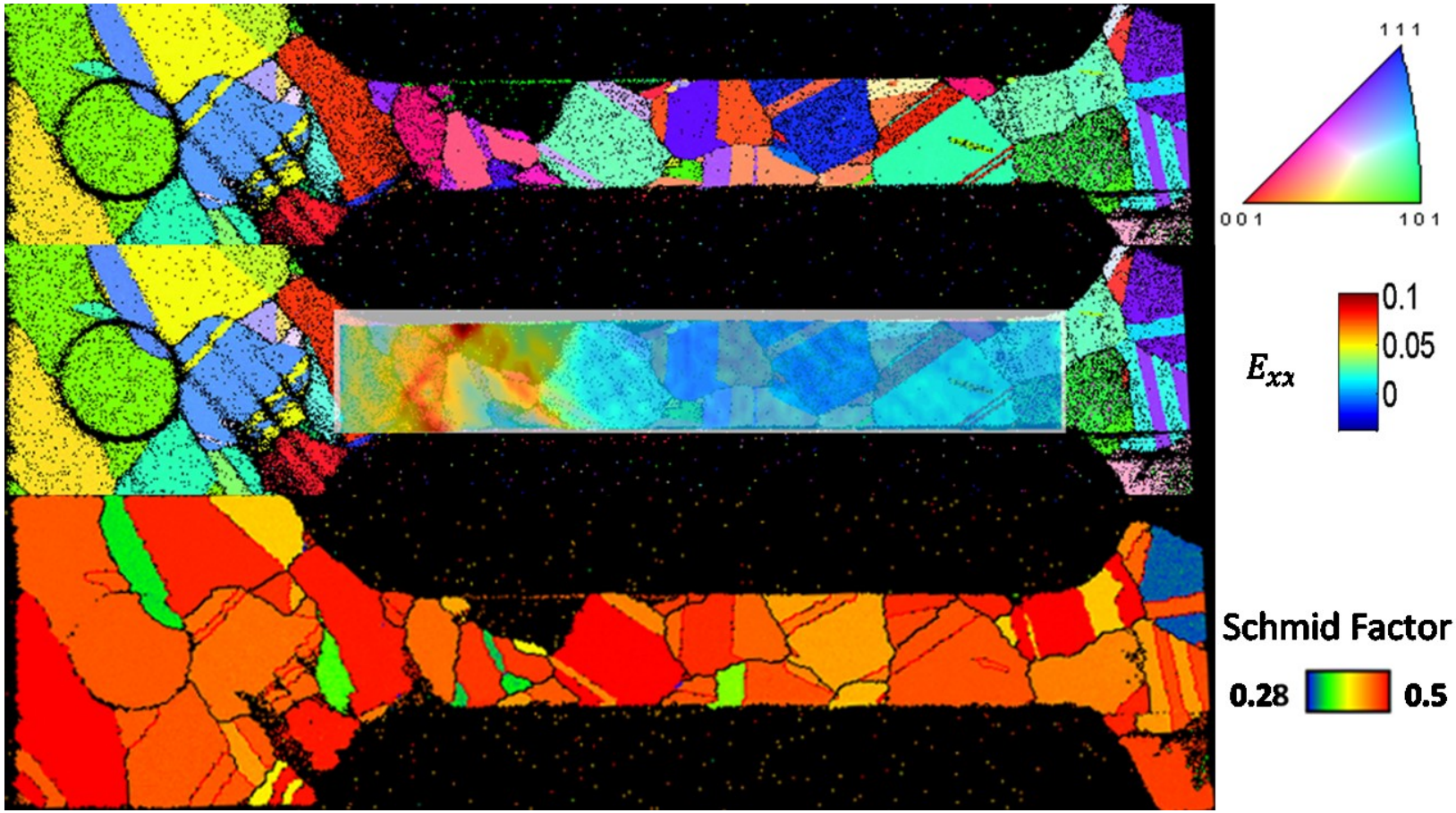

Figure 5-4: (a) Surface microstructure from EBSD for Sample C without and (b) with strain map from Figure 5-2b overlaid. (c) shows a Schmid factor map for this sample.

Another item to note with regards to the 3D reconstruction in Figure 5-1 is that a small volume of the sample is missing from the gage section on the right side of the reconstruction. This is an artifact of the laser machining process resulting from accumulating damage introduced to the sectioning surface during laser milling. Sectioning with the femtosecond laser produces a slight amount of beveling at the sample edge. In order to avoid having this beveling affect the EBSD scans taken in the gage section, the samples were sectioned along the length of the sample so that the beveling would only affect EBSD data in the grip section of the sample. However, along the length of the sample it is more difficult to keep the laser in focus for sectioning, and when the sample is only a few layers thick, it can be difficult to accurately place the beam if the sample starts to bend, resulting in the loss of data as seen in this dataset.

A few attempts were made to develop processes for preventing this kind of damage in future 3D-EBSD experiments. One technique that was tested was electroplating the samples with Ni to create a protective metallic coating on the surface that would also help the sample to maintain its structure during laser sectioning. However, due to the samples being fragile not only because of their size, but also because of the plastic deformation the samples had already undergone, the application of this coating further damaged the samples, rendering them unsuitable for further characterization with any accuracy.

Seeing the drawback of using electroplating, a more robust technique for protecting samples during sectioning was developed. The main issue with the electroplating technique was that it did not provide enough support for the fragile samples, so in the next attempt, samples were sandwiched between two 0.012” thick steel

plates using a conductive epoxy. Not only did this technique allow for easier handling of small test samples, but it also allowed the structure to maintain its rigidity even once the sample gage had been fully sectioned, unlike when a freestanding sample is sectioned, and it became difficult to image and characterize the thin foil that remained and was eventually destroyed in the last steps of the serial sectioning. Figure 5-5 shows a cross section of the sandwich structure after being partially sectioned using the femtosecond laser. It is clear that despite a thicker overall cross section to be ablated, the femtosecond laser is still a rapid sectioning process that doesn't create a bottleneck in the overall workflow. Although only a small section of a sample was able to be characterized as seen in Figure 5-6 before an unrelated vacuum failure occurred while testing this methodology. However, this dataset does prove that slicing can be performed through the sample thickness as opposed to along the sample length as had been done before without incurring any laser machining artifacts. This is a promising result for future applications to this technique for 3D characterization of freestanding samples. In addition, investigating this collected data with modeling collaborators helped to decide that a gage width and thickness of 50-75 μm was the ideal size for testing mesoscale samples within the limit of what could be modeled explicitly.

In addition to the difficulty in sectioning and 3D-EBSD characterization of these 20 μm samples, the results generated from these earlier tests indicated a need to test a larger gage volume to avoid some of the geometrical effects that we were seeing from not having multiple grains spanning the sample cross section. As such, the laser machining technique and sample geometry presented in previous chapters was applied to machine samples having a gage thickness and width ranging from 50-100 μm. The results and

observations from testing and characterization of these samples is presented in the next section.

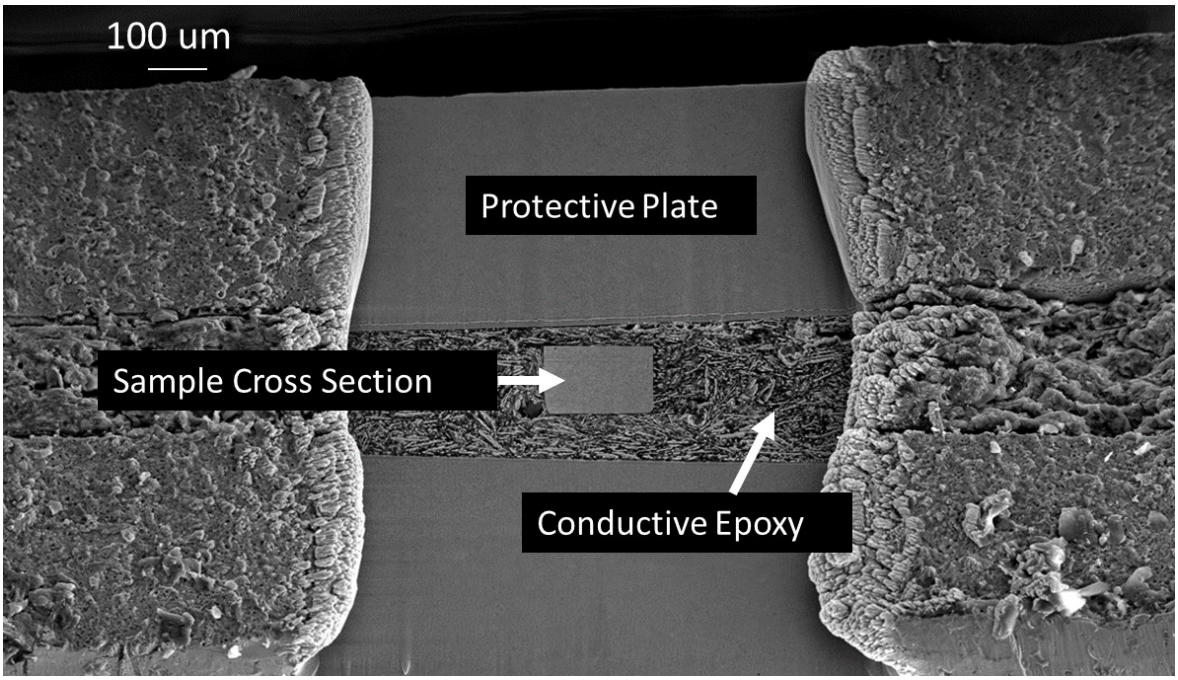

Figure 5-5: Cross section of sandwiched sample structure after preliminary sectioning by laser ablation.

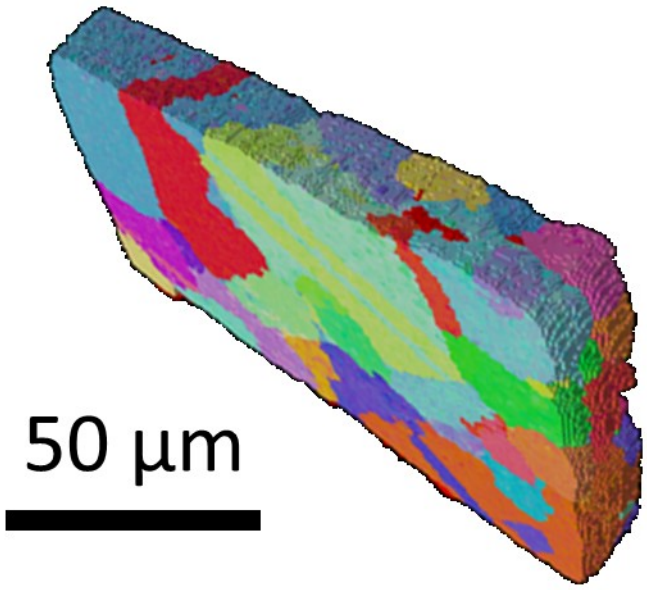

Figure 5-6: Preliminary 3D reconstruction of sandwiched sample from Figure 5-5.

5.3 Ex Situ Testing and Characterization of Mesoscale Samples

It was determined that the geometry of FIB machined samples was too small to be able to reliably capture a true polycrystalline response in the tested samples. With the geometric effect of one grain dominating the response, as well as the observation of rapid slip events more indicative of a single crystal test, it was apparent that a sample geometry ensuring multiple grains across the gage cross section was required. To this end, the femtosecond laser machining technique and mesoscale sample test methodology were developed. This section will discuss the characterization of the samples both in observations of the microstructure and DIC results, as was done with the FIB machined samples, and discuss the insights gained.

5.3.1 Microstructure Characterization

Prior to testing, mesoscale samples were characterized using EBSD in order to observe the microstructure in the sample. After fabrication via femtosecond laser machining, samples were delicately cleaned using isopropyl alcohol (IPA) in order to remove redeposited material. Then, samples were gently polished for about 30 minutes using a colloidal alumina solution in an automated vibratory polisher. This process removed remaining excess material on the sample surface and assured that the surface was polished to a high enough quality to perform EBSD on.

Samples were individually mounted to SEM stubs by attaching one grip end of the sample using carbon tape and then oriented in the SEM at an angle of 70 degrees using an angled SEM holder. EBSD scans were taken of one surface of the sample using a step size of 0.5 μm, which would also be the surface of the sample observed during microtensile testing. The scans were taken of the sample gage section, as well as an area

extending about 50 μm into the grips on both sides in order to capture grains that could play an important role in defining boundary conditions relevant to modeling.

This information was combined with the orientation information obtained from EBSD in order to observe what features in the microstructure were present where strain began to develop in the sample and which grains eventually yielded during plastic deformation. Further insights were gained by determining the Schmid Factor and elastic modulus of each grain in the EBSD map using the TSL OIM software.

5.3.2 2D Digital Image Correlation

Following EBSD characterization, samples were patterned for digital image correlation by applying a 1:10 solution of deagglomerated 50 nm diameter alumina particles in methanol to the sample surface and subsequently spinning the sample at 200 rpm while the solution dried on the sample to ensure that the particles were evenly distributed on the surface.

As discussed more thoroughly in Chapter 4, samples were tested quasistatically by pulling at a strain rate of 10^{-4}/s and images of the speckled sample surfaces were captured once every second during loading. 2D digital image correlation was performed using VIC2D to analyze the captured images to develop 2D strain maps. By observing maps of the strain on the sample surfaces, the nucleation and propagation of strain in the samples was captured and correlated with surface orientation maps to identify what microstructural features led to the observed mechanical behavior.

5.3.3 Results

An example of the evolution of strain observed through 2D digital image correlation is seen for a 50 x 50 μm cross section sample in Figure 5-7. The strain being

shown on this map is the local axial strain in the loading direction. In the uniaxial tension loading condition, use of axial strain is ideal for measuring local deformation. The images used to develop these strain maps were selected as snapshots to demonstrate how the strain in the sample first starts to nucleate and then eventually concentrates in one location in the sample as the sample approaches the maximum global strain that it experiences during the test. The global strain that the sample is experiencing is labeled at the corner of each image to give an idea of how far into the test the image was taken as well as to give an idea of how much greater the strain experienced by the samples at these local hotspots is compared to the overall strain the sample is experiencing during the test. For example, in the sample being shown in Figure 5-7, the local strain experienced at the strain hotspot at the center of the sample indicated on the strain map by the red coloring experiences a strain more than twice as much as that of the global strain of the sample. This behavior demonstrates the heterogenous distribution of strain seen at the grain scale in this material that can also be observed in CPFEM simulations.

To further look at deformation behavior in these samples, these strain maps were correlated with the orientation information obtained from EBSD to investigate microstructural features that lead to deformation in the sample. A summary of results for the sample shown in Figure 5-7 is shown in Figure 5-8. Starting from the top of Figure 5-8 and working down, what is being presented for this sample are: (a) a 2D map of the surface orientation data collected from EBSD with each grain and twin colored according to its out of plane orientation, (b) a 2D map of the orientation data collected from EBSD with each grain and twin colored according to its Schmid Factor calculated based on the sample loading direction, (c) a 2D map of the orientation data collected from EBSD with

each grain and twin colored according to its Elastic Modulus calculated from the sample loading direction and stiffness constants of the material and (d) an overlay of the 2D strain map from Figure 5-7 developed from VIC2D on an outline of the grain boundaries at the sample surface also made from the EBSD orientation data. Each of the maps is accompanied by a scale bar corresponding to the information being plotted on the map.

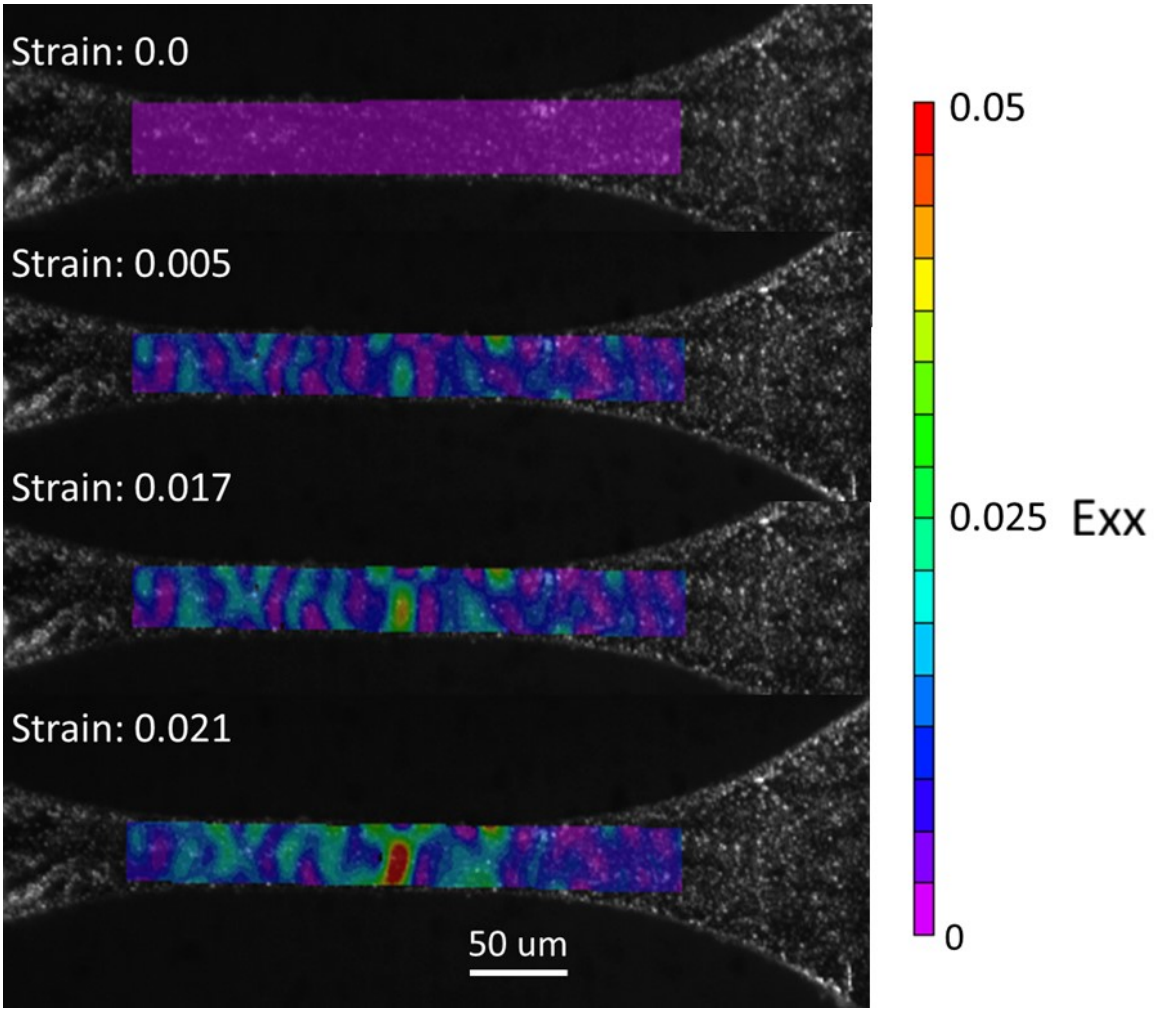

Figure 5-7: Progression of surface strain in microsample of René 88 at different levels of global strain.

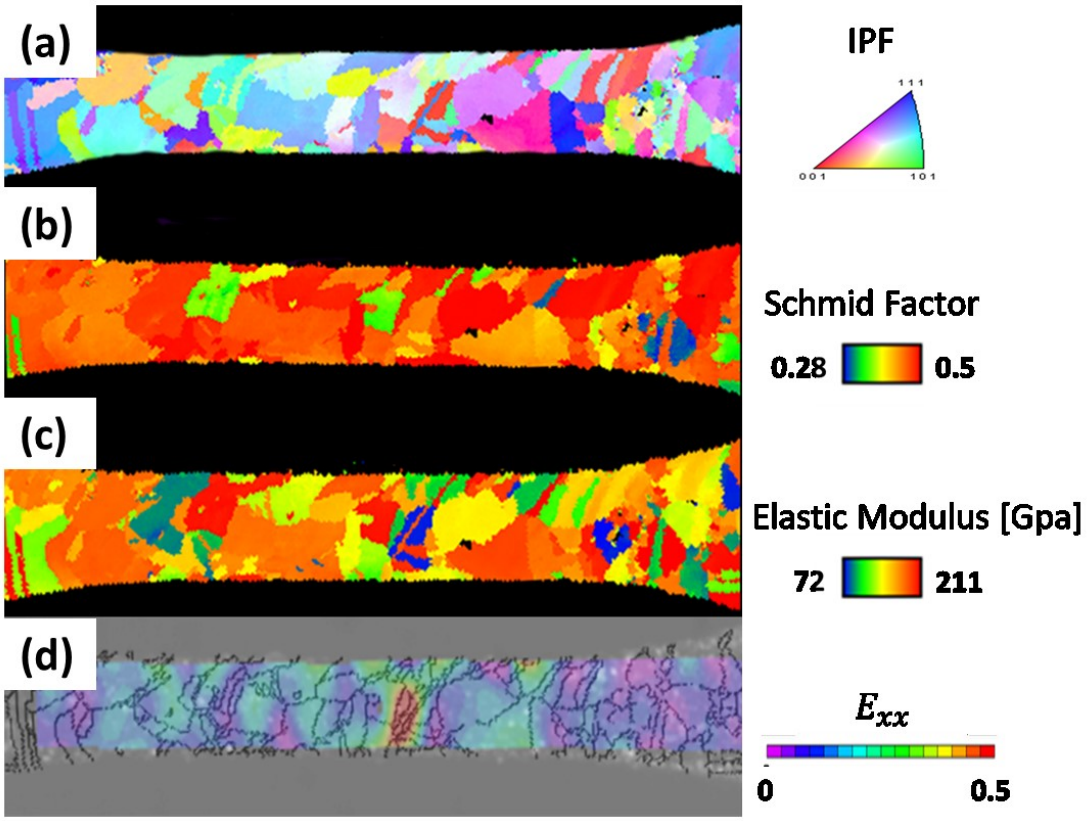

Figure 5-8: Surface images of a 50 x 50 μm tested microsample showing: (a) grain orientation using standard IPF coloring for FCC, (b) Maximum Schmid factor for each grain based on orientation loading direction, (c) elastic stiffness of each grain based on orientation and loading direction, and (d) surface strain map overlaid on grain outline.

5.3.3 Discussion

5.3.3.1 Microstructural Features Influencing Deformation

Looking at the information presented in Figure 5-8, it can be seen where in the microstructure of the sample the strain concentration is forming. In this sample the strain hotspot formed in the grain at the center of the sample that is denoted by a blue color in the elastic modulus map. This indicates that this portion of the sample has a relatively low elastic modulus with respect to how the sample is being loaded. In observing the Schmid Factor and elastic modulus of this grain, it exhibits a relatively high Schmid Factor of 0.45 (greater than 60% of grains within the sample) and low elastic modulus of

72 GPa (less than 95% of grains within the sample). The high Schmid factor seems to indicate that this grain independently would be more inclined for deformation than most other grains contained within the sample. However, this is not the grain with the highest observed Schmid factor and within a neighborhood of grains, simply looking at these individual grain characteristics alone is not be the only means of attempting to identify factors that lead to strain localization as grains exhibit load sharing or load shedding with their neighbors [90, 169, 170].

Looking further at Figure 5-8, it can be seen that in the region of the sample to the left of the strain concentration is a grain exhibiting both a low Schmid Factor of 0.3 and a high elastic modulus of 210 GPa, the opposite characteristics from the grain in which a strain concentration is observed. In addition, the twins of this parent grain also exhibit this elastic mismatch. In studies investigating the fatigue behavior of René 88DT by Stinville et al. [67, 90, 171] and Alam et al [169], it was seen that crack nucleation occurred in twins in which there was a high Schmid Factor and a mismatch in elastic modulus between the twin and the parent grain. These characteristics led to a stress concentration in the microstructure, leading to the formation and propagation of a crack. In a similar way, the mismatch between the Schmid Factors and elastic moduli of these two neighboring grains, as well as between the parent grain and twins in this sample is favorable to generate a stress concentration as well, that is exhibited by a high local strain accumulated in the grain oriented favorably for deformation.

Figure 5-9 presents data collected for slightly larger sample (75 x 75 μm gage cross-section) in a similar manner to the sample that was shown in Figure 5-8.

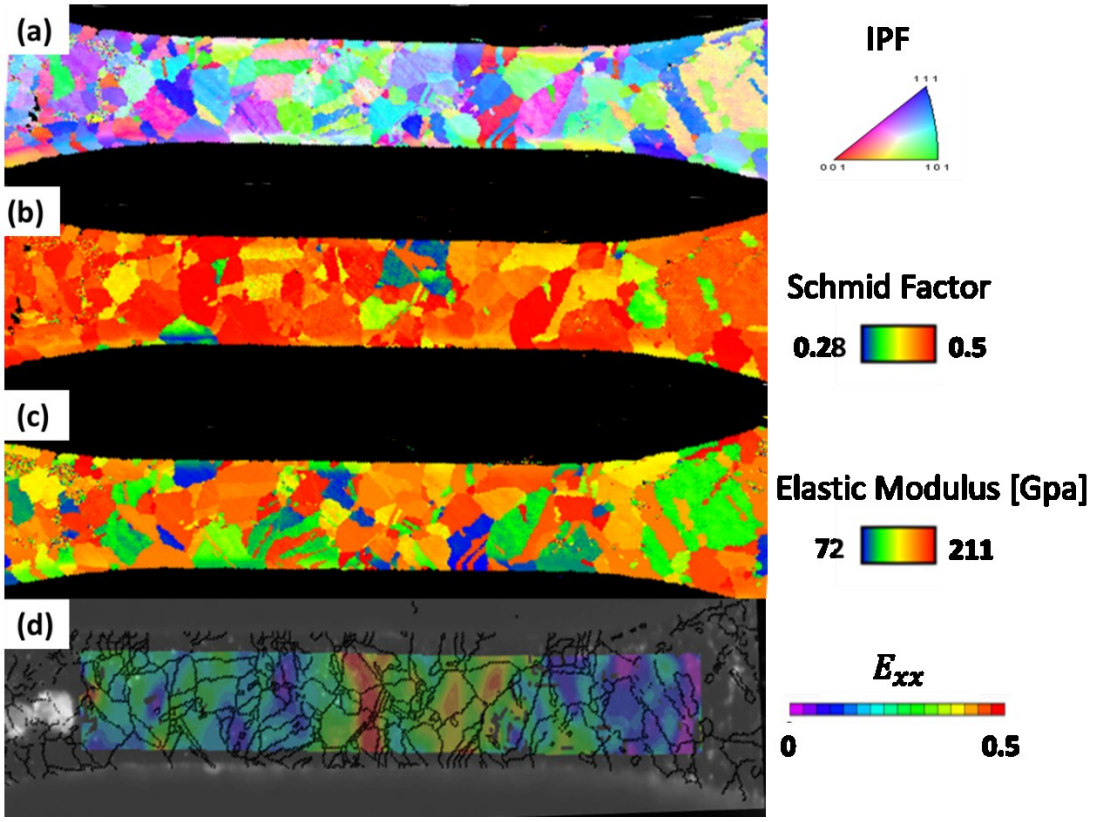

Figure 5-9: Surface images of a 75 x 75 μm tested microsample showing: (a) grain orientation using standard IPF coloring for FCC, (b) Maximum Schmid factor for each grain based on orientation loading direction, (c) elastic stiffness of each grain based on orientation and loading direction, and (d) surface strain map overlaid on grain outline.

The surface orientation data from EBSD, maps of the calculated values of Schmid Factor and elastic modulus as the 2D surface strain map overlaid on a grain boundary map are presented. In this sample, the concentration of strain manifests itself as a band across the width of the sample as compared to being contained within a single grain as had been seen in Figure 5-9. Close inspection shows that the same microstructural features that led to a strain concentration in the prior sample are also present in this sample as well. In this sample, grains in the vicinity of the strain concentration exhibit mismatches in both Schmid Factor and elastic modulus. In observing Figure 5-9b, there was a strong concentration of grains in the center of the sample having a low Schmid

Factor that is not seen elsewhere in the sample. In addition, these grains have a high elastic modulus and are neighbored on both sides by grains having high Schmid Factors and relatively low elastic moduli with respect to the loading condition. In addition, in the vicinity of the stress concentration, we can also see that there are grains present having high Schmid factor and a large mismatch in elastic modulus between the parent grain and the twins contained within which were seen in the previous sample as well as in the fatigue studies. In addition, there are other smaller strain hotspots that can be seen in right side of the sample in Figure 5-9d. It appears that for these three hotspots, two occur at interfaces between grains showing large mismatches in elastic moduli and one occurs within a grain showing a mismatch between the parent grain and twins. Each of these hotspots appears to occur at a location in which a stress concentration would be expected based on the microstructure. Although this sample did not have a specific grain in which the strain was concentrated, the same microstructural features near the strain concentration are seen in both of these cases, as well as in eight other samples, including the sample in Figure 5-8, tested and characterized in this manner as part of this study.

5.3.3.2 Connecting Experiments and Modeling

The combination of 2D surface strain mapping and microstructural characterization is a powerful tool for benchmarking microstructurally dependent models. Having the 3D dataset available as an input for a simulation and then being able to map strain concentrations within samples containing various microstructures is a significant step from simply comparing the predicted mechanical response of the tested samples with the global mechanical behavior of tested samples. Having information about where in the sample the strain begins to accumulate in the early stages of plasticity and subsequently

being able to track its evolution to the point of maximum strain provides a direct comparison to CPFEM output of strain at the grain level of the microstructure. The imaging capability of the technique used within this study provides less resolution than DIC performed with imaging in the SEM, but the acquisition rate of 1 image per second is much faster and allows for collection of more strain data to be used in developing maps to show the evolution of strain in the sample during the course of a test. In addition, the ability to capture microstructural information to correlate with strain mapping and to understand what features lead to local strain concentrations not only allows for direct comparisons with modeling predictions, but also provides insight for further development of models to make sure that appropriate mechanisms are included in CPFEM models.

While microstructural features that can be observed at the surface of these samples provide indication of where in the sample surface deformation occurs, there is still a lot of microstructural information from the entire sample volume that is inaccessible by this technique alone. In order to fully be able to understand the effect of microstructure on the behavior of tested samples and have a true explicit benchmark, full 3D characterization of tested samples is necessary. The subsurface grains can significantly affect the observations made at the sample surface. In a study performed to test microtensile samples of pure Ni and characterize them in 3D, it was found that measurements made at the sample surface could change significantly depending on the structure of grains below the surface that could not be observed with traditional EBSD [87, 88].

Based on the orientation data seen in Figures 5-8 and 5-9, it is clear that a true polycrystalline representation of the microstructure is being captured, and from

discussions with collaborators modeling this material, the number of grains and twins being captured in the gage volume is still less than 1,000 total, which is small enough to be able to mesh and simulate explicitly. Figure 5-11 gives an idea of how a 3D digital microstructure could be used to instantiate a CPFEM simulation. The digital data collected from an experiment has to be properly segmented in order to identify grains and twins in the microstructure. Then, each of these features must be assigned properties based on their orientation. Finally, a mesh can be developed in order to model the microstructure using the CPFE method.

5.3.3.3 Challenges in Explicit Sample Modeling

While this framework for employing the explicit benchmarks gained from mechanical testing to actual CPFEM simulations seems straightforward, the actual application of experimental data to instantiate a simulation is nontrivial. As discussed earlier, one major limitation in terms of the volume that can be modeled is the computational power that is available. Not only does CPFEM require a fine mesh at the grain level but features such as twins that are common in René 88DT require even more elements due to the number of boundaries that are created. For René 88DT this creates the challenge to design and test a sample volume that contains about 1000 grains and twins that can be modeled explicitly, and 3D characterization of these samples with a resolution of 0.5 μm in order to be able to accurately capture the shape of grain and twin boundaries.

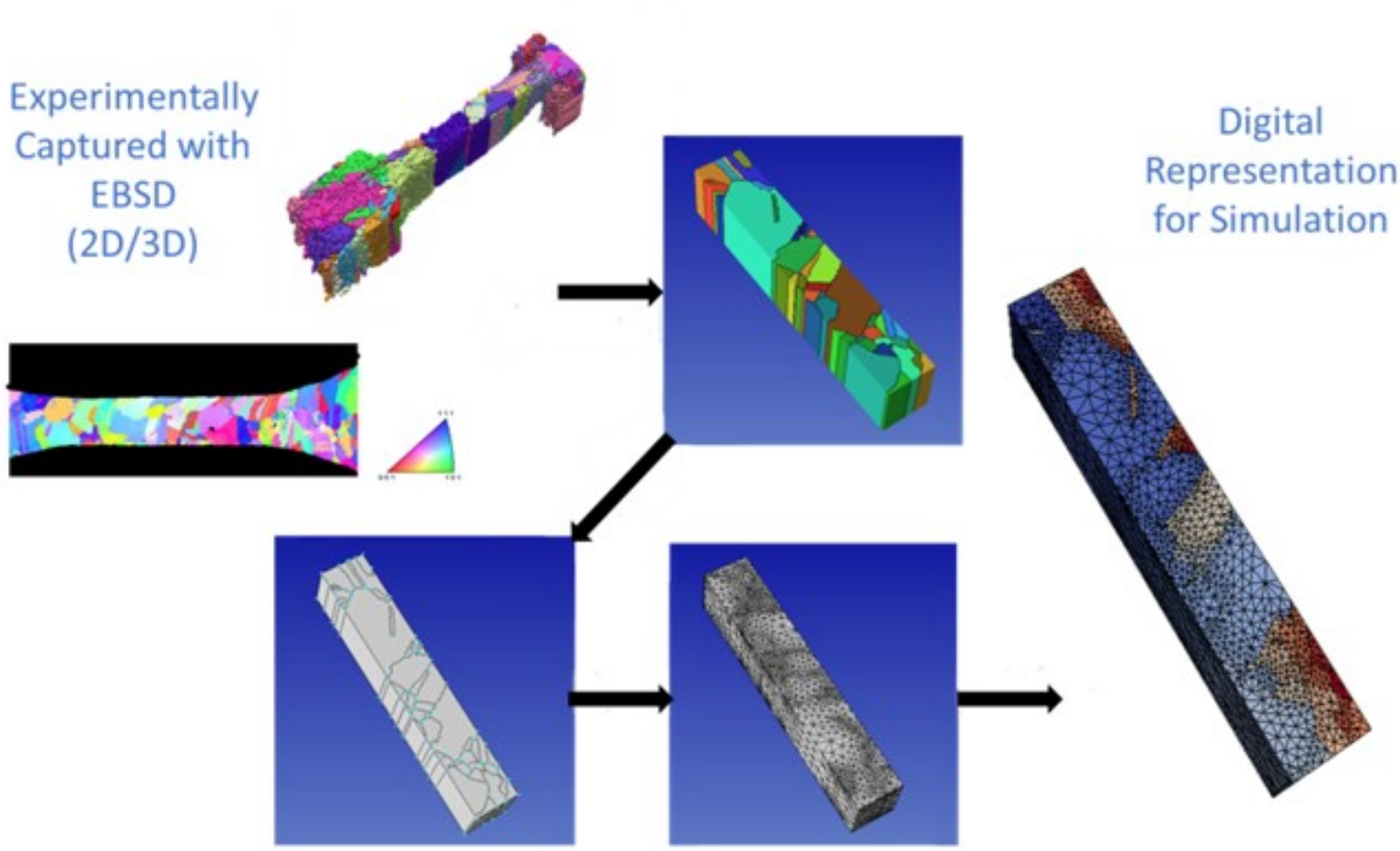

Figure 5-10: Progression from experimentally captured digital microstructure to meshed structure ready for simulation. Digital segmentation based on identifying individual features such as grains is performed, followed by assigning properties to each feature and generating a mesh for performing a CPFEM simulation.

Other significant issues that arise in terms of using experimental data in a simulation are the result of experimental data containing errors. In collection of EBSD data, there are pixels where an orientation cannot be determined, and the data is simply left empty for that pixel, or in which an orientation may not properly be assigned to the pixel. This is especially common at the edges of a sample where signal is lost, or at boundaries where multiple orientations can be sampled. This can lead to discontinuities in the 3D orientation data compromise the digital reconstruction. It is possible to fill in these gaps using a methodology such as a watershed transformation, but if the initial data is poor this can lead to nontrivial modifications to the orientation data that do not allow for a direct comparison between experimental and simulation results. In addition, a technique such as this can give rise to sharp features at grain and twin boundaries that make meshing even more arduous. Limitations in the resolution of experimental techniques also play a significant role in limiting the capability to directly apply CPFEM to experimental data. For one, the time required to collect orientation data via EBSD is almost solely dependent upon the step size selected. Especially for long runs of the SEM required when collecting 3D datasets, one must balance step size resolution with the time required to acquire the EBSD. And, while the in-plane resolution from EBSD may be a parameter that can be directly controlled, in a 3D sectioning process, the out of plane resolution is typically limited even more because of the resolution of a mechanical stage or other tool for controlling motion in the out of plane direction. Resolution of experimental DIC results can also pose a challenge for benchmarking. The resolution possible with DIC is directly linked to the resolution of the image being captured and the quality of the speckle pattern being applied. A finer speckle pattern allows for smaller

DIC subsets and therefore more localized measurements of strain. However, there is again a tradeoff in the image acquisition rate and the resolution of the image. Application of finer speckle patterns can be difficult and require more complex imaging tools such as a SEM. There needs to be an understanding between the experimentalist and modeler in terms of what size scale of deformation needs to be observed as well as the size of features, such as twins in René 88DT, that are expected to play a role in order to determine the proper experimental resolution required.

5.4 Summary and Conclusions

The experimental methodology described here provides a workflow for fabricating and testing microtensile samples at length scales that allow for robust benchmarks for CPFEM simulations. The ability to develop, test and characterize mesoscale samples is necessary in the process of properly benchmarking CPFEM simulations. More than just acquiring the bulk stress-strain response of a sample, investigating local response of the material and the corresponding microstructural features that lead to this behavior provides a new level of benchmarking for ever-improving CPFEM modeling capabilities. The local strain maps developed for the tested René 88DT samples can be used to compare directly with local surface strain maps generated from simulations instantiated with microstructural data from those same samples. This explicit benchmark is both quantitative in terms of the local magnitudes of strain observed as well as qualitative in terms of where on the sample surface these concentrations are located. In addition, the correlation of microstructural information with strain maps in the tested samples provide a benchmark as well. The observations of strain localizations in tested samples occurred in areas of the sample where neighboring

grains and twins exhibited significant mismatches in Schmid factor and elastic modulus with respect to loading. From results in this testing as well as other studies reported in literature, it is seen that near these boundaries, a stress concentration is expected and can therefore be expected to exhibit the location of strain that is observed. Ensuring that this behavior is captured in the results of CPFEM simulations is a critical benchmark and can be used for benchmarking simulations performed in synthetic microstructures beyond the explicit 3D datasets captured experimentally.

Surface observations can only provide so much information, however, and the effect of subsurface microstructure plays a significant role in the observed behavior and the boundary conditions necessary to accurately model experimental results directly. Although still in its infancy, the laser based serial sectioning technique presented in this chapter provides a means for digitally capturing tested 3D volumes that could be utilized to instantiate a simulation and directly compare with experimental results. However, it is evident from the results of the technique, as well as its typical applications, that there is room for improvement in characterizing microscale samples with this tool. Significant steps have been taken to develop a technique for protecting and sectioning freestanding samples of René 88DT using protective plates and conductive epoxy that eliminates laser sectioning artifacts previously observed.

The strain mapping technique presented in this study enables identification of sample regions with localized deformation and comparison with model predictions [88], however, further development may allow for improved resolution in intragranular regions, as well as at grain and twin boundaries [164] to gain more insight into the effects of these features on deformation. Though 3D data of tested samples were not currently

available, efforts to collect them are ongoing. The results of the experiments in this chapter, as well as their attendant 3D microstructural information to be collected, will provide the modeling community with benchmarks. 3D methods such as the presented laser serial sectioning, sectioning via mechanical or chemical polishing and emerging nondestructive characterization techniques such as high energy diffraction microscopy (HEDM) have a lot of potential, especially as the infrastructure for management big data continues to be implemented. However, there are still important considerations, such as the limited spatial resolution and difficulty of reconstruction with HEDM or damage and limited slice resolution with mechanical polishing, in terms of applying these techniques to model benchmarking and validation, and in developing efficient workflows for extracting, processing and utilizing this data from experimental results.

Chapter 6: Summary and Future Work

6.1 Summary

Microtensile tests and unique characterization routes were developed and employed to obtain multi-scale, microstructurally dependent benchmarks for CPFEM models of the polycrystalline Ni-base superalloy René 88DT. This material makes for an interesting case study in merging experiments with multi-scale modeling because it contains microstructural features at different length scales, such as a two-phase microstructure at the subgrain scale and a high volume fraction of twins at the polycrystalline scale. Also, unlike many previous modeling studies of pure metals, this material represents a real structural alloy. This makes modeling efforts for this material strongly applicable to future development and simulation of materials for macroscale components such as in turbine blades and discs.

One major goal of this work was to be able to explicitly characterize tested samples in 3D to be able to instantiate simulations and collect attendant benchmarks of mechanical behavior. Initial microtensile testing was performed on samples with gage cross sections on the order of a few hundred microns machined via Wire EDM and much smaller samples with gage cross sections of 20 x 20 μm machined using a FIB. It was found that the samples machined with wire EDM were able to provide a mechanical response that was very similar to the bulk response of the material. However, due to the size of these samples, there would have been a limit on the computational capacity to explicitly model a sample in 3D. The much smaller size of the FIB-machined samples would have eliminated difficulties due to the volume of the sample to be characterized.

However, from testing performed on these samples it was found that this geometry was too small to capture a true polycrystalline response as the stress-strain response of tested samples appeared to match with behavior more indicative of a single crystal test.

A different sample preparation technique was needed in order to machine samples that were at an intermediate scale. For this purpose, a femtosecond laser machining setup was developed. This tool allowed for precise machining of microtensile samples with cross sectional dimensions on the order of tens of microns up to a few hundred microns at a rate that was an order of magnitude faster than with the FIB; machining of samples 25 times as large as what could be achieved with the FIB was possible in only a matter of minutes.

Through mechanical testing, local strain mapping and microstructural characterization of these mesoscale samples, robust benchmarks were developed to make direct comparisons with CPFEM simulations. Correlation of local strain data with microstructural information from EBSD also provided insight into deformation mechanisms. It was found that strain localized in regions of the sample in which there was a large mismatch in Schmid factor and elastic modulus, in neighboring grains as well as between twins and parent grains. This observation matches well with observations made of this material in fatigue testing and provides insight into how the material behaves during monotonic loading.

Testing samples at different sizes uncovered and revealed an inherent effect of sample size on yield strength. Detailed development of machining processes using wire EDM, laser and FIB was carried out in order to eliminate artifacts thus allowing for linking of experimental results with the direct effects of the underlying microstructure. A

number of samples were tested at different sizes to capture the effect of microstructure. It was seen that on average sample strength decreased with sample size and that the variability of the data increased as the sample width and thickness decreased to 200 μm and below.

In order to further investigate this trend, a series of models were developed. The first was a numerical model that assigned random grain orientations and calculated sample strength based on the Schmid factor of neighboring grains in the gage. Qualitatively, the results of this model matched very well with the trend observed from experiments. Developing this model, led to the realization that it in an FCC material it is very hard to find grains oriented for a low Schmid factor, which explains the absence of an increase in strength at lower sample sizes. A second model introduced dislocation-mediated crystal plasticity to provide more quantitative measures of this behavior. The model was able to capture behavior at three scales: single crystal, quasi-single crystal (2.5 D) and polycrystal. In the single crystal and quasi-single crystal cases, the typical smaller is strong trend was predicted, giving confidence that the model captured this well know effect. However, at the polycrystal scale, the model again matched very well with the experimental data. The use of dislocation-based models could be important in determining the necessary sample size required to test and model a material in order to capture convergence of a property with an RVE. In addition, it can be a useful tool for understanding plasticity in small volumes.

6.2 Future Work

There are a few avenues for further work in benchmarking and modeling this material that could be pursued in future efforts. In terms of modeling, the use of 3D

characterization data and the benchmarks from the tested mesoscale samples in comparing with simulation predictions is a direct path forward. The effort to develop 3D characterization techniques for freestanding samples described in this thesis can be used in order to collect these explicit datasets. Once this information is available, it can be used for instantiating simulations of the developed CPFEM model in order to perform a direct comparison and benchmarking with experimental results. The collected mechanical benchmarks of yield strength, modulus and strain hardening behavior, in addition to the full stress-strain response of tested samples can be compared with simulation predictions to provide a sense of how well the model captures the general mechanical behavior of this material and the effect of size in this material through the use of RVEs. The collected strain mapping data can provide an explicit comparison to samples instantiated with 3D datasets both in terms of seeing that the model predicts the location of strain localizations in the microstructure, as well as the magnitude of this localized strain. In addition, the further proliferation of these datasets to the general scientific community would allow for their use in other modeling studies and contribute to the ongoing effort of gathering these types of datasets for describing materials in 3D.

The results presented in this thesis were from testing performed at room temperature, however the application of superalloys in high temperature environments as well as the yield strength anomaly in superalloys makes high temperature microtensile testing a logical next step. The well-developed techniques in this thesis for fabricating, characterizing and testing samples at room temperature lay the groundwork for microscale testing in other materials and environments. With a high temperature

microtensile load frame, these processes could be adapted for high temperature testing and benchmarking of René 88DT.

During the work of this thesis, the possibility of using HEDM for 3D characterization of René 88DT was investigated. However, due to how challenging it is to reconstruct datasets collected with HEDM, as well as the limited spatial resolution of the technique not being able to accurately capture twins, it has not yet been utilized in characterizing this material. The serial sectioning and EBSD processes outlined in this thesis remain the best tools for 3D characterization of René 88DT because of the spatial resolution that can be achieved with EBSD. But, if the HEDM technique and equipment are improved to a level at which precise characterization of René 88DT is possible, in situ HEDM testing would provide an unparalleled benchmark with real time 3D microstructural information, as well as subsurface details like the residual stress of individual grains that could be captured in models.

7: References

1. Council, N.R., *Integrated computational materials engineering: a transformational discipline for improved competitiveness and national security*. 2008: National Academies Press.
2. Science, N. and T. Council, *Materials genome initiative for global competitiveness*. 2011: Executive Office of the President, National Science and Technology Council.
3. Ghosh, S. and D.M. Dimiduk, *Computational methods for microstructure-property relationships*. 2011: Springer.
4. Echlin, M.P., et al., *The TriBeam system: Femtosecond laser ablation in situ SEM.* Materials Characterization, 2015. **100**: p. 1-12.
5. Brenner, S., et al. *Growth and perfection of crystals*. in *Cooperstown Conference, New York*. 1958.
6. Herring, C. and J. Galt, *Elastic and plastic properties of very small metal specimens.* Physical Review, 1952. **85**(6): p. 1060.
7. Brenner, S.S., *Tensile strength of whiskers.* Journal of Applied Physics, 1956. **27**(12): p. 1484-1491.
8. Brenner, S., *Plastic deformation of copper and silver whiskers.* Journal of Applied Physics, 1957. **28**(9): p. 1023-1026.
9. Tabata, T., et al., *The effect of specimen diameter on tensile behaviors of aluminum thin wires.* Journal of the physical society of Japan, 1976. **40**(3): p. 792-797.
10. Suzuki H, I.S., Takeuchi S. , *In Dislocations and Mechanical Properties of Crystals.* 1957: p. 548-552.
11. Uchic, M.D., et al., *Sample Dimensions Influence Strength and Crystal Plasticity.* Science, 2004. **305**(5686): p. 986-989.
12. Uchic, M.D., et al., *Exploring specimen size effects in plastic deformation of Ni3(Al, Ta).* MRS Proceedings, 2011. **753**: p. BB1.4.
13. Uchic, M.D. and D.M. Dimiduk, *A methodology to investigate size scale effects in crystalline plasticity using uniaxial compression testing.* Materials Science and Engineering: A, 2005. **400-401**: p. 268-278.
14. Greer, J.R. and W.D. Nix, *Size dependence of mechanical properties of gold at the sub-micron scale.* Applied Physics A, 2005. **80**(8): p. 1625-1629.
15. Volkert, C.A. and E.T. Lilleodden, *Size effects in the deformation of sub-micron Au columns.* Philosophical Magazine, 2006. **86**(33-35): p. 5567-5579.
16. Shan, Z., et al., *Mechanical annealing and source-limited deformation in submicrometre-diameter Ni crystals.* Nature materials, 2008. **7**(2): p. 115.
17. Zhang, H., et al., *The design of accurate micro-compression experiments.* Scripta Materialia, 2006. **54**(2): p. 181-186.
18. Orloff, J., et al., *High resolution focused ion beams: FIB and its applications.* Physics Today, 2004. **57**(1): p. 54-55.
19. Kiener, D., et al., *FIB damage of Cu and possible consequences for miniaturized mechanical tests.* Materials Science and Engineering: A, 2007. **459**(1-2): p. 262-272.
20. Greer, J.R. and W.D. Nix, *Nanoscale gold pillars strengthened through dislocation starvation.* Physical Review B, 2006. **73**(24): p. 245410.

21. Moser, B., et al., *Strength and fracture of Si micropillars: A new scanning electron microscopy-based micro-compression test.* Journal of materials research, 2007. **22**(4): p. 1004-1011.
22. Bei, H., et al., *Compressive strengths of molybdenum alloy micro-pillars prepared using a new technique.* Scripta Materialia, 2007. **57**(5): p. 397-400.
23. Greer, J.R., W.C. Oliver, and W.D. Nix, *Size dependence of mechanical properties of gold at the micron scale in the absence of strain gradients.* Acta Materialia, 2005. **53**(6): p. 1821-1830.
24. Shim, S., et al., *Effects of focused ion beam milling on the compressive behavior of directionally solidified micropillars and the nanoindentation response of an electropolished surface.* Acta Materialia, 2009. **57**(2): p. 503-510.
25. El-Awady, J.A., et al., *Effects of focused ion beam induced damage on the plasticity of micropillars.* Physical Review B, 2009. **80**(10): p. 104104.
26. El-Awady, J.A., et al., *Trapping and escape of dislocations in micro-crystals with external and internal barriers.* International Journal of Plasticity, 2011. **27**(3): p. 372-387.
27. Kiener, D., W. Grosinger, and G. Dehm, *On the importance of sample compliance in uniaxial microtesting.* Scripta Materialia, 2009. **60**(3): p. 148-151.
28. Kiener, D., et al., *A further step towards an understanding of size-dependent crystal plasticity: In situ tension experiments of miniaturized single-crystal copper samples.* Acta Materialia, 2008. **56**(3): p. 580-592.
29. Uchic, M.D. and D.M. Dimiduk, *A methodology to investigate size scale effects in crystalline plasticity using uniaxial compression testing.* Materials Science and Engineering: A, 2005. **400**: p. 268-278.
30. *Standard Test Methods for Tension Testing of Metallic Materials*.
31. Shade, P.A., et al., *Experimental measurement of surface strains and local lattice rotations combined with 3D microstructure reconstruction from deformed polycrystalline ensembles at the micro-scale.* Integrating Materials and Manufacturing Innovation, 2013. **2**(1): p. 5.
32. Fujii, K. and K. Fukuya, *Development of micro tensile testing method in an FIB system for evaluating grain boundary strength.* Materials transactions, 2011. **52**(1): p. 20-24.
33. Oluwasegun, K.M., et al., *Micro-tensile strength of a welded turbine disc superalloy.* Materials Science and Engineering: A, 2014. **596**: p. 229-235.
34. McLean, M.J., et al., *Microscale Fracture Toughness of Bismuth Doped Copper Bicrystals Using Double Edge Notched Microtensile Tests.* Experimental Mechanics, 2014. **54**(4): p. 685-688.
35. McCarthy, J., et al., *FIB micromachined submicron thickness cantilevers for the study of thin film properties.* Thin Solid Films, 2000. **358**(1): p. 146-151.
36. Di Maio, D. and S.G. Roberts, *Measuring fracture toughness of coatings using focused-ion-beam-machined microbeams.* Journal of Materials Research, 2005. **20**(2): p. 299-302.
37. Motz, C., T. Schöberl, and R. Pippan, *Mechanical properties of micro-sized copper bending beams machined by the focused ion beam technique.* Acta Materialia, 2005. **53**(15): p. 4269-4279.
38. Gong, J. and A.J. Wilkinson, *Anisotropy in the plastic flow properties of single-crystal α titanium determined from micro-cantilever beams.* Acta Materialia, 2009. **57**(19): p. 5693-5705.
39. Lavenstein, S., et al., *High frequency in situ fatigue response of Ni-base superalloy René-N5 microcrystals.* Acta Materialia, 2018. **144**: p. 154-163.

40. !!! INVALID CITATION !!! {}.
41. Pan, D., et al., *Evolution of a diffusion aluminide bond coat for thermal barrier coatings during thermal cycling.* Acta Materialia, 2003. **51**(8): p. 2205-2217.
42. Boehlert, C., et al., *Microsample creep testing of fully-lamellar TiAl alloys.* Gamma Titanium Aluminides, 1999: p. 669-77.
43. Zupan, M. and K. Hemker, *High temperature microsample tensile testing of γ-TiAl.* Materials Science and Engineering: A, 2001. **319**: p. 810-814.
44. Gianola, D., et al., *Stress-assisted discontinuous grain growth and its effect on the deformation behavior of nanocrystalline aluminum thin films.* Acta Materialia, 2006. **54**(8): p. 2253-2263.
45. Wang, Y., et al., *Microsample tensile testing of nanocrystalline copper.* Scripta Materialia, 2003. **48**(12): p. 1581-1586.
46. Legros, M., et al., *Microsample tensile testing of nanocrystalline metals.* Philosophical magazine A, 2000. **80**(4): p. 1017-1026.
47. Coe, D.J., *The Application of Mocrosample Testing to an Investigation of Electron Irradiation Effects on Type 316 Stainless Steel and Fe-Cu-Mn*. 1999, Johns Hopkins University.
48. Sharpe, W.N., et al. *New test structures and techniques for measurement of mechanical properties of MEMS materials*. in *Microlithography and Metrology in Micromachining II*. 1996. International Society for Optics and Photonics.
49. Hemker, K. and H. Last, *Microsample tensile testing of LIGA nickel for MEMS applications.* Materials Science and Engineering: A, 2001. **319**: p. 882-886.
50. Becker, E., et al., *Fabrication of microstructures with high aspect ratios and great structural heights by synchrotron radiation lithography, galvanoforming, and plastic moulding (LIGA process).* Microelectronic engineering, 1986. **4**(1): p. 35-56.
51. Klaassen, E.H., et al., *Silicon fusion bonding and deep reactive ion etching: a new technology for microstructures.* Sensors and Actuators A: Physical, 1996. **52**(1-3): p. 132-139.
52. Sharpe, W.N., et al., *Fracture Strength of Single-Crystal Silicon Carbide Microspecimens at 24$^{\circ}\hbox {C} $ and 1000$^{\circ}\hbox {C} $.* Journal of Microelectromechanical Systems, 2008. **17**(1): p. 244-254.
53. Rottmann, P.F. and K.J. Hemker, *Experimental quantification of mechanically induced boundary migration in nanocrystalline copper films.* Acta Materialia, 2017. **140**: p. 46-55.
54. Cohen, M.G., R.A. Kaplan, and E.G. Arthurs, *Micro-materials processing.* Proceedings of the IEEE, 1982. **70**(6): p. 545-555.
55. Chichkov, B.N., et al., *Femtosecond, picosecond and nanosecond laser ablation of solids.* Applied Physics A, 1996. **63**(2): p. 109-115.
56. Suzuki, A., M.F.X. Gigliotti, and P.R. Subramanian, *Novel technique for evaluating grain boundary fracture strength in metallic materials.* Scripta Materialia, 2011. **64**(11): p. 1063-1066.
57. Slaughter, S.K., et al. *High Throughput Femtosecond-Laser Machining of Micro-Tension Specimens*. in *TMS 2015 144th Annual Meeting & Exhibition*. 2015. Springer.
58. Pfeifenberger, M.J., et al., *The use of femtosecond laser ablation as a novel tool for rapid micro-mechanical sample preparation.* Materials & Design, 2017. **121**: p. 109-118.
59. Espinosa, H., B. Prorok, and M. Fischer, *A methodology for determining mechanical properties of freestanding thin films and MEMS materials.* Journal of the Mechanics and Physics of Solids, 2003. **51**(1): p. 47-67.

60. Espinosa, H., B. Prorok, and B. Peng, *Plasticity size effects in free-standing submicron polycrystalline FCC films subjected to pure tension.* Journal of the Mechanics and Physics of Solids, 2004. **52**(3): p. 667-689.
61. Haque, M. and M. Saif, *In-situ tensile testing of nano-scale specimens in SEM and TEM.* Experimental mechanics, 2002. **42**(1): p. 123-128.
62. Greek, S. and S.A. Johansson. *Tensile testing of thin-film microstructures*. in *Micromachined Devices and Components III*. 1997. International Society for Optics and Photonics.
63. Sharpe Jr, W.N., *An interferometric strain-displacement measurement system.* 1989.
64. Sharpe, W., B. Yuan, and R. Edwards, *A new technique for measuring the mechanical properties of thin films.* Journal of Microelectromechanical systems, 1997. **6**(3): p. 193-199.
65. Sharpe, W., et al., *Strain measurements of silicon dioxide microspecimens by digital imaging processing.* Experimental Mechanics, 2007. **47**(5): p. 649-658.
66. Kammers, A.D. and S. Daly, *Self-assembled nanoparticle surface patterning for improved digital image correlation in a scanning electron microscope.* Experimental Mechanics, 2013. **53**(8): p. 1333-1341.
67. Stinville, J.C., et al., *High resolution mapping of strain localization near twin boundaries in a nickel-based superalloy.* Acta Materialia, 2015. **98**: p. 29-42.
68. Tao, G. and Z. Xia, *A non-contact real-time strain measurement and control system for multiaxial cyclic/fatigue tests of polymer materials by digital image correlation method.* Polymer Testing, 2005. **24**(7): p. 844-855.
69. Becker, R. and S. Panchanadeeswaran, *Effects of grain interactions on deformation and local texture in polycrystals.* Acta Metallurgica et Materialia, 1995. **43**(7): p. 2701-2719.
70. Zhang, N. and W. Tong, *An experimental study on grain deformation and interactions in an Al-0.5% Mg multicrystal.* International Journal of Plasticity, 2004. **20**(3): p. 523-542.
71. Cheong, K.-S. and E.P. Busso, *Effects of lattice misorientations on strain heterogeneities in FCC polycrystals.* Journal of the Mechanics and Physics of Solids, 2006. **54**(4): p. 671-689.
72. Kalidindi, S.R., A. Bhattacharyya, and R.D. Doherty, *Detailed analyses of grain–scale plastic deformation in columnar polycrystalline aluminium using orientation image mapping and crystal plasticity models.* Proceedings of the Royal Society of London. Series A: Mathematical, Physical and Engineering Sciences, 2004. **460**(2047): p. 1935-1956.
73. Rehrl, C., et al., *Crystal orientation changes: A comparison between a crystal plasticity finite element study and experimental results.* Acta Materialia, 2012. **60**(5): p. 2379-2386.
74. Zhao, Z., et al., *Investigation of three-dimensional aspects of grain-scale plastic surface deformation of an aluminum oligocrystal.* International Journal of Plasticity, 2008. **24**(12): p. 2278-2297.
75. Lim, H., et al., *Grain-scale experimental validation of crystal plasticity finite element simulations of tantalum oligocrystals.* International Journal of Plasticity, 2014. **60**: p. 1-18.
76. Héripré, E., et al., *Coupling between experimental measurements and polycrystal finite element calculations for micromechanical study of metallic materials.* International Journal of Plasticity, 2007. **23**(9): p. 1512-1539.
77. Bhattacharyya, A., et al., *Evolution of grain-scale microstructure during large strain simple compression of polycrystalline aluminum with quasi-columnar grains: OIM*

measurements and numerical simulations. International Journal of Plasticity, 2001. **17**(6): p. 861-883.
78. Turner, T.J. and S.L. Semiatin, *Modeling large-strain deformation behavior and neighborhood effects during hot working of a coarse-grain nickel-base superalloy.* Modelling and Simulation in Materials Science and Engineering, 2011. **19**(6): p. 065010.
79. St-Pierre, L., et al., *3D simulations of microstructure and comparison with experimental microstructure coming from OIM analysis.* International Journal of Plasticity, 2008. **24**(9): p. 1516-1532.
80. Musienko, A., et al., *Three-dimensional finite element simulation of a polycrystalline copper specimen.* Acta materialia, 2007. **55**(12): p. 4121-4136.
81. Alkemper, J. and P. Voorhees, *Quantitative serial sectioning analysis.* Journal of microscopy, 2001. **201**(3): p. 388-394.
82. Spowart, J.E., H.E. Mullens, and B.T. Puchala, *Collecting and analyzing microstructures in three dimensions: a fully automated approach.* Jom, 2003. **55**(10): p. 35-37.
83. Spowart, J.E., *Automated serial sectioning for 3-D analysis of microstructures.* Scripta Materialia, 2006. **55**(1): p. 5-10.
84. Uchic, M.D., et al., *Augmenting the 3D characterization capability of the dual beam FIB-SEM.* Microscopy and Microanalysis, 2004. **10**(S02): p. 1136-1137.
85. Groeber, M.A., et al., *3D reconstruction and characterization of polycrystalline microstructures using a FIB–SEM system.* Materials Characterization, 2006. **57**(4-5): p. 259-273.
86. Zaafarani, N., et al., *Three-dimensional investigation of the texture and microstructure below a nanoindent in a Cu single crystal using 3D EBSD and crystal plasticity finite element simulations.* Acta Materialia, 2006. **54**(7): p. 1863-1876.
87. Shade, P.A., et al., *Micro-tensile testing and 3d-ebsd characterization of pure nickel multi-crystals (preprint)*. 2011, AIR FORCE RESEARCH LAB WRIGHT-PATTERSON AFB OH MATERIALS AND MANUFACTURING DIR METALS CERAMICS AND NONDESTRUCTIVE EVALUATION DIV/METALS BRANCH.
88. Turner, T., et al., *The influence of microstructure on surface strain distributions in a nickel micro-tension specimen.* Modelling and Simulation in Materials Science and Engineering, 2012. **21**(1): p. 015002.
89. *A new TriBeam system for three-dimensional multimodal materials analysis.* Review of Scientific Instruments, 2012. **83**(2): p. 023701.
90. Stinville, J., et al., *A combined grain scale elastic–plastic criterion for identification of fatigue crack initiation sites in a twin containing polycrystalline nickel-base superalloy.* Acta Materialia, 2016. **103**: p. 461-473.
91. Kwakman, L., et al. *Sample preparation strategies for fast and effective failure analysis of 3D devices*. in *39th International Symposium for Testing and Failure Analysis, San Jose, California*. 2013.
92. Xiao, Y., et al., *Investigation of the deformation behavior of aluminum micropillars produced by focused ion beam machining using Ga and Xe ions.* Scripta Materialia, 2017. **127**: p. 191-194.
93. Burnett, T.L., et al., *Large volume serial section tomography by Xe Plasma FIB dual beam microscopy.* Ultramicroscopy, 2016. **161**: p. 119-129.
94. Poulsen, H.F., *Three-dimensional X-ray diffraction microscopy: mapping polycrystals and their dynamics*. Vol. 205. 2004: Springer Science & Business Media.
95. Lienert, U., et al., *High-energy diffraction microscopy at the advanced photon source.* JOM, 2011. **63**(7): p. 70-77.

96. Poulsen, H.F., et al., *Three-dimensional maps of grain boundaries and the stress state of individual grains in polycrystals and powders.* Journal of applied crystallography, 2001. **34**(6): p. 751-756.
97. Bernier, J.V., et al., *Far-field high-energy diffraction microscopy: a tool for intergranular orientation and strain analysis.* The Journal of Strain Analysis for Engineering Design, 2011. **46**(7): p. 527-547.
98. Poulsen, H.F., et al., *Three-dimensional maps of grain boundaries and the stress state of individual grains in polycrystals and powders.* Journal of Applied Crystallography, 2001. **34**(6): p. 751-756.
99. Lauridsen, E.M., et al., *Tracking: a method for structural characterization of grains in powders or polycrystals.* Journal of Applied Crystallography, 2001. **34**(6): p. 744-750.
100. Li, S. and R. Suter, *Adaptive reconstruction method for three-dimensional orientation imaging.* Journal of Applied Crystallography, 2013. **46**(2): p. 512-524.
101. Suter, R., et al., *Forward modeling method for microstructure reconstruction using x-ray diffraction microscopy: Single-crystal verification.* Review of scientific instruments, 2006. **77**(12): p. 123905.
102. Margulies, L., et al., *Strain tensor development in a single grain in the bulk of a polycrystal under loading.* Acta Materialia, 2002. **50**(7): p. 1771-1779.
103. Oddershede, J., et al., *Determining grain resolved stresses in polycrystalline materials using three-dimensional X-ray diffraction.* Journal of Applied Crystallography, 2010. **43**(3): p. 539-549.
104. Shade, P.A., et al., *A rotational and axial motion system load frame insert for in situ high energy x-ray studies.* Review of Scientific Instruments, 2015. **86**(9): p. 093902.
105. Schuren, J.C., et al., *New opportunities for quantitative tracking of polycrystal responses in three dimensions.* Current Opinion in Solid State and Materials Science, 2015. **19**(4): p. 235-244.
106. Turner, T.J., et al., *Crystal Plasticity Model Validation Using Combined High-Energy Diffraction Microscopy Data for a Ti-7Al Specimen.* Metallurgical and Materials Transactions A, 2017. **48**(2): p. 627-647.
107. Pollock, T.M. and S. Tin, *Nickel-based superalloys for advanced turbine engines: chemistry, microstructure and properties.* Journal of propulsion and power, 2006. **22**(2): p. 361-374.
108. Krueger, D.D., R.D. Kissinger, and R.G. Menzies, *Development and Introduction of a Damage Tolerant High Temperature Nickel-Base Disk Alloy, Rene'88DT.* Superalloys 1992: Proceedings of the 7th Intenational Symposium of Superalloys, 1992.
109. Miao, J., T. Pollock, and J. Jones, *Fatigue crack initiation in nickel-based superalloy René 88 DT at 593 C.* Superalloys, 2008: p. 589-97.
110. Keshavarz, S. and S. Ghosh, *Multi-scale crystal plasticity finite element model approach to modeling nickel-based superalloys.* Acta Materialia, 2013. **61**(17): p. 6549-6561.
111. Srikar, V.T. and S. Spearing, *A Critical Review of Microscale Mechanical Testing Methods Used in the Design of Microelectromechanical Systems*. Vol. 43. 2003. 238-247.
112. Gianola, D.S. and C. Eberl, *Micro- and nanoscale tensile testing of materials.* JOM, 2009. **61**(3): p. 24.
113. Hemker, K. and W. Sharpe Jr, *Microscale characterization of mechanical properties.* Annu. Rev. Mater. Res., 2007. **37**: p. 93-126.
114. Giannuzzi, L.A. and F.A. Stevie, *A review of focused ion beam milling techniques for TEM specimen preparation.* Micron, 1999. **30**(3): p. 197-204.

115. Eastman, D.W., et al. *Benchmarking Crystal Plasticity Models with Microtensile Evaluation and 3D Characterization of René 88DT*. in *Superalloys 2016: Proceedings of the 13th Intenational Symposium of Superalloys*. Wiley Online Library.
116. Frey, L., C. Lehrer, and H. Ryssel, *Nanoscale effects in focused ion beam processing.* Applied Physics A, 2003. **76**(7): p. 1017-1023.
117. Adams, D.P., et al., *Micromilling of metal alloys with focused ion beam–fabricated tools.* Precision Engineering, 2001. **25**(2): p. 107-113.
118. Munroe, P.R., *The application of focused ion beam microscopy in the material sciences.* Materials Characterization, 2009. **60**(1): p. 2-13.
119. Ho, K.H. and S.T. Newman, *State of the art electrical discharge machining (EDM).* International Journal of Machine Tools and Manufacture, 2003. **43**(13): p. 1287-1300.
120. Mahendran, S. and R. Devarajan, *MICRO-EDM: OVERVIEW AND RECENT DEVELOPMENTS*. 2018.
121. Bobbili, R., V. Madhu, and A.K. Gogia, *Effect of Wire-EDM Machining Parameters on Surface Roughness and Material Removal Rate of High Strength Armor Steel.* Materials and Manufacturing Processes, 2013. **28**(4): p. 364-368.
122. Liao, Y.S., J.T. Huang, and Y.H. Chen, *A study to achieve a fine surface finish in Wire-EDM.* Journal of Materials Processing Technology, 2004. **149**(1): p. 165-171.
123. Ramakrishnan, R. and L. Karunamoorthy, *Multi response optimization of wire EDM operations using robust design of experiments.* The International Journal of Advanced Manufacturing Technology, 2006. **29**(1): p. 105-112.
124. Rao, P.S., K. Ramji, and B. Satyanarayana, *Experimental investigation and optimization of wire EDM parameters for surface roughness, MRR and white layer in machining of aluminium alloy.* Procedia Materials Science, 2014. **5**: p. 2197-2206.
125. Akhmanov, S.A., V.A. Vysloukh, and A.S. Chirkin, *Optics of femtosecond laser pulses.* Moscow Izdatel Nauka, 1988.
126. Schaffer, C.B., et al., *Micromachining bulk glass by use of femtosecond laser pulses with nanojoule energy.* Optics letters, 2001. **26**(2): p. 93-95.
127. Pronko, P.P., et al., *Machining of sub-micron holes using a femtosecond laser at 800 nm.* Optics Communications, 1995. **114**(1): p. 106-110.
128. von der Linde, D., K. Sokolowski-Tinten, and J. Bialkowski, *Laser–solid interaction in the femtosecond time regime.* Applied Surface Science, 1997. **109-110**: p. 1-10.
129. Perez, D. and L.J. Lewis, *Molecular-dynamics study of ablation of solids under femtosecond laser pulses.* Physical Review B, 2003. **67**(18): p. 184102.
130. Feng, Q., et al., *Femtosecond laser machining of single-crystal superalloys through thermal barrier coatings.* Materials Science and Engineering: A, 2006. **430**(1): p. 203-207.
131. Rizvi, N.H., *Femtosecond laser micromachining: Current status and applications.* Riken review, 2003: p. 107-112.
132. Preuss, S., A. Demchuk, and M. Stuke, *Sub-picosecond UV laser ablation of metals.* Applied Physics A, 1995. **61**(1): p. 33-37.
133. *A review of ultrashort pulsed laser ablation of materials.* Journal of Laser Applications, 1998. **10**(1): p. 18-28.
134. Ostendorf, A. *Femtosecond laser machining*. in *Technical Digest. CLEO/Pacific Rim 2001. 4th Pacific Rim Conference on Lasers and Electro-Optics (Cat. No.01TH8557)*. 2001.
135. Ma, S., et al., *Femtosecond Laser Ablation Regimes in a Single-Crystal Superalloy.* Metallurgical and Materials Transactions A, 2007. **38**(13): p. 2349-2357.

136. Zhang, W., et al., *Femtosecond laser machining characteristics in a single-crystal superalloy.* Rare Metals, 2011. **30**(1): p. 639-642.
137. Semaltianos, N.G., et al., *Femtosecond laser ablation characteristics of nickel-based superalloy C263.* Applied Physics A, 2008. **94**(4): p. 999.
138. *Ablation of solids by femtosecond lasers: Ablation mechanism and ablation thresholds for metals and dielectrics.* Physics of Plasmas, 2002. **9**(3): p. 949-957.
139. Sipe, J., et al., *Laser-induced periodic surface structure. I. Theory.* Physical Review B, 1983. **27**(2): p. 1141.
140. Bonse, J., et al., *Femtosecond laser-induced periodic surface structures.* Journal of Laser Applications, 2012. **24**(4): p. 042006.
141. Suh, C.H., Y.-C. Jung, and Y.S. Kim, *Effects of thickness and surface roughness on mechanical properties of aluminum sheets.* Journal of mechanical science and technology, 2010. **24**(10): p. 2091-2098.
142. Sim, G.-D., et al., *Tailoring the mechanical properties of sputter deposited nanotwinned nickel-molybdenum-tungsten films.* Acta Materialia, 2018. **144**: p. 216-225.
143. Sim, G.-D., et al., *Nanotwinned metal MEMS films with unprecedented strength and stability.* Science advances, 2017. **3**(6): p. e1700685.
144. Hill, R., *Elastic properties of reinforced solids: Some theoretical principles.* Journal of the Mechanics and Physics of Solids, 1963. **11**(5): p. 357-372.
145. Echlin, M.P., W.C. Lenthe, and T.M. Pollock, *Three-dimensional sampling of material structure for property modeling and design.* Integrating Materials and Manufacturing Innovation, 2014. **3**(1): p. 21.
146. Ma, A., F. Roters, and D. Raabe, *A dislocation density based constitutive model for crystal plasticity FEM including geometrically necessary dislocations.* Acta Materialia, 2006. **54**(8): p. 2169-2179.
147. Miyazaki, S., K. Shibata, and H. Fujita, *Effect of specimen thickness on mechanical properties of polycrystalline aggregates with various grain sizes.* Acta Metallurgica, 1979. **27**(5): p. 855-862.
148. Chauhan, S. and A.F. Bastawros, *Probing thickness-dependent dislocation storage in freestanding Cu films using residual electrical resistivity.* Applied Physics Letters, 2008. **93**(4): p. 041901.
149. Ghosh, P. and A.H. Chokshi, *Size Effects on Strength in the Transition from Single-to-Polycrystalline Behavior.* Metallurgical and Materials Transactions A, 2015. **46**(12): p. 5671-5684.
150. Okamoto, N.L., et al., *Specimen-and grain-size dependence of compression deformation behavior in nanocrystalline copper.* International Journal of Plasticity, 2014. **56**: p. 173-183.
151. Wang, C.-j., et al., *Plastic deformation size effects in micro-compression of pure nickel with a few grains across diameter.* Materials Science and Engineering: A, 2015. **636**: p. 352-360.
152. Gu, X.W., et al., *Size-dependent deformation of nanocrystalline Pt nanopillars.* Nano letters, 2012. **12**(12): p. 6385-6392.
153. Tsuchiya, T., et al., *Specimen size effect on tensile strength of surface-micromachined polycrystalline silicon thin films.* Journal of Microelectromechanical Systems, 1998. **7**(1): p. 106-113.
154. Peters, W. and W. Ranson, *Digital imaging techniques in experimental stress analysis.* Optical engineering, 1982. **21**(3): p. 213427.

155. Chu, T., W. Ranson, and M.A. Sutton, *Applications of digital-image-correlation techniques to experimental mechanics.* Experimental mechanics, 1985. **25**(3): p. 232-244.
156. Eberl, C., et al., *Digital image correlation and tracking.* MatLabCentral, Mathworks file exchange server, FileID, 2006. **12413**.
157. Thompson, R.J., *Experimental techniques for the characterization and development of thermal barrier coating bond coat alloys*. 2008: The Johns Hopkins University.
158. Wheeler, R., P. Shade, and M. Uchic, *Insights gained through image analysis during in situ micromechanical experiments.* JOM, 2012. **64**(1): p. 58-65.
159. Shade, P., et al., *A combined experimental and simulation study to examine lateral constraint effects on microcompression of single-slip oriented single crystals.* Acta Materialia, 2009. **57**(15): p. 4580-4587.
160. Kammers, A. and S. Daly, *Small-scale patterning methods for digital image correlation under scanning electron microscopy.* Measurement Science and Technology, 2011. **22**(12): p. 125501.
161. Kammers, A.D. and S. Daly, *Digital image correlation under scanning electron microscopy: methodology and validation.* Experimental Mechanics, 2013. **53**(9): p. 1743-1761.
162. Bird, J., C. Ross, and A. Little, *Mechanics of solids*. 2016: Routledge.
163. Wlodek, S.T., M. Kelly, and D. A. Alden, *The structure of Rene 88DT*. 1996. 129-136.
164. Stinville, J., et al., *Sub-grain scale digital image correlation by electron microscopy for polycrystalline materials during elastic and plastic deformation.* Experimental Mechanics, 2016. **56**(2): p. 197-216.
165. Bagri, A., et al., *Microstructure and Property-Based Statistically Equivalent Representative Volume Elements for Polycrystalline Ni-Based Superalloys Containing Annealing Twins.* Metallurgical and Materials Transactions A, 2018. **49**(11): p. 5727-5744.
166. Roters, F., et al., *Overview of constitutive laws, kinematics, homogenization and multiscale methods in crystal plasticity finite-element modeling: Theory, experiments, applications.* Acta Materialia, 2010. **58**(4): p. 1152-1211.
167. Biery, N., M. de Graef, and T.M. Pollock, *A method for measuring microstructural-scale strains using a scanning electron microscope: Applications to γ-titanium aluminides.* Metallurgical and Materials Transactions A, 2003. **34**(10): p. 2301-2313.
168. Groeber, M.A. and M.A. Jackson, *DREAM. 3D: a digital representation environment for the analysis of microstructure in 3D.* Integrating Materials and Manufacturing Innovation, 2014. **3**(1): p. 5.
169. Alam, Z., et al. *Microstructural aspects of fatigue crack initiation and short crack growth in René 88DT*. in *Superalloys 2016: proceedings of the 13th international symposium of Superalloys. Wiley, Hoboken*. 2016.
170. Lenthe, W.C., et al., *Prediction of Fatigue-Initiating Twin Boundaries in Polycrystalline Nickel Superalloys Informed by TriBeam Tomography.* Microscopy and Microanalysis, 2016. **22**: p. 1732.
171. Stinville, J.C., et al., *Measurement of Strain Localization Resulting from Monotonic and Cyclic Loading at 650 ∘C in Nickel Base Superalloys.* Experimental Mechanics, 2017. **57**(8): p. 1289-1309.

8: Vita

David Eastman was born in Durham, North Carolina in October 1991 to Lawrence and Helen Eastman. He graduated from Howard High School in Ellicott City, Maryland in 2009. He attended the University of Maryland, Baltimore County and earned a Bachelor of Science in Mechanical Engineering in 2013. He joined Professor Kevin Hemker's group at Johns Hopkins University in August 2013 and worked as part of the Center of Excellence in Integrated Materials Modeling, studying Ni-base superalloys and collecting experimental benchmarks for crystal plasticity models. In October of 2018, he completed his Doctor of Philosophy degree in Mechanical Engineering.